Department of Science and High Technology
PhD in Computer Science and Computational Mathematics, XXXI Cycle

APPLICATIONS OF METHOD OF LINES IN CHEMICAL ENGINEERING PROBLEMS

Marco Barozzi

Advisor: prof. Sabrina Copelli

December 2018

La vostra carriera sarà caratterizzata da innumerevoli presentazioni delle quali non capirete assolutamente nulla

---

Prof. Umberto Mosco

Acknowledgement

The list of persons that allowed me to reach this point is pretty long, so I will try to be as much concise as possible. First acknowledgement go for my advisor, professor Sabrina Copelli, who followed me over all this path. It was a pleasure to work with her, even with a lot of "non linear" Ph.D. issues (just to stay on the scientific topic). I owe her all the work I was able to do in these 3 years, and I hope we will be able to work together in the future.

Many thanks to the whole Ph.D. Committee, including professors Donatelli M., Serra Capizzano S. and Cassani D. (I directly cite them only because they are the only ones I had the fortune to know and speak with), who bestowed their trust upon me, even if I do not come from a purely mathematical environment.

Thanks to all professors who kept our PhD courses and conferences, providing fresh and interesting scientific knowledge.

Thanks to ICAP-Sira, a company I could work with during the first year of my Ph.D. It was extremely fun and useful to see "equations" by the other side of the coin.

Thanks to my parents and family, who sustained me both economically and emotionally during all this adventure.

Thanks to my friends, always a good and pleasant company for the harsh times.

Thanks to my dog, always ready to disrupt my work when I'm working on my PC at home.

Contents

1 Introduction **7**

1.1 Problem formulation 9
1.2 Transport equations 10
1.3 Eulerian approach 13
1.3.1 Continuity equation 13
1.3.2 Material balance equation 14
1.3.3 Momentum balance equation 16
1.3.4 Energy balance equation 20
1.4 Constitutive relations 21
1.4.1 Material diffusion 22
1.4.2 Thermal diffusion 23
1.4.3 Momentum diffusion 23
1.5 Boundary and initial conditions 25
1.6 Classification of transport equations 26
1.6.1 Steady state problems 27
1.6.2 Unsteady state problems 28
1.6.3 Geometrical classification 29

2 State of the art **31**

2.1 Dust explosions 31
2.1.1 Modelling dust explosions 35
2.1.2 Case histories 37
2.1.3 Important parameters in dust explosions 49
2.2 Runaway Boundaries for PFRs 55
2.2.1 Theories in the '70s 60
2.2.2 New models in the '80s 63
2.2.3 Recent works 67

3 Method of lines **70**
3.1 PDEs structure . . . 71
3.2 Generation of the spatial grid . . . 72
3.3 Discretization of the spatial derivates . . . 74
3.3.1 Uniform grids . . . 75
3.3.2 Accuracy and order . . . 77
3.3.3 Non-uniform grid . . . 77
3.3.4 General algorithm . . . 78
3.4 Translation of the boundary conditions . . . 82
3.4.1 Elimination of the unknown variables . . . 82
3.4.2 Introduction of fictious nodes . . . 84
3.4.3 Introduction of Algebraic Equations . . . 86
3.5 Solving the semi-discrete ODEs system . . . 87

4 Mathematical models **91**
4.1 Estimation of k_{ST} of explosive dusts in a 20 L apparatus . . . 91
4.1.1 Model description . . . 92
4.1.2 Ignitors model . . . 93
4.1.3 Pyrolisys-Devolatilization model . . . 96
4.1.4 Volatiles combustion characterization . . . 99
4.1.5 Balance equations . . . 101
4.1.6 Final model . . . 108
4.2 Plug Flow Reactor models . . . 109
4.2.1 1-D PFR models . . . 114
4.2.2 Case study: Oxidation of Naphthalene . . . 118
4.2.3 Nondimensional models . . . 122

5 Results **129**
5.1 Simulation of k_{ST} . . . 129
5.1.1 Solution of the PDE system . . . 133
5.1.2 Aspirin . . . 140
5.1.3 Cork . . . 143
5.1.4 Corn starch . . . 144
5.1.5 Niacin . . . 146
5.1.6 Polyethylene . . . 147
5.1.7 Polystyrene . . . 149
5.1.8 Sugar . . . 150
5.1.9 Wheat flour . . . 152

5.1.10 Parity plots 153
5.2 Plug Flow Reactor simulation 154
5.2.1 Numerical experiments 156
5.2.2 Steady state model 162
5.2.3 Unsteady state model, constant temperature jacket . . 170
5.2.4 Unsteady state model, constant inlet temperature jacket 176
5.2.5 Unsteady state model, temperature controller 183
5.2.6 Summary of results 186

6 Conclusions **188**

Abstract

In this work, two problems in chemical engineering are studied and solved. Estimation of an important parameter of dust explosions, the deflagration index k_{ST}, and a study of unsteady state with axial diffusion Plug Flow Reactors are presented. Both problems are approached by characterizing the physical phenomena involved with suitable transport equations. Such equations have been developed with the synergy of both consolidated theoretical models and *ad hoc* assumptions and semi-empiric approaches, according to the specific problem analyzed. The final equation systems result in a system of non-linear Partial Differential Equations.

The numerical solution of such equations has been performed by implementing the Method of Lines, a numerical method based on the discretization of spatial derivative operators, transforming a system of PDEs into a system of ODEs or DAEs. The resulting ODEs/DAEs systems have been implemented and solved inside $MATLAB^{\text{TM}}$environment. The Method of Lines is presented for uniform and non-uniform grids, generalized with the use of spatial derivatives discretization stencils of several orders of accuracy.

For the estimation of k_{ST}, we validated the model with 8 organic dust: Aspirin, Cork, Corn starch, Niacin, Polyethylene, Polystyrene, Sugar and Wheat flour. Results showed an interesting match between experimental and simulated data: predictions for the deflagration index were good, while the evolution of process variables (such as the temperature of the gas phase), still leaves room for improvements.

For the PFR study, we propose 1-D models, taking in account the reactor start-up, thermal and material axial diffusion, and the presence of a heating/cooling system. In order to judge the quality of the results, we took as case study a reaction well studied in the literature over the years: the oxidation of Naphthalene. We developed the so-called Runaway Boundaries for the reaction considered. Our results found good matches with the avail-

able literature data and analysis. We also noticed a shifting of the Runaway Boundaries when considering a more realistic heating/cooling system.

List of Figures

1.1 Different control volumes 11
1.2 Infinitesimal volume of a fluid 13
1.3 Pressure and viscous forces on the perpendicular sections of the infinitesimal cube 17
1.4 28

2.1 From the classic fire triangle to the dust explosion pentagon (Source: Occupational Safety and Health Administration) . . . 32
2.2 Effect of particle size on combustion (Source: Eckhoff R.,2003) 33
2.3 Potential reconstruction of the scene of wheat flour explosion in Mr. Giacomelli's bakery, based on count Morozzo report (Source: Eckhoff R., 2003) 38
2.4 Picture of the silo roof after the wheat grain explosion (Source: Eckhoff R.,2003) 40
2.5 Picture of the air shaft along the damaged walls of reinforced concrete silo cells of the grain terminal (Source: Eckhoff R.,2003) 41
2.6 Scheme of the atomized aluminium production (Source: Lunn G.,1984) 42
2.7 Some pictures of the plant after the accident (Source: Lunn G., 1984) 42
2.8 Picture of the Imperial Sugar plant after the accident (Source: CSB, official website) 43
2.9 Some pictures of the plant before and after the accident (Source: Eckhoff R., 2015) 45
2.10 Reconstruction of the blast wave propagation (Source: Eckhoff R., 2015) 47
2.11 Picture of the dust collecting barrel of the #1 filter (Source: Eckhoff R., 2015) 48

2.12 Cross section the 20 liter explosion vessel for determination of the minimum explosible concentration (Source: Cashdollar and Hertzberg, 1985) 51
2.13 Sketch of a 1.2 liter Hartmann bomb (Source: Eckhoff R., 2003) 52
2.14 Sketch of a standard 1 m^3 vessel (Source: Eckhoff R., 2003) . 53
2.15 Picture of a 20L Siwek apparatus 54
2.16 Typical evolution of a pressure profile during an explosion (the slope of the red line is the k_{ST}) 55
2.17 Sensitivity of the maximum temperature rise as a function of the cooling intensity N [23] 59
2.18 First Barkelew diagram showing that all the sensitivity curves have a common envelope [23] 59
2.19 Second Barkelew diagram differentiating between sensitive and insensitive operating conditions [23] 59
2.20 p-T phase plane, showing p-T trajectories, maxima curve p_{m}, loci of inflection points ($p_{\mathrm{i,max}}$ and $p_{\mathrm{i,min}}$) and the simplified curve p_{cr} 61
2.21 $S(T, T_{\mathrm{in}})$ as a function of the axial coordinate l for different values of the ratio of reactant to coolant heat capacity for a PFR (τ_{PFR}).[29] 67

3.1 Example of uniform grid with 10 nodes 73
3.2 Comparison between a uniform grid and a non-uniform one, generated by $F(\tilde{x}_i) = x^2$ 75

4.1 Zirconium burning particle 95
4.2 Sketch of a single dust particle pyrolysis mechanism 97
4.3 TGA of aspirin 99
4.4 Simple Plug Flow reactor scheme 110
4.5 Feed-forward control scheme 112
4.6 Feed-back control scheme 113
4.7 Simple Plug Flow reactor scheme 115
4.8 Simple Plug Flow reactor scheme 116
4.9 Napthalene oxidation reaction scheme 119
4.10 Napthalene oxidation process scheme 120

5.1 Gas temperature for Corn Starch (with average diameter: 54 μm) 134

5.2 Volatile production rate for Corn Starch (with average diameter: 54 μm) . . . 135
5.3 Particle temperature for Corn Starch (with average diameter: 54 μm) . . . 135
5.4 Gas temperature in the sphere with Relative Tolerance=1E-6 and Absolute Tolerance=1E-9, study on grid dependence) . . . 137
5.5 With Relative Tolerance=1E-3 and Absolute Tolerance=1E-6) 139
5.6 Gas temperature with different schemes and Relative Tolerance=1E-6 and Absolute Tolerance=1E-9) . . . 140
5.7 TGA for aspirin . . . 141
5.8 Conversion vs. Temperature profile for Aspirin . . . 143
5.9 Conversion vs. Temperature profile for Cork . . . 144
5.10 Conversion vs. Temperature profile for Corn . . . 146
5.11 Conversion vs. Temperature profile for Niacin . . . 147
5.12 Conversion vs. Temperature profile for Polyethylene . . . 149
5.13 Conversion vs. Temperature profile for Polystirene . . . 150
5.14 Conversion vs. Temperature profile for Sugar . . . 152
5.15 Conversion vs. Temperature profile for Wheat flour . . . 153
5.16 Comparison among Theoretical and Experimental values of k_{ST} 154
5.17 Study of grid dependence for reactor and jacket temperature at final time with Relative Tolerance=1E-6 and Absolute Tolerance=1E-9. T_{IN}=625 K, v_0=0,5 $\frac{m}{s}$, $v_{0,cool}$=0,3 $\frac{m}{s}$) . . . 158
5.18 Reactor and jacket temperature at final time with different schemes and Relative Tolerance=1E-6 and Absolute Tolerance=1E-9.T_{IN}=625 K, v_0=0,5 $\frac{m}{s}$, $v_{0,cool}$=0,3 $\frac{m}{s}$) . . . 160
5.19 Distribution of grid points with a Chebyshev polynomial . . . 161
5.20 Reactor and jacket temperature at final time with different grids, Relative Tolerance=1E-6 and Absolute Tolerance=1E-9.T_{IN}=625 K, v_0=0,5 $\frac{m}{s}$, $v_{0,cool}$=0,3 $\frac{m}{s}$) . . . 162
5.21 Temperature and Sensitivity analysis with respect to the inlet pressure (Varma and Morbidelli, 1999) . . . 163
5.22 Evolution of conversion and temperature along the reactor with P_{IN}=1.6 kPa, T_{IN}=625 K, v_0=0,5 $\frac{m}{s}$, T_w= 625 K . . . 165
5.23 Evolution of conversion and temperature along the reactor with P_{IN}=1.85 kPa, T_{IN}=625 K, v_0=0,5 $\frac{m}{s}$ . . . 166
5.24 Temperature and Sensitivity analysis with respect to the inlet pressure, for the steady state model . . . 168

5.25 Maximum temperature and Sensitivity respect to different values of P_{IN}, with T_{IN}=625 K, v_0=1 $\frac{m}{s}$, steady state model. . . 169
5.26 Evolution of conversion and temperature along the reactor with P_{IN}=1.6 kPa, T_{IN}=625 K, v_0=0,5 $\frac{m}{s}$, T_w= 625 K 171
5.27 Evolution of conversion and temperature along the reactor with P_{IN}=1.85 kPa, T_{IN}=625 K, v_0=0,5 $\frac{m}{s}$, T_w= 625 K . . . 172
5.28 Maximum temperature and Sensitivity respect to different values of P_{IN}, with T_{IN}=625 K, v_0=1 $\frac{m}{s}$, unsteady state model with constant jacket temperature. 173
5.29 Maximum temperature and Sensitivity respect to different values of T_{IN}, with P_{IN}=1.6 kPa, v_0=1 $\frac{m}{s}$, unsteady state model with constant jacket temperature. 175
5.30 Temperature profiles for the unsteady state model with constant inlet temperature for the jacket (P_{IN}=1.6 kPa, T_{IN}=625 K, v_0=1 $\frac{m}{s}$, $v_{0,cool}$=0,3 $\frac{m}{s}$ $T_{w,IN}$= 625 K) 177
5.31 Temperature profiles for the unsteady state model with constant inlet temperature for the jacket (P_{IN}=1.85 kPa, T_{IN}=625 K, v_0=1 $\frac{m}{s}$, $v_{0,cool}$=0,3 $\frac{m}{s}$ $T_{w,IN}$= 625 K) 178
5.32 Temperature profiles for the unsteady state model with constant inlet temperature for the jacket (P_{IN}=1.85 kPa, T_{IN}=625 K, v_0=1 $\frac{m}{s}$, $v_{0,cool}$=1 $\frac{m}{s}$ $T_{w,IN}$= 625 K) 178
5.33 Sensitivity respect to different values of P_{IN}, with T_{IN}= 625 K, v_0=0.2/1 $\frac{m}{s}$, $v_{0,cool}$=0,3 $\frac{m}{s}$ $T_{w,IN}$= 625 K 180
5.34 Sensitivity respect to different values of T_{IN}, with P_{IN}= 1.6 kPa, v_0=0.2/1 $\frac{m}{s}$, $v_{0,cool}$=0,3 $\frac{m}{s}$ $T_{w,IN}$= 625 K 182
5.35 Sensitivity respect to different values of P_{IN}, with T_{IN}= 625 K, v_0=0.2/1 $\frac{m}{s}$, $v_{0,cool}$=0,3 $\frac{m}{s}$ $T_{w,IN}$= 625 K and thermocouple placed at z_T=0.2 184
5.36 Sensitivity respect to different values of T_{IN}, with P_{IN}= 1.6 kPa, v_0=0.2/1 $\frac{m}{s}$, $v_{0,cool}$=0,3 $\frac{m}{s}$ $T_{w,IN}$= 625 K and thermocouple placed at z_T=0.2 185
5.37 Sensitivity respect to different values of P_{IN} and T_{IN}, with v_0=0.2 $\frac{m}{s}$, $v_{0,cool}$=0,3 $\frac{m}{s}$ $T_{w,IN}$= 625 K and thermocouple placed at z_T=0.6 186

List of Tables

1.1 PDE classification 30

2.1 Fundamental aspects of dust explosions mechanisms (Eckhoff, 2003) 36
2.2 Hazard class of explosible dusts (Source: OSHA CPL 03-00-008) 55

3.1 List of weights for centered schemes in uniform grids (Source: Fornberg B., 1988) 80
3.2 List of weights for upwind schemes in uniform grids (Source: Fornberg B., 1988) 81

4.1 List of naphthalene oxidation physical-chemical parameters . . 123
4.2 List of adimensional parameters 124
4.3 List of adimensional variables 125

5.1 Computational times with Relative Tolerance equal to 1E-6 and Absolute Tolerance equal to 1E-9 136
5.2 Computational times with Relative Tolerance equal to 1E-3 and Absolute Tolerance equal to 1E-6 138
5.3 Computational times with Relative Tolerance equal to 1E-6 and Absolute Tolerance equal to 1E-9 140
5.4 Pyrolysis kinetic parameters for Aspirin dust 142
5.5 Pyrolysis kinetic parameters for Aspirin dust 142
5.6 Pyrolysis kinetic parameters for Cork dust 143
5.7 Pyrolysis kinetic parameters for Cork dust 144
5.8 Pyrolysis kinetic parameters for Corn starch dust 145
5.9 Pyrolysis kinetic parameters for Corn starch dust 145
5.10 Pyrolysis kinetic parameters for Niacin dust 146
5.11 Pyrolysis kinetic parameters for Niacin dust 147

5.12 Pyrolysis kinetic parameters for Polyethylene dust 148
5.13 Pyrolysis kinetic parameters for Polyethylene dust 148
5.14 Pyrolysis kinetic parameters for Polystyrene dust 149
5.15 Pyrolysis kinetic parameters for Polystyrene dust 150
5.16 Pyrolysis kinetic parameters for Sugar dust 151
5.17 Pyrolysis kinetic parameters for Sugar dust 151
5.18 Pyrolysis kinetic parameters for Wheat flour dust 152
5.19 Pyrolysis kinetic parameters for Wheat flour dust 153
5.20 Computational times with Relative Tolerance equal to 1E-6 and Absolute Tolerance equal to 1E-9, testing grid dependence 157
5.21 Computational times with Relative Tolerance equal to 1E-6 and Absolute Tolerance equal to 1E-9, 250 grid points 159
5.22 Computational times for different grids, with Relative Tolerance equal to 1E-6 and Absolute Tolerance equal to 1E-9, 250 grid points 161

Introduction

Since ancient times, one of the most challenging aspects in human history has been describing and manipulating physical phenomena. There are evidence of the use of rough mathematical tools even in Egyptian times (around 1800 BC), probably used for agricultural or construction purposes. In the Roman-Greek period, significant developments have been made in the geometry field, with mathematicians like Archimedes and Euclid. Archimedes' studies have seen implementations even in war strategies: the city of Syracuse used mirrors to reflect solar light in order to defend the coast from enemy naval assaults. In the 17-th century, mathematicians Isaac Newton and Wilhelm Leibniz introduced the modern *calculus*. With the introduction of integrals and derivatives, a powerful tool to describe real physical phenomena was introduced. Still today, after more than 300 years, Differential Equations (DEs) are still the mainstream tool used to describe phenomena of everyday life, spacing from the description of space, sky, and clouds, to models describing the evolution animal species in an environment. The general concept of a DE is pretty intuitive: by one side, we have an independent variable(s), that is the quantity we want to estimate. By the other hand, we have the dependent variable(s), that is the element upon which the independent variable(s) evolves. In most physical phenomena, the independent variables are represented by space (hence, 3 variables) and time. If a single or a system of DE depends only on a variable, we will have an Ordinary Differential Equation system (ODEs). If more dependent variables are present, we have a Partial Differential Equation system (PDEs). ODEs and PDEs were and are even today subject of research: existence and shape of solutions, stable and reliable numerical methods to solve them, applications to real cases.

In this context, chemical reactions are included in the set of phenomena that can be modelled by DEs. Chemical engineering made huge advances in process intensification, understanding and development of chemical systems

through the years, thanks to the constant evolution and introduction of powerful mathematical tools. A lot of relevant problems in applied engineering have been successfully resolved by approaching them with DEs. Such DEs are generally constructed by a set of proper balance equations, that contain relations describing the specific subject. Standard balances are done with respect to mass, energy, and momentum, and they will be discussed in detail later. The main feature of predictive models involving chemical reactions is their non-linearity, generally due to the reaction term itself. Non-linearity adds remarkable complications: for example, a lot of numerical methods and theorems are easy to be applied only to linear equation systems. Also, non-linearity in evolutive phenomena (namely, something that we want to know how will behave over time), has unreliable long-time predictions because the solution highly depends on the value of *initial conditions* imposed. It is an aim of this work to study real phenomena characterized by this behavior.

In this work, a mathematical approach has been applied to resolve two actually opened problems in chemical engineering. In the first part, a model to predict an important parameter (named dust deflagration index k_{ST}) is presented. Nowadays, such value is determined with fully experimental methods, putting a certain amount of dust inside an apparatus designed ad hoc, where the dust deposit is force-ignited. In this work a semi-empirical model, describing ignition and combustion of explosive dusts in such apparata is proposed. Also, the model takes into account dust particle size, evaluating different values for different particles distribution. The mathematical model proposed requires minor experimental parameters in order to be closed, leading to a much cheaper procedure. Results show good agreement between experimental data and predicted values.

In the second part, a model to simulate Plug Flow Reactor is proposed. In this case, as a novelty respect to other works, we develop it under unsteady state hypothesis and with thermal and material axial diffusion, and we take into account for a cooling system that can have a temperature controller installed. The unsteady state condition allows for the estimation of problems during the reactor start-up, that is a delicate procedure. Generally, PFRs are supposed to have very fast transients, and we want to study it by directly evaluating it. Thermal and material diffusion are also in general neglected in the main studies about PFRs. The final aim of this part of the work is to calculate the so-called Runaway Boundaries for the PFR: a diagram that shows under which operating conditions the system becomes unstable. We will study whether our model, with diffusion and unsteady state condi-

tions, provides different results respect to the one presented in the current literature, which are based on steady state with no diffusion models.

The work is organized as it follows: the next section will provide a general discussion about the problem formulation, describing the main tools used to represent a chemically reactive system. In the following chapter, a state of the art of the proposed arguments is presented, showing the current state of these problems, based on the dedicated scientific literature. Chapter 3 provides a description of the resolution approach applied (the Method of Lines), with a focus on how it should be implemented to a PDEs system. In section 4 the mathematical models developed are presented, specifying the hypotheses used to build them. Finally, the results of the simulations carried out are reported.

1.1 Problem formulation

The most common way to simulate a chemically reactive system is the introduction of fluid dynamics: a science dedicated to studying chemical and physical phenomena, based on the concept of conservation laws. A conservation law is a concept which implies that, given a volume, a certain quantity will remain constant over time. The physical properties of the fluid are described by constitutive relations, such as equations of state (like the perfect gases for gaseous phases). Constitutive relations are necessary in order to close the systems of equation generated because conservation laws (represented by transport equations) introduce conceptual elements, that would remain unspecified otherwise.

All transport equations are based on this intuitive and general balance equation, applied to a generic quantity:

$$Accumulation = Inlet - Ouput + Generation \tag{1.1}$$

The meaning of this equation can be explained in this way: the evolution over time of a certain quantity (*Accumulation*), is increased by all the *Inlet* flows of the same+ minus the *Output* flows. The *Generation* is an internal phenomenon that can lead to both consumption or production of the quantity taken. With the implementation of calculus, every single term can be mathematically described by using integrals, derivatives, and other tools. When talking about fluid dynamics, it is important to classify between compressible fluids and noncompressible ones. Several approaches exists to evaluate

that status of a fluid. The most simple is to introduce the Mach number M, defined as the ratio between the fluid velocity and the speed of sound:

$$M = \frac{v}{v_{sound}} \tag{1.2}$$

If this number is low ($M < 1$), the fluid can be considered not compressible. Establishing whether a fluid is compressible or not is an aspect of critical importance in order to address a proper model. Another important hypotheses required for the application of fluid dynamics equations is the continuum state, which is the case of the studies carried out in this work. The concept of continuum means that a fluid property is defined at every portion of space, allowing DEs to be effectively implemented. This is, of course, an approximation, since matter is made of particles (protons, electrons, atoms and so on), but as long as we want to discuss the problem on "lengths" that are way larger than those particles (and this is the case), the continuum state is a consistent hypothesis.

1.2 Transport equations

Here we introduce the generic balance equations that can be used to describe a reactive system. These equations are called *transport equations*, and they describe how a physical quantity (mass, energy, and momentum), is conserved in a portion of space. Taken in general form, these equations can be applied to different geometries (cartesian, cylindrical or spherical), which choice depends on the related phenomenon. Two important concepts used to approach this argument are *control system* and *control volume*.

Control system A set of atoms and molecules that characterize a well-defined region. This group is able to interact with other control systems, but mass flows between them are neglected

Control volume A precise portion of space considered. In the most general sense, it can be changed over time

In order to be rigorous, fluid dynamic equations should be written with respect to system volumes, due to the physical interpretation of material balances. However, it is simpler to formulate an equation using the control volume approach. For this reason, it is needed to introduce a relation to

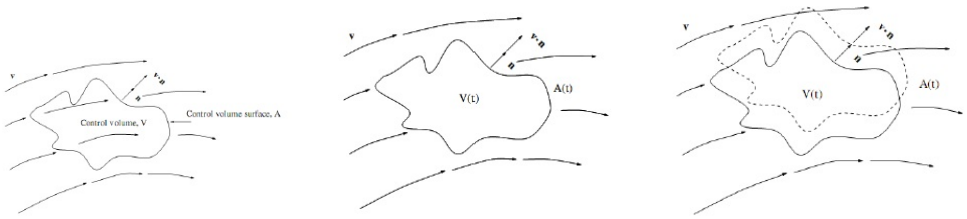

(a) *Eulerian control volume* (b) *Lagrangian control volume* (c) *Macroscopic control volume*

Figure 1.1: Different control volumes

swap between the two concepts. This is granted by the Reynolds transport theorem.

Theorem 1 (of Reynolds transport) *Consider an Euclidean region $\Omega(t)$, with a boundary $\partial\Omega(t)$. Let then be the vector $\boldsymbol{x}(t) \subset \Omega(t)$. $\boldsymbol{v}(\boldsymbol{x}, t)$ is the velocity field in the region, and $\boldsymbol{n}(\boldsymbol{x}, t)$ is the outward pointing normal vector. Given then a scalar, vector or tensor field $\boldsymbol{f}(\boldsymbol{x}, t)$, it respects this relation:*

$$\frac{d}{dt}\left(\int_{\Omega(t)} \boldsymbol{f} dV\right) = \int_{\Omega(t)} \frac{\partial \boldsymbol{f}}{\partial t} dV + \int_{\partial\Omega(t)} (\boldsymbol{v} \cdot \boldsymbol{n})\, \boldsymbol{f} dA \tag{1.3}$$

The control volume approach can be applied in several ways, depending on which properties we give to the control volume:

Eulerian approach In the Eulerian formulation, the control volume is supposed to be fixed in space. The balances are then developed according to the fact that the control volume "observes" what happens upon it. The Eulerian formulation is fairly simple to implement and leads to mathematical models easier to be solved. An example of Eulerian control volume is shown in Fig. 1.1a.

Lagrangian approach In the Lagrangian approach, the control volume is a portion of the fluid, that moves with respect to a fixed reference frame. The main assumption for this formulation consists in assuming that the fluid properties in a certain point and time, are the same of the Lagrangian control volume, in the same point ant time. A scheme is presented in Fig. 1.1b.

Macroscopic approach An alternative is to consider a control volume of a fixed dimension and shape, that can be immobile or in motion. The balance equations are then written in integral form. By the application of the Reynolds transport theorem and Gauss theorem, we get differential equations of the same structure of the other two approaches. Fig.1.1c schematizes the control volume used in this approach.

Remark It could be interesting to have methods to shift between Eulerian and Lagrangian models. This is done by applying the concept of *substantial derivative*(also called *total* or *convective* derivative). The total derivative of a quantity $\phi(\mathbf{x}, t)$ is defined at it follows:

$$\frac{D\phi}{Dt} = \left.\frac{\partial\phi}{\partial t}\right|_{x,y,z} + \mathbf{v}_S \nabla\phi \tag{1.4}$$

$\mathbf{v}_S$ is the observer velocity. If the observer moves with the fluid then we have $\mathbf{v}_S = \mathbf{v}$, and:

$$\frac{D\phi}{Dt} = \left.\frac{\partial\phi}{\partial t}\right|_{x,y,z} + \mathbf{v}\nabla\phi \tag{1.5}$$

At this point, if we consider the same hypothesis of theorem 1, we can calculate the total derivative of the integral of $\mathbf{f}(\mathbf{x}, t)$ over the domain $\Omega(t)$:

$$\frac{D}{Dt}\left(\int_{\Omega(t)} \mathbf{f}\, dV\right) = \int_{\Omega} \frac{\partial \mathbf{f}}{\partial t} dV + \int_{\partial\Omega(t)} (\mathbf{v}\cdot\mathbf{n})\, \mathbf{f}\, dA \tag{1.6}$$

In this formulation, Ω is a fixed volume, namely the volume of $\Omega(t)$at time t. By applying the Gauss theorem, the surface integral in Eq.1.6 can be transformed in a volume integral:

$$\int_{\partial\Omega(t)} (\mathbf{v}\cdot\mathbf{n})\, \mathbf{f}\, dA = \int_{\Omega} \nabla(\mathbf{f}\mathbf{v}) dV \tag{1.7}$$

Hence, the transport theorem can be written in following form, where it is highlighted the "Lagrangian" term at the left of the equality, and the "Eulerian" part on the right.

$$\frac{D}{Dt}\left(\int_{\Omega(t)} \mathbf{f}\, dV\right) = \int_{\Omega} \left[\frac{\partial \mathbf{f}}{\partial t} + \nabla(\mathbf{f}\mathbf{v})\right] dV \tag{1.8}$$

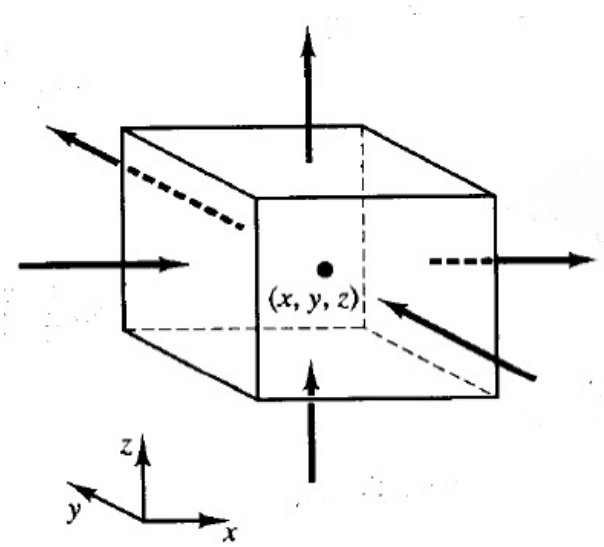

Figure 1.2: Infinitesimal volume of a fluid

1.3 Eulerian approach

Since we introduced a tool to shift between the two approaches, we will consider all the transport equations in the Eulerian approach (also, it is the model considered in all presented works). In order to set the balances, we will take an infinitesimal fluid volume considered in Fig.1.2. The arrows indicate a generic flow on the cube surfaces.

1.3.1 Continuity equation

We first introduce the *Continuity equation*, that reflects the total mass conservation law, under the Eulerian hypothesis. Following the statement 1.1, in this case the generation term disappears, due to the total mass conservation. The accumulation term on the cube becomes:

$$\frac{\partial m}{\partial t} = \frac{\partial}{\partial t}(\rho \partial V) = \frac{\partial \rho}{\partial t} \partial x \partial y \partial z$$

Where m indicates the mass, and ρ the density of the fluid. The material flow through the cube surfaces can be estimated by multiplying the material flux by the cube surface. The material flux is evaluated with a simple first

order Taylor expansion. Since the only known property is the fluid velocity v in the center of the cube, the Taylor expansions for the material fluxes should start in the cube center. We then have, for the 3 surfaces oriented as the axis (in order, surfaces x, y, z):

$$[\rho v_x|_{x+\frac{1}{2}\partial x} - \rho v_x|_{x-\frac{1}{2}\partial x}]\partial y\partial z \simeq \left[\rho v_x + \frac{\partial(\rho v_x)}{\partial x}\frac{1}{2}\partial x - \rho v_x + \frac{\partial(\rho v_x)}{\partial x}\frac{1}{2}\partial x\right]\partial y\partial z = \\ = \frac{\partial(\rho v_x)}{\partial x}\partial x\partial y\partial z$$

$$[\rho v_y|_{y+\frac{1}{2}\partial y} - \rho v_y|_{y-\frac{1}{2}\partial y}]\partial x\partial z \simeq \left[\rho v_y + \frac{\partial(\rho v_y)}{\partial y}\frac{1}{2}\partial y - \rho v_y + \frac{\partial(\rho v_y)}{\partial y}\frac{1}{2}\partial y\right]\partial x\partial z = \\ = \frac{\partial(\rho v_y)}{\partial y}\partial x\partial y\partial z$$

$$[\rho v_z|_{z+\frac{1}{2}\partial z} - \rho v_z|_{z-\frac{1}{2}\partial z}]\partial x\partial y \simeq \left[\rho v_z + \frac{\partial(\rho v_z)}{\partial z}\frac{1}{2}\partial z - \rho v_z + \frac{\partial(\rho v_z)}{\partial z}\frac{1}{2}\partial z\right]\partial x\partial y = \\ = \frac{\partial(\rho v_z)}{\partial z}\partial x\partial y\partial z$$

This result can be summarized introducing the divergence of the vector velocity $\mathbf{v}(v_x, v_y, v_z)$.

$$Inlet - Outlet = -\left[\frac{\partial \rho v_x}{\partial x} + \frac{\partial \rho v_y}{\partial y} + \frac{\partial \rho v_z}{\partial z}\right]\partial x\partial y\partial z = -\nabla(\rho\mathbf{v})\partial x\partial y\partial z$$

Finally, the continuity equation appears in the final form:

$$\frac{\partial \rho}{\partial t} + \nabla(\rho\mathbf{v}) = 0 \tag{1.9}$$

It is important to notice that, even if this balance has been deduced in cartesian coordinates, it stands under a generic domain.

1.3.2 Material balance equation

The material balance takes in account instead for the single chemical species involved in the process. This type of balance can be written both in molar or massive terms. Sometimes an approach has advantages over the other. For example, chemical reactions are generally defined ad function of concentration, thus a molar balance is preferable. Before approaching the treatment

of the material balance, it is useful to introduce some deeper concepts about fluid velocities. A fluid motion is due to the motion of a huge set of molecules. Even if we treat fluids as continuous media, in reality they are made of microscopic particles, that are in motion and interact with themselves. In this sense, the fluid velocity $\mathbf{v}$ used before (like in Eq.1.9), is more precisely the *mean massive velocity*. Assuming that we have a fluid composed of NC species, we define $\mathbf{v}$ as:

$$\mathbf{v} = \frac{\sum_{j=1}^{NC} \rho_j \mathbf{v}_j}{\sum_{j=1}^{NC} \rho_j} = \frac{\sum_{j=1}^{NC} \rho_j \mathbf{v}_j}{\rho} = \sum_{j=1}^{NC} \omega_j \mathbf{v}_j \tag{1.10}$$

Where we introduced the massive fraction ω_j

$$\omega_j = \frac{\rho_j}{\rho} \tag{1.11}$$

What is the physical interpretation of this quantity? It means that, while each singular particle can freely move in each direction(with velocity $\mathbf{v}_j$), statistically they tend all to move in the same direction $\mathbf{v}$. This allows to introduce the diffusive velocity $\mathbf{v}_j, d$:

$$\mathbf{v}_j, d = \mathbf{v}_j - \mathbf{v} \tag{1.12}$$

That is, the velocity related to single species diffusion phenomena.

We return now to the definition of the material balance equation. Differently from the continuity equation, that considers the total mass, the generation term is not negligible. The accumulation term, following the same approach for the continuity equation 1.9 becomes:

$$\frac{\partial m_j}{\partial t} = \frac{\partial}{\partial t}(\rho_j \partial V) = \frac{\partial \rho_j}{\partial t} \partial x \partial y \partial z$$

The material balance imposes that a certain quantity of j can change due to diffusion, convection and reaction:

$$\frac{\partial m_j}{\partial t} = \left[\frac{\partial m_j}{\partial t}\right]_{conv} + \left[\frac{\partial m_j}{\partial t}\right]_{diff} + \left[\frac{\partial m_j}{\partial t}\right]_{rxn}$$

The convection term can be developed as before, based on the infinitesimal volume in Fig.1.2, leading to:

$$\left[\frac{\partial m_j}{\partial t}\right]_{conv} = -\left[\frac{\partial \rho_j v_x}{\partial x} + \frac{\partial \rho_j v_y}{\partial y} + \frac{\partial \rho_j v_z}{\partial z}\right] \partial x \partial y \partial z = -\nabla(\rho_j \mathbf{v}) \partial x \partial y \partial z$$

$$\left[\frac{\partial m_j}{\partial t}\right]_{diff} = -\left[\frac{\partial j_{j,x}}{\partial x} + \frac{\partial j_{j,y}}{\partial y} + \frac{\partial j_{j,z}}{\partial z}\right] \partial x \partial y \partial z = -\nabla(\mathbf{j}_j)\partial x \partial y \partial z$$

The reaction term is left in the general form:

$$\left[\frac{\partial m_j}{\partial t}\right]_{rxn} = R_j \partial x \partial y \partial z$$

Since it is not possible to summarize all chemical reactions in a single general formula,the term R_j depends upon the specific chemical processes involved. Now it possible to get the complete expression for the material balance equation:

$$\frac{\partial_j \rho}{\partial t} + \nabla(\rho_j \mathbf{v}_j) = R_j \tag{1.13}$$

As in the former case, this relation is valid in other geometries, accordingly to the correct expression of the divergence operator.

Remark In order to close the balance equation systems, NC material balances should be considered (one for each chemical species). An alternative could be take $NC - 1$ single species material balance and the continuity equation. Indeed, the sum of all the NC material balances gives back the continuity equation.

$$\sum_{j=i}^{NC} \left[\frac{\partial m_j}{\partial t}\right] = \frac{\partial \rho}{\partial t} + \nabla(\rho \mathbf{v}) = 0$$

This result comes from the fact that the sum of both diffusive terms and reactions are equal to zero, due to mass conservation.

$$\sum_{j=i}^{NC} \mathbf{j}_j = 0 \qquad \sum_{j=i}^{NC} R_j = 0$$

1.3.3 Momentum balance equation

In order to compute the momentum balance equation, it is necessary to provide a description of the different type of stresses that can insist upon the fluid.

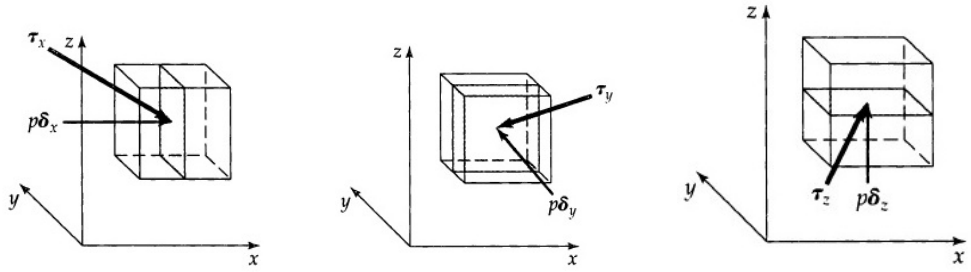

(a) (b) (c)

Figure 1.3: Pressure and viscous forces on the perpendicular sections of the infinitesimal cube

Molecular stress tensor

Let us consider the usual infinitesimal cube of fluid. Imagine now to slice it in two part by using a perpendicular plane in the cube center. Fig.1.3 shows the sections after this operation. Let us take the cubes sliced with a plane perpendicular to the x axis (Fig.1.3a). We want now to "replace" the missing half with a force per unit of surface $\boldsymbol{\pi}_x$. Since this vector can have every orientation, we can divide this component in two pieces:

- a component oriented as the x axis, that is related to the pressure of the fluid p, called $p\boldsymbol{\delta}_x.\boldsymbol{\delta}_x$ is the versor parallel to x axis
- a component $\boldsymbol{\tau}_x$, that can have every orientation

Stresses related to pressure are perpendicular to the cube surfaces, the term $\boldsymbol{\tau}_x$ is harder to study, since it still can have every orientation.

If we repeat this operation on all axis, we get this set:

$$\begin{aligned}\boldsymbol{\pi}_x &= p\boldsymbol{\delta}_x + \boldsymbol{\tau}_x \\ \boldsymbol{\pi}_y &= p\boldsymbol{\delta}_y + \boldsymbol{\tau}_y \\ \boldsymbol{\pi}_z &= p\boldsymbol{\delta}_z + \boldsymbol{\tau}_z\end{aligned}$$

Each $\boldsymbol{\tau}_{x,y,z}$ can be again split into three vectors parallel to the axis, leading the well known tensor, which has 9 components. In particular, the resulting tensor $\underline{\boldsymbol{\tau}}$ contains the *viscous stresses* upon the fluid, and the $p\underline{\boldsymbol{\delta}}$ tensor is the *hydrostatic stress tensor*. We can summarize all in this compact notation:

$$\underline{\boldsymbol{\pi}} = p\underline{\boldsymbol{\delta}} + \underline{\boldsymbol{\tau}} \tag{1.14}$$

The tensor components $\pi_{xx} = p + \tau_{xx}$,$\pi_{yy} = p + \tau_{yy}$ and $\pi_{zz} = p + \tau_{zz}$ are called *normal stresses*, due to their orientation, normal to the surfaces perpendicular to te main axis. The others are called *shear stresses*.

Momentum convective fluxes tensor

The momentum per unit of volume of our fluid cube is equal to $\rho\mathbf{v}$. In order to evaluate the momentum flux over the cube, we can always consider the sliced cube, obtaining $\rho\mathbf{v}v_x$,$\rho\mathbf{v}v_y$,$\rho\mathbf{v}v_z$, one for each perpendicular surfaces to the axis. Of course, since $\mathbf{v}$ is a vectorial quantity, all the single components generate another tensor. The structure of the complete tensor is the following:

$$\rho\mathbf{v}\mathbf{v} = \left(\sum_i \boldsymbol{\delta}_i \rho v_i\right)\mathbf{v} = \left(\sum_i \boldsymbol{\delta}_i \rho v_i\right)\left(\sum_j \boldsymbol{\delta}_j \rho v_j\right) = \sum_i \sum_j \boldsymbol{\delta}_i \boldsymbol{\delta}_j \rho v_i v_j$$

Momentum balance

Now all the components to develop the momentum balance equation are set. Differently from the other balances, here we have vectorial quantities. Hence, the formulation will be more complex. As in the previous case, we can consider the contribution of each single axis, resulting in scalar equation. We consider as an example the component parallel to the x axis. The accumulation term is:

$$\frac{\partial \rho v_x}{\partial t}\partial x \partial y \partial z$$

For simplicity sake, we group the two stress tensors in a unique term $\underline{\boldsymbol{\Phi}}$:

$$\underline{\boldsymbol{\Phi}} = \underline{\boldsymbol{\pi}} + \rho\mathbf{v}\mathbf{v} = p\underline{\boldsymbol{\delta}} + \underline{\boldsymbol{\tau}} + \rho\mathbf{v}\mathbf{v}$$

With this grouping, we can consider the $Inlet - Outlet$ component of momentum. As in the previous case, it is possible to approximate this difference with a first order Taylor expansion form the cube center. in this case we have more components, due to the tensor properties. On the component parallel to x axis we get then:

$$Inlet - Outlet = -\left[\frac{\Phi_{xx}}{\partial x} + \frac{\Phi_{yx}}{\partial y} + \frac{\Phi_{zx}}{\partial z}\right]\partial x \partial y \partial z$$

External contribution are related to forces such as gravity. We group all the effects under a single force $\mathbf{F}$, that splits into gravity g and other generic forces h. The final balance on the x axis is:

$$\frac{\partial \rho v_x}{\partial t}\partial x\partial y\partial z = -\left[\frac{\Phi_{xx}}{\partial x} + \frac{\Phi_{yx}}{\partial y} + \frac{\Phi_{zx}}{\partial z}\right]\partial x\partial y\partial z + \rho \mathbf{F}_x \partial x\partial y\partial z$$

Which can be simplified in:

$$\frac{\partial \rho v_x}{\partial t} = -\left[\frac{\Phi_{xx}}{\partial x} + \frac{\Phi_{yx}}{\partial y} + \frac{\Phi_{zx}}{\partial z}\right] + \rho \mathbf{F}_x$$

If we consider all the components, we can get the balance over all the volume:

$$\frac{\partial(\rho \mathbf{v})}{\partial t} = -\nabla \underline{\mathbf{\Phi}} + \rho \mathbf{F}$$

Where we define the divergence of the tensor as:

$$\nabla \underline{\boldsymbol{\tau}} = \left(\frac{\partial}{\partial x}, \frac{\partial}{\partial y}, \frac{\partial}{\partial z}\right)\begin{bmatrix}\Phi_{xx} & \Phi_{xy} & \Phi_{xz}\\ \Phi_{yx} & \Phi_{yy} & \Phi_{yz}\\ \Phi_{zx} & \Phi_{zy} & \Phi_{zz}\end{bmatrix} = \begin{bmatrix}\frac{\partial \Phi_{xx}}{\partial x} & \frac{\partial \Phi_{xy}}{\partial y} & \frac{\partial \Phi_{xz}}{\partial z}\\ \frac{\partial \Phi_{yx}}{\partial x} & \frac{\partial \Phi_{yy}}{\partial y} & \frac{\partial \Phi_{yz}}{\partial z}\\ \frac{\partial \Phi_{zx}}{\partial x} & \frac{\partial \Phi_{zy}}{\partial y} & \frac{\partial \Phi_{zz}}{\partial z}\end{bmatrix}$$

It is possible to split the tensor into the single components.

$$\frac{\partial(\rho \mathbf{v})}{\partial t} = -\nabla p - \nabla \underline{\boldsymbol{\tau}} + \rho \mathbf{F} - \nabla(\rho \mathbf{v}\mathbf{v}) + \rho \mathbf{F} \tag{1.15}$$

This equation is also known as *Cauchy equation*.

Remark Its useful to define the Cauchy equation with the total derivative. If we rewrite the equation in this way:

$$\frac{\partial(\rho \mathbf{v})}{\partial t} + \nabla(\rho \mathbf{v}\mathbf{v}) = -\nabla p - \nabla \underline{\boldsymbol{\tau}} + \rho \mathbf{F} \tag{1.16}$$

The first term can be written in explicit form:

$$\rho\frac{\partial \mathbf{v}}{\partial t} + \mathbf{v}\frac{\partial \rho}{\partial t} + \mathbf{v}\nabla(\rho \mathbf{v}) + \rho \mathbf{v}\nabla(\mathbf{v}) = \rho\left[\frac{\partial \mathbf{v}}{\partial t} + \mathbf{v}\nabla(\mathbf{v})\right] - \mathbf{v}\left[\frac{\partial \rho}{\partial t} + \nabla(\rho \mathbf{v})\right] \tag{1.17}$$

It is possible to apply the continuity equation 1.9 and the definition of total derivative, and we get:

$$\rho\frac{D\mathbf{v}}{Dt} = -\nabla p - \nabla \underline{\boldsymbol{\tau}} + \rho \mathbf{F} \tag{1.18}$$

Mechanical energy conservation From the momentum balance equation 1.17 it is possible to obtain the mechanical energy conservation law. While it is not true in general, it has several interesting applications. In order to derive that we multiply the former balance by the fluid velocity $\mathbf{v}$:

$$\mathbf{v}\rho\frac{D\mathbf{v}}{Dt} = -\mathbf{v}\nabla p - \mathbf{v}\nabla\underline{\boldsymbol{\tau}} + \rho\mathbf{F}\mathbf{v} \tag{1.19}$$

By applying the definition of specific kinetic energy we then get:

$$\rho\frac{D\hat{E}_K}{Dt} = -\mathbf{v}\nabla p - \mathbf{v}\nabla\underline{\boldsymbol{\tau}} + \rho\mathbf{F}\mathbf{v} \tag{1.20}$$

That is the mechanical energy transport equation.

1.3.4 Energy balance equation

The energy balance should consider all the possible energy forms:

Kinetic energy Associated with fluid velocity, it will be considered in the *specific* form (that means, independent from the fluid mass) $\hat{E}_K$, defined as $\hat{E}_K = \frac{1}{2}\mathbf{v}\mathbf{v}$

Internal energy It is related to molecules, atoms and particles motion (thus, it highly depends from temperature). We will assume that the specific internal energy $\hat{U}$ its a quantity that depends upon fluid density, temperature, and composition.

Potential energy Associated with the fact that fluid is inside gravity. In general it is preferable to consider it as an external work that insists on the system due to the presence of the gravitational field.

Let us consider again the infinitesimal fluid volume represented in Fig.1.2. If we get a single cube face, we can define the convective energy flux that passes through it:

$$\mathbf{e}_{conv} = \rho(\hat{E}_K + \hat{U})\mathbf{v}$$

There are also contributions due to the stresses applied on the fluid. Those can be evaluated by using the molecular stress tensor $\boldsymbol{\pi}$ (that is a force per unit of surface, like a pressure). The energy flux associated with this is then:

$$\mathbf{e}_{stress} = \underline{\boldsymbol{\pi}}\mathbf{v} = \begin{bmatrix}\boldsymbol{\pi}_x\mathbf{v}\\ \boldsymbol{\pi}_y\mathbf{v}\\ \boldsymbol{\pi}_z\mathbf{v}\end{bmatrix} = \begin{bmatrix}\pi_{xx}v_x + \pi_{xy}v_y + \pi_{xz}v_z\\ \pi_{yx}v_x + \pi_{yy}v_y + \pi_{yz}v_z\\ \pi_{zx}v_x + \pi_{zy}v_y + \pi_{zz}v_z\end{bmatrix}$$

Now that convective and stress contributions have been defined,the energy diffusion is missing. We will call this term $\mathbf{q}$. The total energy flux $\mathbf{e}$ is than:

$$\mathbf{e} = \rho(\hat{E}_K + \hat{U})\mathbf{v} + \underline{\boldsymbol{\pi}}\mathbf{v} + \mathbf{q}$$

At last, the contribution of external forces (like gravity), is summarized by:

$$\mathbf{e}_{ext} = \rho\mathbf{F}\mathbf{v}$$

All elements are now defined. Now, they need to be applied to the usual infinitesimal volume. Energy fluxes can be treated as in the former cases, and by applying a first order Taylor expansion we get the final energy balance:

$$\frac{\partial}{\partial t}[\rho(\hat{E}_K + \hat{U})] = -\nabla\mathbf{e} + \rho\mathbf{F}\mathbf{v}$$

Which can be expanded as:

$$\frac{\partial}{\partial t}[\rho(\hat{E}_K + \hat{U})] + \nabla[\rho(\hat{E}_K + \hat{U})\mathbf{v}] = -\nabla(\underline{\boldsymbol{\pi}}\mathbf{v}) - \nabla\mathbf{q} + \rho\mathbf{F}\mathbf{v} \tag{1.21}$$

Or, by splitting the molecular stress tensor in its components:

$$\frac{\partial}{\partial t}[\rho(\hat{E}_K+\hat{U})]+\nabla[\rho(\hat{E}_K+\hat{U})\mathbf{v}] = -\nabla(p\underline{\boldsymbol{\delta}}\mathbf{v})-\nabla(\underline{\boldsymbol{\tau}}\mathbf{v})-\nabla\mathbf{q}+\rho\mathbf{f}\mathbf{v}+\rho\mathbf{g}\mathbf{v} \tag{1.22}$$

1.4 Constitutive relations

In this part we are defining the *constitutive equations*, the relations used to close some of the terms involved in the transport equations. Such relations, such as diffusion, have been introduced in a theoretical way, and then they are still unknowns in the equations proposed. Diffusive fluxes, tensors, and reaction terms need to be expressed as a function of physical properties of the fluid, such as temperature, pressure, concentrations. Constitutive relations are equations that accomplish this task, generating closed expressions, that can be effectively solved. While transport equations are always valid, since they translate real physical facts, constitutive relations are the mathematical form of models based upon certain hypotheses. Thus, they are not necessarily true, and should be taken accordingly to the real case they want to be applied. In the proposed models, we will always consider fluids with no memory: the local status of the fluid at a certain time can be always expressed as a function of instantaneous and local properties.

1.4.1 Material diffusion

We have introduced earlier the diffusive flux of the $j-th$ species $\mathbf{j}_j$. It is possible to address material diffusion to four different sources.

- Classic material diffusion $\mathbf{j}_j^0$, associated with concentration gradients
- Thermal material diffusion $\mathbf{j}_j^t$, associated with temperature gradients (also called *Soret effect*)
- Pressure material diffusion $\mathbf{j}_j^p$, associated with pressure gradients
- Forced diffusion $\mathbf{j}_j^f$, associated with the imposition external fields

The global material diffusion $\mathbf{j}_j$ is hence the sum of these terms:

$$\mathbf{j}_j = \mathbf{j}_j^0 + \mathbf{j}_j^t + \mathbf{j}_j^p + \mathbf{j}_j^f$$

In most of the common applications, the predominant term is the standard material diffusion$\mathbf{j}_j^0$. The simplest and most used relation to characterize this type of diffusion is the *Fick's law*: diffusion has not a prevalent direction, and the material flux is proportional to mass gradients. We have then:

$$\mathbf{j}_j = -\wp_j \nabla \rho_j = -\rho \wp_j(\omega_j)$$

In molar terms, the partial density is substituted by the component concentration:

$$\mathbf{J}_j = -\wp_j \nabla C_j$$

The constant $\wp_j$ $[\frac{m}{s}]$, is the *diffusion coefficient*, of the $j-th$ species. This constant is generally evaluated by using semi-empirical correlations or by imposing mixing rules.

Remark The Fick's law can bring to numerical problems: since the single coefficients are evaluated with not completely rigorous methods, this can lead to not respecting the zero-sum of all diffusive terms. This can be solved with two different approaches:

1. Correction on inert: the diffusive coefficients related to the inerts (which do not interfere with reactions), are calculated in order to force the zero sum of the diffusive flows.
2. Correction of the diffusion velocity: the fluid velocity is corrected with an additional argument that grants the closure of diffusive fluxes.

1.4.2 Thermal diffusion

In a similar way to material diffusion, even thermal diffusive effects can be split into more components:

- Thermal diffusion q^t, associated with temperature gradients
- Diffusion due to concentration gradients q^c, associated with concentration gradients
- Pressure thermal diffusion q^p, associated with pressure gradients
- Forced diffusion q^f, associated with the imposition external fields

Again, the most common term is the thermal diffusion q^t, which can be described by the *Fourier's law*, that gives the following expression:

$$q^t = -\alpha \nabla T$$

α is called *thermal conductivity*.

Remark When talking about heat flows, thermal radiation should be considered. Modelling radiative effects is a complex task. Thermal radiation is due to electromagnetic waves, its effects are strictly related to the wavelength of the radiation. Chemical species targeted by electromagnetic waves, not only result in heating, but they can also interact with them. If they have enough energy, these waves can break chemical bonds, and interact with reactions. The most simplified approach consists in taking only the thermal power (whenever this is in accord to the system considered).

1.4.3 Momentum diffusion

Viscous stresses exist only when the fluid is in motion, and their tensor should be addressed. When a fluid is in motion, the molecules that actually move try to drag the adjacent ones, and intermolecular forces causes friction between them. The entity of intermolecular forces depends on the fluid considered. In this case, we consider Newtonian fluids. A Newtonian fluid is a fluid in which the viscous stresses arising from its flow, at every point, are linearly proportional to the local strain rate of its deformation over time. If the

Newtonian fluid hypothesis is consistent, the following relation describes the viscous stresses tensor:

$$\underline{\boldsymbol{\tau}} = -\mu(\nabla \circ \mathbf{v} + (\nabla \circ \mathbf{v})^T) + \left(\frac{2}{3}\mu - \kappa\right)(\nabla \mathbf{v})\underline{\boldsymbol{\delta}} \tag{1.23}$$

Where $\nabla \circ \mathbf{v}$ is the velocity gradient tensor, $(\nabla \circ \mathbf{v})^T$ its transpose, $\underline{\boldsymbol{\delta}}$ a unitary tensor (namely, an identity matrix). The the velocity gradient tensor assumes this form:

$$\nabla \circ \mathbf{v} = \left(\frac{\partial}{\partial x}, \frac{\partial}{\partial y}, \frac{\partial}{\partial z}\right)^T (v_x, v_y, v_z) = \begin{bmatrix} \frac{\partial v_x}{\partial x} & \frac{\partial v_y}{\partial x} & \frac{\partial v_z}{\partial x} \\ \frac{\partial v_x}{\partial y} & \frac{\partial v_y}{\partial y} & \frac{\partial v_z}{\partial y} \\ \frac{\partial v_x}{\partial z} & \frac{\partial v_y}{\partial z} & \frac{\partial v_z}{\partial z} \end{bmatrix} \tag{1.24}$$

The quantity $\nabla \circ \mathbf{v} + (\nabla \circ \mathbf{v})^T$ presented in Eq.1.23 is also called the *rate of strain tensor* $\underline{\boldsymbol{D}}$.

$$\underline{\boldsymbol{D}} = (\nabla \circ \mathbf{v} + (\nabla \circ \mathbf{v})^T) \tag{1.25}$$

$$\boldsymbol{D}_{i,j} = \frac{\partial v_j}{\partial i} + \frac{\partial v_i}{\partial j} \tag{1.26}$$

Sometimes, $\underline{\boldsymbol{D}}$ is formulated by multiplying it by $\frac{1}{2}$. This constitutive relation requires two additional information: the *dynamic viscosity* μ and the *volume (or dilatational) viscosity* κ. The viscosity μ expresses the fluid resistance to shearing flows, where adjacent layers move parallel to each other at different speeds. Measurements and models to estimate it have been deeply studied and developed over the years, and it is possible to find accurate values for this quantity. The dilatational viscosity κ is associated with compressible fluids, that can exhibit internal frictions due to expansions and contractions. In most of the applications (it is possible to show that for mono-atomic gases its value is 0), it is reasonable to assume that this coefficient is close to zero.

As a remark, if we use Newton's law 1.23 to close the Cauchy equation 1.17, we get three equations of momentum conservation. If they are then coupled with the continuity equation 1.9, we get the well-known *Navier-Stokes equations*. Navier-Stokes equations are useful because they describe the physics of many real physical phenomena, such as weather, ocean currents, water flow in a pipe and air flow around a wing. They are still today subject of deep research and analysis (but they will not be treated in this work).

1.5 Boundary and initial conditions

All the equations just described require some additional information in order to be solved, due to the nature of derivative operators. It is necessary to supplement the system with Initial Conditions and Boundary Conditions.

Initial conditions The concept of initial condition is strongly related to evolutive systems: starting from a certain point, we want to know the dynamic of the solution. Reactive systems belong to these problems. From a strictly mathematical point of view, there is no limitation on when the condition should be put (it is possible to assume that the interested variable assumes a specific value at any time). Although, when dealing with real evolution problems (like dynamics of populations), we generally know the status of the system at *time zero*. From there the term *initial* condition.

Boundary conditions Boundary conditions, as the name suggests, impose the variables value over the domain boundaries. For example, the Laplace equation on a one-dimensional domain (namely, a line), will require two BCs (one at the first point of the domain , one at the edge). BCs represent the physical properties of the system on the boundary, they highly depend on the specific problem, and their form can influence by a lot the complexity of the final system.

In PDEs, the type of conditions are classified into three groups, based on the mathematical structure they assume:

- Dirichlet conditions
- Neumann conditions
- Robin conditions

We take as an example the 1-D Laplace equation (ϕ is a generic variable), defined over the domain $D \in (0, 1)$:

$$\Delta\phi = 0 \qquad \frac{d^2\phi}{dx^2} = 0 \tag{1.27}$$

Dirichlet conditions are the most simple, and they simply assume that, on the boundary domain, or at a certain time, the independent variable is a

constant. In this case:

$$\begin{aligned} \phi(x=0) &= a \qquad a \in \mathbb{R} \\ \phi(x=1) &= b \qquad b \in \mathbb{R} \end{aligned}$$

Neumann conditions, instead, impose the derivative of the variable over the domain boundaries. This is an example of Neumann BCs:

$$\begin{aligned} \left.\frac{d\phi}{dx}\right|_{x=0} &= 0 \\ \left.\frac{d\phi}{dx}\right|_{x=1} &= 0 \end{aligned}$$

This type of BCs are common in diffusion problems, when at the boundary we want to neglect diffusive effects.

A Robin condition, at last, is a mix of the two previous cases:

$$\begin{aligned} \alpha(x=0)\phi + \left.\frac{d\phi}{dx}\right|_{x=0} &= g(x=0) \\ \alpha(x=1)\phi + \left.\frac{d\phi}{dx}\right|_{x=1} &= g(x=1) \end{aligned}$$

Where α and g are two functions defined on the boundary (in 1-D domains, of course, this is trivial).

1.6 Classification of transport equations

It is natural to think that, once almost all the possible physical phenomena in chemical systems have been treated, we now can potentially simulate and predict every possible real system. Unfortunately, this is not true. By one side, constitutive relations are not always adequate to model reality, but by the other side, the proposed systems (that appear as PDEs), need to be solved. The numerical solution of transport equation (especially Navier-Stokes equations) it is still today an interesting and challenging study to be performed, with a lot of opened problems. For this reason, it is pretty common to impose simplifications over the proposed equations, depending upon the specific problem. Sometimes they are consistent, and the results are comparable with real phenomena, sometimes they are not. Historically,

several simplified systems have been deeply studied by themselves (like the Laplace equation). Hence, a classification of the transport equations systems that arise from different simplifications is needed. We generally talk about: *linear* and *non linear* PDEs, *steady* and *unsteady state* problems, *n-th order* problems and *parabolic, hyperbolic* and *elliptic* PDEs.

1.6.1 Steady state problems

Steady state is a concept that implies the non-dependence from time of the problem. Hence, assuming that the original problem has time derivative components, the system passes through a *transient state*: a finite portion of time where the system variables evolve over time. Once this is over, the system variables are constant or maintain dependences only in spatial directions. This case is very common in chemical reactions: since the initial status of the system is made of *reagents*, at some point an *equilibrium state* is reached: a status where all reagents are consumed and only stable products are present (if the reactions are non reversible), or where direct reaction rates are equal to reverse reaction rates. These equations are also called *elliptic*. An example of *elliptic problem* is the Laplace equation 1.27. This equation is able to describe both pure thermal and material diffusion (if described by Fick and Fourier law), under steady state assumption. For example, we can introduce the pure steady state thermal diffusion problem, used to define heat diffusion in solids:

$$\Delta T = 0 \tag{1.28}$$

Since the time derivative is absent, only BCs need to be defined in order to solve these equations. For this reason, they are also often referred to as *boundary value problems*.

Remark It is worth to note that, if we consider a 1-D steady state problem, it actually appears as an ODE, since only a single spatial derivative appears. This is a very useful tool, because, while the relative unsteady state PDE can have numerical problems or issues, ODEs are generally easier to solve. Thus, even if the original problem is introduced at unsteady state, it can be useful to solve before the steady state version, in order to deduce some preliminary information on the problem solution.

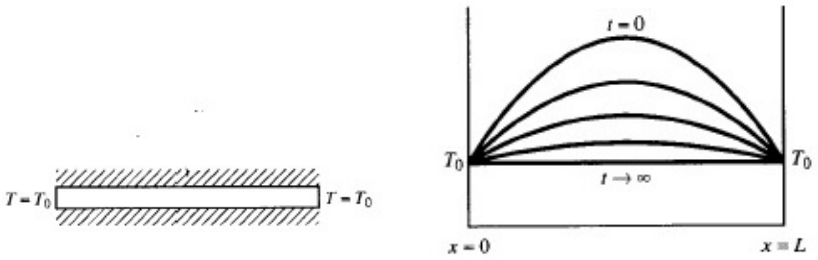

(a) *Cooling metal bar scheme* (b) *Temperature profile over time*

Figure 1.4

1.6.2 Unsteady state problems

By the other hand, unsteady state problems account for the time dependence of the solution. All the reported transport equations appear as unsteady state problems. It is possible to classify these equations in two types: *hyperbolic* and *parabolic*.

The prototype of parabolic equations is the unsteady diffusion equation:

$$\frac{\partial \phi}{\partial t} = \gamma \Delta \phi \tag{1.29}$$

In this case γ is a generic constant. Let us consider the thermal diffusion on a mono-dimensional metal bar (schematized in Fig.1.4a), where no external thermal fluxes are present ($q = 0$). We have then:

$$\frac{\partial T}{\partial t} = \alpha \frac{\partial^2 T}{\partial x^2} \tag{1.30}$$

Assuming a parabolic profile at $t = 0$, that means:

$$T(x = 0, 1) = T_0 \tag{1.31}$$

$$T(t = 0, x) = f(x) \tag{1.32}$$

Where $f(x)$ describes a parabolic temperature profile. Since no heat flux is present, we expect the bar to lower its temperature over time.

As we can see from Fig.1.4b, the temperature of the bar lowers indeed over time. As $t \to \infty$, the temperature profile flattens on T_0, imposed by the BCs.

Hyperbolic equations, instead, are typical of phenomena where dissipation effects are negligible. The most common example is the *wave equation*.

$$\frac{\partial^2 \phi}{\partial t^2} = c^2 \Delta \phi \tag{1.33}$$

c^2 is a constant, often called wave velocity. However, hyperbolic systems are typical of fluids with high velocities (such as shock-waves), where the Mach number is particularly high.

1.6.3 Geometrical classification

We introduced the terms *elliptic, parabolic* and *hyperbolic*. This classification rises as an analogy with the conic sessions (*ellipse*, *parabola* and *hyperbola*). The ellipse has a very regular and smooth shape, so elliptic problems allow for smooth solutions. Hyperbola are composed of two separate sections. Hyperbolic equations, indeed, are able to support solutions with discontinuities, such as shock-wave problems. We introduce a generic equation in 2-D domains:

$$a_1 \frac{\partial^2 \phi}{\partial x^2} + a_2 \frac{\partial^2 \phi}{\partial x \partial y} + a_3 \frac{\partial^2 \phi}{\partial y^2} + a_4 \frac{\partial \phi}{\partial x} + a_5 \frac{\partial \phi}{\partial y} + f(\phi) + a_6 = 0 \tag{1.34}$$

Assume for simplicity that $a_1, a_2 ...$ are all real constants. It is possible to show that Eq.1.34 allows for hyperbolic solutions if his characteristic equation has two real roots:

$$a_1 \left(\frac{dy}{dx} \right)^2 - a_2 \left(\frac{dy}{dx} \right) + a_3 = 0 \tag{1.35}$$

From the value of the discriminant of Eq.1.35, we can distinguish among the three classes (shown in Table 1.1).

$(a_2^2 - 4a_1a_3)$	Type of equation
< 0	elliptic
> 0	hyperbolic
$= 0$	parabolic

Table 1.1: PDE classification

State of the art

In this section we are providing a state of the art of the two presented applications: modelling and evaluating important parameters about dust explosions and characterize the behavior and the parametric sensitivity of Plug Flow Reactors. The main target of this part is to introduce the background and the reasons that give both research and practical importance to the analyzed problems, supported by a summary of relevant historical facts and specific literature studies about these topics.

2.1 Dust explosions

Before starting discussing what is a dust explosion, the concept of explosion itself should be clarified. Encyclopedias give different definitions that can be summarized in two categories. The first focuses on the strong noise or *bang* due to the sudden release of a huge pressure wave. What generated this pressure wave, whether it is related to a release of chemical or mechanical energy, is of secondary concern. This definition of an explosion matches the basic meaning of the word (*sudden outburst*)[10]. The second category of definitions is limited to explosions caused by the sudden release of chemical energy. This includes explosions of gases, dust and solid explosives. The emphasis is then often put on the chemical energy release itself, and explosion is defined accordingly. Depending on the context, both definitions can be useful in the study of dust explosions.

So, what is a dust explosion? Still in our times the concept of explosive dust like sugar, flour, and metals is not well established. Metal and organic dust, since they are made of atoms at oxidizable state, can definitely burn. If then the combustion rate is sufficiently high, and the phenomenon occurs in a confined volume, we have all the elements to produce an explosion, in the

Figure 2.1: From the classic fire triangle to the dust explosion pentagon (Source: Occupational Safety and Health Administration)

meaning of a huge pressure wave, generated by the chemical energy released by the combustion of fine, dispersed particles.[3],[10]

How does a dust explosion occur? The first required step is definitely a combustion process. In general, when talking about fires, it is common to introduce the necessary conditions to promote combustion with the classic fire triangle (Fig. 2.1): oxygen, a fuel, and an ignitions source are necessary to start a combustion event. This definition, however, applies only to gas and liquid combustibles. When talking about combustion of solids, and then dust explosions, additional conditions are required, leading to the dust explosion pentagon (Fig. 2.1). The fire triangle is complemented with *dispersion* and *confinement*. Dispersion indicates the requirement of contact between oxygen and combustible: while gases or evaporating liquids form generally a homogeneous gaseous phase, combustion of solids leads to a heterogeneous system, with solid particles dispersed in air. An immobile dust deposit does not have access to oxygen molecules, and it will be harder to be ignited. Confinement, by the other side, is a strict explosion related issue: if a violent combustion occurs in an unconfined environment, according to the perfect gases law, the burning mass will expand in volume, due to the temperature increase generated by the combustion itself. The introduction of a confinement, thus burning in a small, fixed volume, will promote an increase in the pressure of the system, until reaching overpressure that cannot be held by the confining structure, leading to the effective explosion. Also, it should be noticed that the introduction of a confinement, due to the reduction of the volume where the combustible can be dispersed, generates higher combustible concentrations in air. In factories, confinements are basically always present: pipelines, storage systems, closed rooms... Hence, explosions should never be underestimated in a real industrial environment.

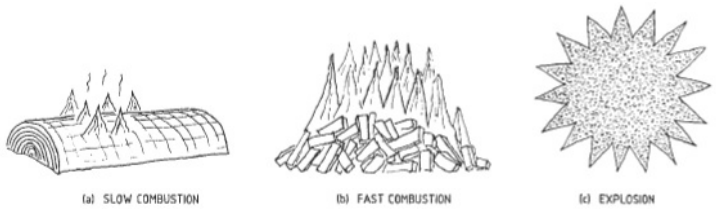

Figure 2.2: Effect of particle size on combustion (Source: Eckhoff R.,2003)

Particle size effect

A solid combustion requires contact between the involved reagents. All the combustion mechanisms that include oxygen and the solid fuel, are superficial reactions. For this reason, particle size is crucial when talking about dust explosions. It is a well-known fact that wood chips burn easier than a log. Fig.2.2 shows an example of the effect of particle size. The parameter used to describe the effect of particle size is the specific area of a particle: namely, the ratio between the surface and the volume of the particle. The ratio follows the $\frac{3}{2}$ power law: the smaller the particle, the higher the ratio. As an example, assuming spherical particles with radius r, the ratio follows this rule:

$$\frac{S}{V} = \frac{4\pi r^2}{\frac{4}{3}\pi r^3} = \frac{3}{r}$$

So, the spherical particle surface relatively increases as the radius gets smaller. This ratio has additional importance: not only smaller particles burn more violently but are also dispersed easier. Dust deposits made of small particles are more easily dispersed in the environment by air jets, blast waves and so on. This leads to easier triggering of secondary explosions.

Materials involved

Another important thing to consider is the type of dust involved. In general, any substance with atoms at not maximum oxidized state can react with oxygen. While the global reaction is always the same (fuel and oxygen to give oxides, heat and water), the mechanism is substantially different, depending on the material subject of the combustion. It is possible to classify explosive solids in the following way [10]:

- Natural organic materials (grain, linen, sugar..)

- Synthetic organic materials (plastics, organic pigments, pesticides..)
- Coal and peat
- Metals (aluminium, zinc, iron...)

Metal dusts are associated with higher combustion enthalpies (ranging between 300-2500 $\frac{KJ}{molO_2}$) than organic ones (200-500 $\frac{KJ}{molO_2}$). Pyrolysis and combustion mechanisms are substantially different depending on the material, and the specific mathematical models should be developed accordingly. This work focuses on modelling explosion of organic dust. The hypotheses based upon the proposed combustion and pyrolysis model will be discussed later.

Primary and secondary explosions

When talking specifically about dust explosions, one of the most important fact to consider is the importance of secondary explosions. Generally, when talking about the more classical gas explosions, the phenomenon is related to a distinct volume, or a portion of an industrial environment, where a single explosive effect occurs (called *primary explosion*). In the case of gases, the process equipment normally contains fuel only, with no air, and under such circumstances, gas explosions inside process equipment are impossible. Therefore, most primary gas explosions take place outside process equipment, where gas from accidental leaks is mixed with air and explosible atmospheres generated. Also, once the gas explosion occurs, the fuel itself is not present in the surroundings (unless the explosion is so violent that it causes the rupture of eventual storage systems or pipelines). When talking about dust explosions, the situation is drastically different. First, a lot of industrial processes allow dust to be regularly present in both process equipment and buildings. Imagine industrial mills: used to produce finer particles (like flour or powdered sugar), they are not isolated from the surroundings, generating thus airborne mixtures of dust and air, and dust deposits over time. Dust deposits are particularly subtle: even thin layers can contain such a high quantity of combustible material.

As an example, imagine having a 1 mm deposit with a bulk density of 500 $\frac{kg}{m^3}$, in a cubic room with 5m edge. If the dust is dispersed in a 1m height of the room, it will lead to a local $500\frac{g}{m^3}$. If the dust is dispersed in the whole

room, the final average concentration will be $100\frac{g}{m^3}$. Such values, for a lot of dust, are widely in the explosive concentration range.

If removal of dust deposits and venting are not adequately carried out, the whole facility becomes a potential bomb. Indeed, as it will be highlighted in the following case histories report when a dust explosion occurs, we generally have a primary event, that in general has not the potential of causing severe damages. But then, the propagation of blast waves and flames can promote the entrainment of dust deposits, lying dormant, generating several secondary explosions.

2.1.1 Modelling dust explosions

In order to completely understand the extent of dust explosions, a lot of mechanisms, effects, and physical phenomena must be studied. As pointed out by Eckhoff [10], the fundamental aspects of dust explosions can be summarized as in Table 2.1. Developing a complete predictive model on dust explosions requires to model and know all the just presented aspects, and it is still a challenging topic. Over time, a lot of dedicated studies and researches have been performed.

In order to describe the generation of dust clouds, Lightstone and Raithby presented in 1998 [17] a mathematical model that predicts the motion of particles in a turbulent flow. The model was based on solving the probability density function of particle velocity and treats the impact of the velocity probability density function as a diffusion process. The model gave good agreement between predictions and experimental data. The available model are based upon strict hypotheses, due to extreme complexity of the phenomenon. [10] provides a detailed collection of former studies on dust explosions.

More recently, in 2005, a CFD (Computational Fluid Dynamic) software has been developed to model dust explosions, named DESC (Dust Explosion Simulation Code) [20]. Still today, this is the only known CFD software dedicated to modelling dust explosions.

In the latter years, several works have been dedicated to estimating the effect of particle size on important dust explosion parameters, such as the k_{ST} [63] [61].

Dust cloud formation process	**Dust cloud ignition process**	**Flame propagation processes in dust clouds**	**Blast waves generated by burning dust clouds**
Interparticle forces in dust deposits (dispersion)	General ignition theory	Single-particle ignition and combustion in a hot oxidizer gas	Blast wave properties as a function of burning dust cloud properties
Entrainment of particles from dust deposits by shock waves passing across the deposit surface	Ignition of single particles and clouds	Laminar and turbulent flames in dust clouds	Effects of blast waves on humans and mechanical structures
Entrainment of particles from dust deposits by turbulent gas flows	Ignition by smoldering combustion in dust layers and deposits	Mechanism of heat transfer:conduction, convection, radiation	Ability of blast waves to transform dust layers into dust clouds
Transport of gas particles in turbulent gas flows	Hot surfaces	Limit conditions for flame propagation through dust clouds: particle properties, dust concentration,oxygen concentration, geometry	
Measurement and characterization of state of turbulence in dust clouds	Flying burning metal particles	Acceleration of dust cloud flames by turbulence	
Measurement and characterization of distribution of particles in dust clouds	Electric sparks and arcs	Detonation of dust clouds	
	Electrostatic discharges		
	Hot gas jets		
	Shock waves		
	Focused light-beam hot spots		
	Influences on ignition sensitivity of dust cloud properties:composition, size and shape of particles,turbulence, dust concentration,gas phase composition		

Table 2.1: Fundamental aspects of dust explosions mechanisms (Eckhoff, 2003)

2.1.2 Case histories

Unfortunately, dust explosions are still a not well-known argument, especially in the real industry field. In a lot of cases, only those who have experienced a dust explosion in their own plant, whether workers or management, have a much more deep appreciation of the concreteness of this hazard than those who only heard or read about dust explosions in general terms. Constant efforts in real understanding, with the cooperation of scientific research, industry, and both national and international association dedicated to industrial safety, will result in increasing the groper motivation for minimizing the probability of occurrence of such events in the future. The use of case histories is one of the most efficient ways to emphasize the importance of dust explosions, that is, a fairly detailed collection of dust explosions that actually occurred elsewhere. The problem of this strategy is that it takes into account only big accidents: minor accidents, that cause low damages to both personnel and plants, are often not considered and kept unspoken. Extremely severe industrial accidents, due to the massive impact of the phenomenon, come off as an extremely unfortunate source of information, and motivations to improve industrial safety. By the other hand, it is important to notice that while small accidents are in practice unavoidable, they often are symptoms of an "ill" system, and should never be underestimated. The collection of accidents presented in this part will consider events occurred over the years and over the world, covering the last 50 years, and various types of explosive dust.

Explosion of a flour warehouse (Italy, 1785)

From the scientific literature point of view, this can be considered the historical starting point of the field of dust explosions. On the 14th December, 1785, around six o'clock in the evening, an explosion of wheat flour took place. The event occurred in Mr. Giacomelli bakery, and after it windows frames of the building where found on the street. All the information about this event is known thanks to the work of Count Carlo Lodovico Morozzo (1743-1804), president of the *Accademia delle Scienze di Torino*, who made a detailed report on the accident [19]. A tentative reconstruction of the accident is given in Fig. 2.3.

It is important to notice how Count Morozzo introduced in his report the importance of improving the understanding of the dust explosion phe-

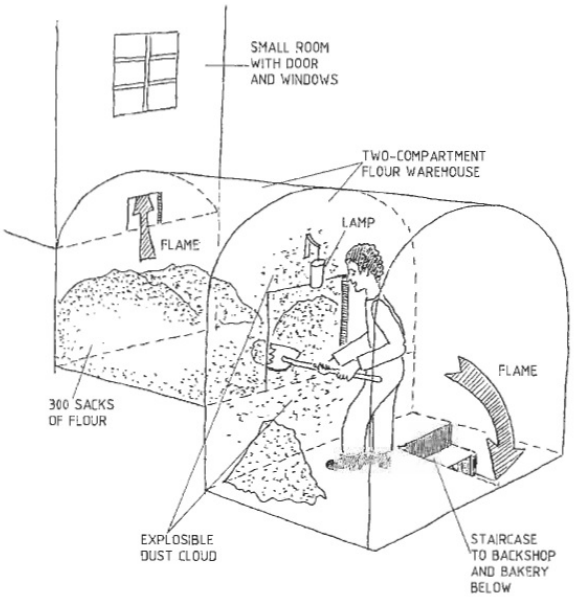

Figure 2.3: Potential reconstruction of the scene of wheat flour explosion in Mr. Giacomelli's bakery, based on count Morozzo report (Source: Eckhoff R., 2003)

nomenon, starting the scientific literature about this fascinating argument.

Explosion of a wheat grain dust silo (Norway, 1970)

In 1970, a wheat grain explosion occurred in Stavanger (Norway), in a silo property of the Norwegian Grain Corporation. The event took place in a hot and dry summer day. No casualties have been reported, but some severe burns affected some workers. The explosion lasted for about 25-30s, and according to witnesses, six or seven distinct explosions have been recognized. The flame was capable of propagating for a total distance of about 1500 meters, through a number of bucket elevators, horizontal conveyors, ducting, filters, and rooms in the building. This facility was constituted by many large and small silos (the capacity of silos ranged between 50 and 2000 m^3), with a total number of more than 20 storage buildings.

One of the most interesting facts about this accident, despite dust explosions occurred in more than 10 silos, only one resulted badly damaged by the event (notable in Fig.2.4). This silo was unvented, with a storage volume of 2000 m^3, and had its roof blown up. Considering this, it is clear that the maximum explosion pressures in all the other 21 silos, both vented and unvented, were actually below the threshold of 0.2 bar(g), which would be required to blow up the actual type of silo roof. The source and initiation of this accident are yet unknown. Two main hypotheses have been proposed. The first one identifies the self-ignition of a dust deposit in the boot of an elevator, where the explosion was supposed to trigger. The self-ignition process has been justified by the contact with a hot bucket. This bucket would have been heated by repeated impacts until it finally loosened and fell into the dust deposit in the elevator boot. The second theory claims that a certain chain of events lead to the ignition. The starting event was the welding on the outside of the grain feed duct to one of the elevator boots. Due to efficient heat transfer through the duct wall, the heat would have promoted the ignition of a possible dust deposit on the inside of the duct wall. Lumps of the smoldering deposit could then have loosened and been conveyed into the elevator boot, where the primary explosion took place.

Inland grain terminal (United States, 1980)

In 1980, at St. Joseph, Missouri, a dust explosion interested an inland grain terminal. The event happened in the afternoon, involving one casualty and

Figure 2.4: Picture of the silo roof after the wheat grain explosion (Source: Eckhoff R.,2003)

Figure 2.5: Picture of the air shaft along the damaged walls of reinforced concrete silo cells of the grain terminal (Source: Eckhoff R.,2003)

four injured. The economic damage was estimated around US$ 2 millions[16]. The whole facility reported structure damage, with more severe consequences on the silos. Their roofs were blown up. Casings of all bucket elevators, steel as well as concrete, had opened up in many places. Fig. 2.5 shows the air shaft, where the gallery wall and roof had been completely destroyed, leaving only the reinforcing rods. Some concrete fragments were found about a hundred meters into the adjacent railway yard.

Atomized aluminum powder explosion (United Kingdom, 1983)

In July 1983, a severe explosion occurred in the aluminium powder production plant of Anglesley, UK. Fig. 2.6 shows the layout of the plant. Molten aluminum coming from the furnaces was broken into small droplets by a jet of air. The aluminum powder so formed was carried by a current of air along sections of horizontal ducting at ground level before entering a riser that delivered it to a double stage collecting system. Two parallel collector streams were present. After the powder had been effectively separated, the air passed through a fan and out to the atmosphere via a vertical stack. The powder dropped through rotary valves into a "Euro-bin", one for each stream. When full, the bins were transported along a covered walkway from beneath the collector to the screen room, where the aluminum powder was separated into particle-size fractions. The collected fractions were bagged in the bagging room, and the powder was then taken to the storeroom.

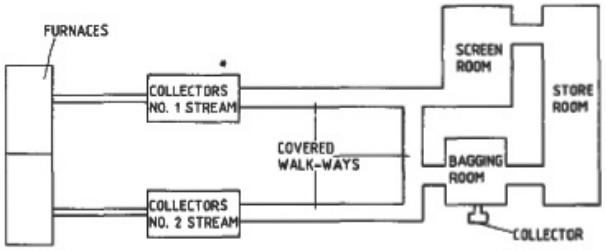

Figure 2.6: Scheme of the atomized aluminium production (Source: Lunn G.,1984)

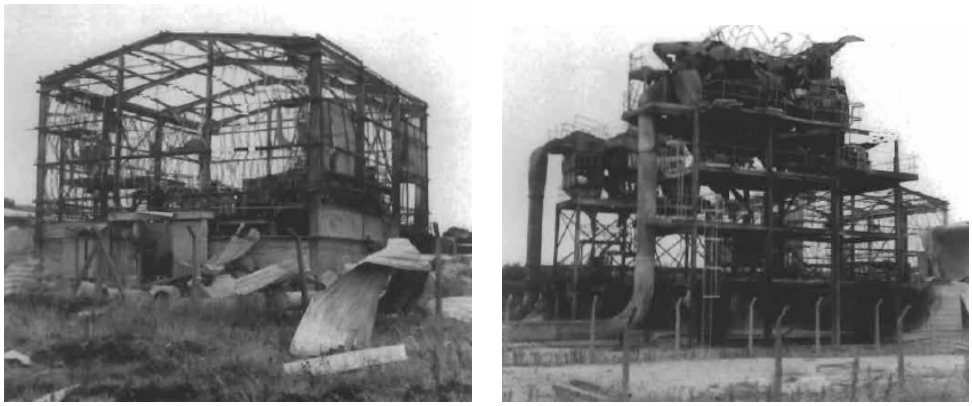

(a) *Picture of the screen room after the explosion*

(b) *Picture of the stream collectosr after the explosion*

Figure 2.7: Some pictures of the plant after the accident (Source: Lunn G., 1984)

The explosions involved the entire facility. Fig.2.7a shows the remains fo the store room after the accident, and Fig.2.7b shows the damages on the no.2 stream collectors. Still, the ignition source and the location of the ignition are not known [18]. From witnesses, it was known that the only the no.1 stream was active at that time, indicating the only option for the explosion trigger. From the picture ,it can be deduced that ignition could have occurred either before or within the first stage of the no. 1 stream collectors. Air blasts from the primary explosions then stirred up dust deposits in the walkways and screen room, allowing the flame to propagate into these areas, leading to secondary explosions.

Figure 2.8: Picture of the Imperial Sugar plant after the accident (Source: CSB, official website)

Imperial Sugar Refinery (United States, 2008)

On February 7, 2008, a huge explosion occurred at the Imperial Sugar refinery northwest of Savannah, Georgia, causing 14 deaths and injuring 38 others. This accident has been deeply studied and analyzed by the U.S. Chemical Safety and Hazard Investigation Board (CSB), an independent American federal agency charged with investigating industrial chemical accidents. It has been considered the deadliest dust explosions accident in the last decades. In this case a massive explosion of sugar dust was triggered, which aftermaths are shown in Fig. 2.8. Walls of the building blew up, equipment were completely destroyed, and the entire structure was engulfed by fire. After the accident, it was evidenced that the facility presented important accumulations of sugar dust and spills of granulated sugar were spread through the whole building. Thus, both working stations, corridors, and equipment were a massive source of combustible material, giving the base for a catastrophe of this magnitude.

Granulated sugar from the refinery was collected in three 100-foot (around 30.5m) tall silos. The granulated sugar was then conveyed into packaging buildings, where it was prepared for distribution. Some of the granulated sugar was destined to other productions, such as brown sugar or powdered sugar. During transport operations, mainly on conveyor belts, sugar would spill and disperse in the environment, generating dust deposits. Also, in order to produce powdered sugar, hammer mills were used, leading to even

finer particles dispersed in the plant. Dust collection systems were installed in the plant, but it was noticed that they were undersized. However, the dust collection system did not include conveyor belts and elevator buckets. Sugar deposits were not subject of scheduled cleaning operations. Instead, in order to clean deposits on equipment, the workers could use compressed air to remove them. This operation, though, just contributes to increasing dispersion of particles in the air, promoting optimal conditions for dust explosions.

The ignition source came from a sudden equipment change. In the tunnel beneath the sugar silos, the sugar was conveyed into a long steel conveyor belt. The sugar was sent to the belt through chutes. Eventually, some dust accumulation at the end of the chutes would clump, and block the regular flow of sugar over the belt, with spillage of sugar on the floor. The tunnel was adequately ventilated, so the sugar dust concentration in the air was kept under safe values. In 2007, the company decided to close this conveyor belt, with stainless steel panels, in order to reduce sugar contaminations. This lead to the possibility of formation of confined dust explosive mixtures. On the day of the accident, a sugar clump on a chute caused to the generation of an explosive sugar inside the conveyor belt, now confined by the recently installed panels. Under this conditions, an overheated bearing promoted the self-ignition of the dust cloud, triggering the primary explosion, that then spread through the wall building, using all the dust deposits, shaken by the already occurring explosion, to promote secondary events.

Aluminium-alloy dust explosion (China, 2014)

In 2014, a catastrophic dust explosion occurred at Zhongrong Metal Products Company, a large industrial plant for polishing various aluminium-alloy parts in Kunshan, China. The explosion occurred during manual polishing of the surfaces of aluminium-alloy wheel hubs, destined for the car industry. The accident registered 75 almost instant casualties and 185 persons were injured. Subsequently, 71 of the seriously injured also died, which increased the total victims to 146. The economic loss was estimated around 351 million Yuan. This is probably one of the most serious dust explosion catastrophes known. Fig. 2.9 provides a glimpse of the consequences of the explosion, giving a comparison of the plant before and after the aluminium dust explosion.

In the morning of August 2, at about 7:34 a.m., when normal polishing activity has been going on for half an hour, a strong explosion occurred. From the record of a video camera located outside another factory building

(a) *Workers in standard operating conditions*

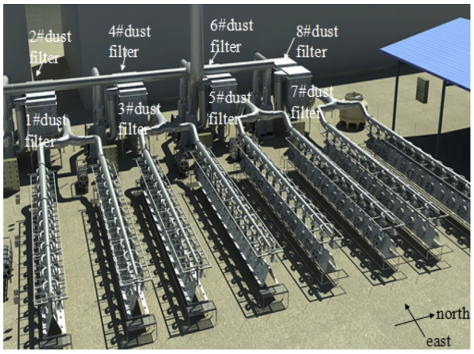

(b) *Sight of the polishing plant*

(c) *Second floor after the explosion*

(d) *A wall of the facility destroyed by the catastrophe*

Figure 2.9: Some pictures of the plant before and after the accident (Source: Eckhoff R., 2015)

about 500 m away from where the first explosion occurred, it was revealed a sequence of multiple explosions lasting for about 5-7 s, including a distinct series of 8 successive explosions [11]. These 8 explosions were identified as the well-known "mushroom-shaped" dust/smoke clouds, coming from each of the 8 dust collectors (located outside the building). It was also reported that all the windows in the first floor of the building that exploded were shattered and blown to the outside. The window frames recovered were completely deformed. Fig. 2.9d shows the southern part of the plant, completely collapsed. Almost all process equipment in the factory was destroyed as dust filters. It was noticed that the dust filters that collected the dust from the first floor were more damaged than the ones dedicated for the second-floor dust. In particular dust filter #1 was blown entirely apart.

The facility included 32 polishing production lines (16 lines on the basement and 16 lines on the first floor). Along each line there were 12 working stations, as indicated in Fig. visible in Fig. 2.9a. On the day before the accident, 29 production lines were operating in normal conditions, 13 on the basement and 16 on the first floor. 348 workers were on duty [11]. As already noted, 8 sets of dust collection systems were installed outside the main factory building. The bag filters in the dust collectors were cleaned by mechanical shaking at intervals. According to survivors interviews, due to the breakdown of the electric motor, the automatic shaking systems were out of service for a long period of time. For this reason, workers had to shake the bags manually every morning in order to work.

The reconstruction of the accident was based upon retrieving the necessary conditions that can promote a dust explosion.

Exploding material and oxidizing atmosphere It was clear that the only candidate that could bring to such a serious event was the aluminium dust produced during the polishing of aluminium alloys hubs. Aluminium dust deposits where present in the whole area, and in the 8 collectors outside the factory. Aluminium is a metal, and, under the right conditions, can burn in presence of oxygen and water. All the pipelines and the dust collectors were not isolated properly, so air was regularly in contact with dust. Water can play a significant role in the self-ignition of metal dust deposits and it has already studied and proved in previous studies [7], and confirmed in this accident reconstruction [11]. The presence of water, as it will be explained later, was given by rains a couple of days before the accident occurred.

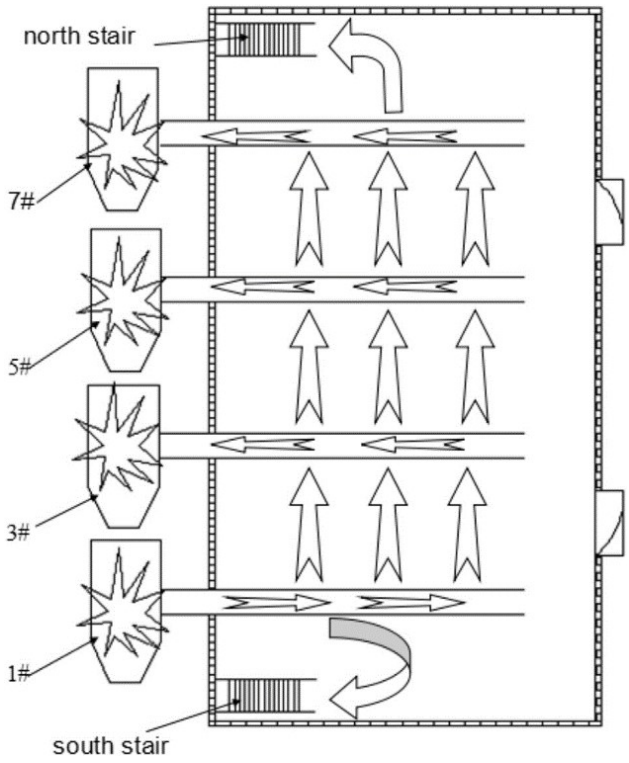

Figure 2.10: Reconstruction of the blast wave propagation (Source: Eckhoff R., 2015)

Initiation Based on the severity of the damages reported on the process equipment and on the video camera records, it was determined that the most likely place where the primary explosion started was the #1 dust filter. From there, the dust flame propagated, upstream inside the dust extraction duct and it entered the first-floor working lines, from where it exited into the workrooms via the dust extraction hoods above the working stations, and eventually ignited the dispersed deposited dust on the floor around the production lines, causing major secondary explosions. Then these explosions and associated dust flames propagated the entire length of the first floor and got sucked into the dust extraction ducts leading to the second floor, where additional explosions occurred [11]. Fig.2.10 shows the most probable propagation of the blast wave started from the #1 dust filter.

Figure 2.11: Picture of the dust collecting barrel of the #1 filter (Source: Eckhoff R., 2015)

Ignition Still, it is not known how the first explosion occurred. Several options have been tested, starting from hypothesizing mechanical friction in the dust filters, due to the cleaning system. As already recalled, the cleaning system was in fault state at that time, and also it was calculated that the eventual aluminium concentrations were not able to sustain an explosion. As mentioned before, water can promote oxidation of metals. Also, it was noticed (Fig. 2.11) that the dust collecting barrel of the #1 filter reported a corroded hole at the bottom. With an experimental procedure, it was demonstrated that, in combination with water, the aluminium deposits in the barrel could reach the self-ignition temperature [11], thus leading to the following explosions. The hole in the barrel was probably due to long-time corrosion, and water could penetrate inside because of the recent rains. In conclusion, the explosion started from the self-ignition of the aluminium dust deposit located in the #1 filter.

Additional information was collected about the plant management:

- Dust explosions events were not considered in the facility risk analysis, justified by the relatively low amount of material involved
- Regular cleaning of dust deposits in the workstations was not scheduled
- The venting system was not adequately designed
- Dust filters and pipelines were not isolated

This accident, unfortunately, teaches that still in recent times dust explosions are not yet properly considered. Even relatively small amount of dust can

cause severe explosions. Also simple and small actions, like regular cleaning of dust deposits, can effectively prevent events like this.

2.1.3 Important parameters in dust explosions

Over the years, assessing the explosivity of dust deposits has become a crucial aspect in the industry. Due to the complexity and variety of its aspects, it is important to ease the burden of efforts that need to be done for dust explosion prevention. For this reason, defining significant parameters that allow for accounting the risks associated with a dust sample has become the mainstream approach in this field. A specific parameter, in this sense, is basically a number that can be used to establish whether or not a situation is potentially dangerous, and it can be used for designing proper safety or venting devices. Historically, these parameters have been studied mainly in experimental tests [9], leading to the definition of national and international standards and associations dedicated to this topic (such as NFPA (National Fire Protection Association), ATEX directive, EN and ASTM standards).

Defining a parameter is already by itself a complex task: since it is generally a number, it necessarily condenses a lot of information. Introducing a parameter requires deep researches and analysis before it is considered a significant source of information. For this reason, we will consider elements that are actually used in risk prevention and globally acknowledged as good indicators of explosive dust characteristics.

Once a parameter is defined, it is also necessary to evaluate it. From there, it is possible to move in two directions: study and develop proper experimental tests, or promote the introduction of predictive mathematical models. The modelling approach is definitely of a noble intent, since it requires the understanding of all the involved phenomena. However, it is not always feasible: the mathematical problem may not have a resolution (think about the Navier-Stokes equations), and often the closure of a balance is done with relations that require new parameters (like in the constitutive relations). For this reason, experimental tests are still today the most reliable and "easy" way to estimate a parameter. They do not come without errors: the experiment is always subject to both human and intrinsic errors, giving misleading results. In general, this is overcome with multiple tests (that leads to more expensive procedures). Also, an experimental test is often felt more reliable than "cold" mathematical predictions.

Particle size distribution and specific surface area

Particle size is crucial to address solids combustion. Several methods are reported to evaluate the particle size distribution of dust [2]:

- Sieving (woven-wire and electroformed micromesh)
- Microscopy (light microscopy, transmission electron microscopy (TEM), and scanning electron microscopy (SEM))
- Sedimentation in liquids (incremental and cumulative, gravitational and centrifugal)
- Electrical sensing zone
- Light scattering
- Permeametry and gas diffusion
- Gas adsorption

Some methods provide the full particle size distribution, others estimate an average particle size, representing the overall mass. The selection of a proper method to provide particle size distribution should be underestimated.

Minimum Ignition Temperature of dust clouds

In industrial environment, hot surfaces are common: furnaces, ovens, reactors can heat by convection dust clouds and dust deposits. At the right temperature, the dust cloud is able to self-ignite, generating the primary event. The MIT is determined by using furnaces, such as the Godbert-Greenwald furnace: a dispersed dust cloud is sent in a cylinder at a known temperature. The temperature is increased by steps, until the dust cloud ignites.

Minimum Electric Spark Ignition of dust clouds and layers

Sparks are between the main triggering event of dust explosion. Friction due to metal parts contacting, an impact of falling objects on metal surfaces, moles... Sources for sparks are countless. Even in this case, the determination of these parameters is mainly performed with experimental tests, imposing sparks on a dust cloud or a dust layer, depending on which datum is required.

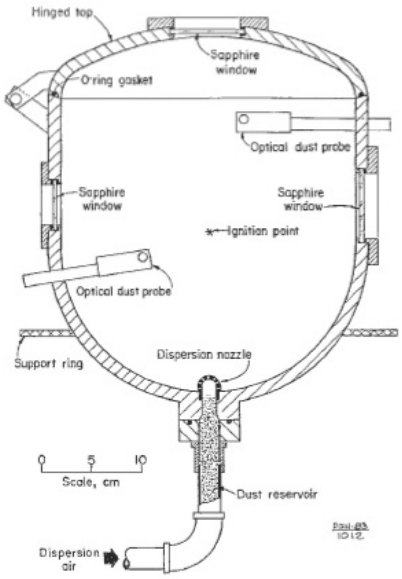

Figure 2.12: Cross section the 20 liter explosion vessel for determination of the minimum explosible concentration (Source: Cashdollar and Hertzberg, 1985)

Minimum Explosible Dust Concentration

A dust cloud cannot propagate a combustion flame if the particles are not enough concentrated. This means that theoretically, if dust clouds are kept below proper thresholds, dust explosions could be prevented a priori. The experimental test is quite intuitive: a fixed amount of dust (that is directly related to the dust cloud concentration) is dispersed and ignited inside a vessel. Starting from small amounts, more and more dust is loaded until the mix effectively ignites, marking the Minimum Explosible Dust Concentration. Estimation techniques have been studied by Dorsett in 1960 [8], and then by Hertzberg et al. in 1979 [13]. in 1985 , Cashdollar and Hertzberg [14] developed a 20 liter explosion apparatus, represented in Fig.2.12.

Maximum Explosion Pressure at constant volume

Overpressure generated by dust explosion is an important parameter: it is the property that effectively decides if an equipment or pipeline will burst, and it is greatly enhanced by confinement. Experimental tests are still the

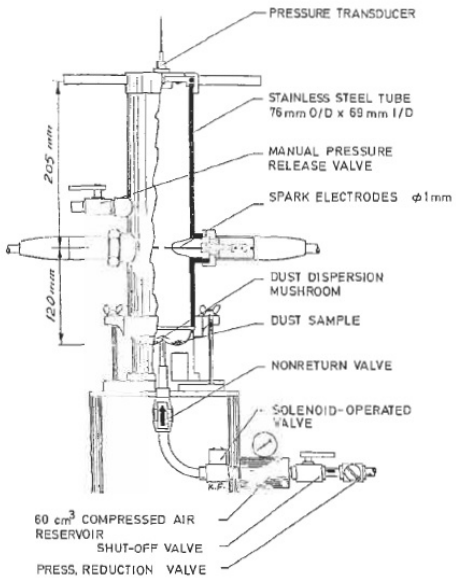

Figure 2.13: Sketch of a 1.2 liter Hartmann bomb (Source: Eckhoff R., 2003)

mainstream technique applied to determine it. All the procedures follow more or less the same pattern, and they are carried out inside specifically designed devices (called *bomb*):

1. Load a certain amount of dust inside the bomb
2. Activate a jet of air that promotes dust dispersion
3. Ignite the dust cloud (generally by spark ignition)
4. Read the maximum overpressure after the experiment

Hartmann bomb The Hartmann bomb, described by Dorsett et al.[8], has been used throughout the world to estimate the maximum explosion pressure of dust clouds for nearly half a century. This apparatus, which is illustrated in Fig. 2.13, basically consists of a closed vertical 1.2 liter stainless steel cylinder into which a known quantity of dust is dispersed as a cloud by a blast of air and exposed to an ignition source. The pressure profile is recovered by the pressure transducer. The drawbacks of this system are related to its small volume. Indeed, the overpressure determined with this

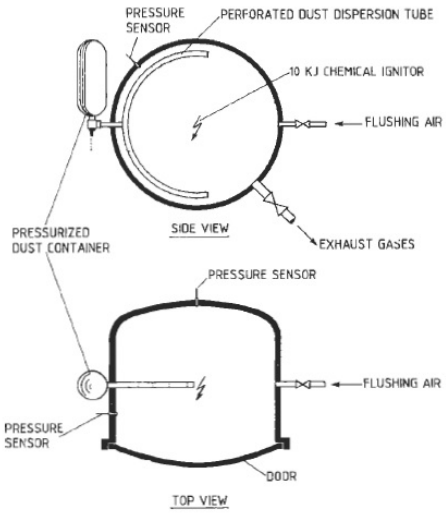

Figure 2.14: Sketch of a standard 1 m^3 vessel (Source: Eckhoff R., 2003)

device is in general 25-30% lower than the results of bigger apparata, such as the 1 m^3 vessel [10].

1 m^3 standard ISO vessel The 1 m^3 ISO vessel is a bigger bomb, as shown in Fig. 2.14. A container of approximately 5 liters capacity and capable of being pressurized with air until 20 bar is attached to the explosion chamber. The container is fitted with an opening valve that can open in 10 ms. The container is connected to the explosion chamber via a perforated semicircular spray pipe. The ignition source is a pyrotechnical ignitor with a total energy of 10kJ and it is set afire after a fixed delay of 0.6 s after onset of dust injection. The total mass of ignitor used is 2.4 g, and its composition is the following: 40% zirconium, 30%barium nitrate, and 30% barium peroxide. The results of this system are more reliable than the ones of the Hartmann bomb, due to the major volume implied, but they are quite similar. Due to the bigger volumes, this procedure is also more expensive.

20L Siwek sphere This smaller bomb (shown in Fig. 2.15), has been designed by Siwek (1988), in order to produce the same result of the 1 m^3 vessel. This sphere is basically a smaller version of the 1 m^3 bomb. The ignition conditions are the same, and good results have been obtained between

Figure 2.15: Picture of a 20L Siwek apparatus

the two bombs [10].

Maximum Rate of Rise of Explosion Pressure at a constant volume

This is one of the most important parameter when talking about explosions, because it quantifies the explosion violence [15], that is, the rate of heat generation inside the enclosure where the explosion is initiated. Its estimate is crucial for a proper design of equipment aimed to protect the industrial process from dust explosions. This parameter is called k_{ST}, and it will also be the subject of this work. It is defined with the "cubic root law", introduced by Bartknecht [4],[5] [6]:

$$V^{\frac{1}{3}} \left(\frac{dp}{dt}\right)_{max} \qquad \left[bar\frac{m}{s}\right] \tag{2.1}$$

p is the pressure and V is the volume where the explosion takes act. Fig. 2.16 shows an intuitive example of what k_{ST} is: the maximum slope of the curve $p-t$, namely the time when the pressure rate is at its highest.

Occupational Safety and Health Administration produced a list of hazard classes of explosive dust based on the k_{ST} values, shown in Table 2.2.

The experimental tests are the same used for the estimation of maximum pressure, since the pressure transducer produces already a $p-t$ curve at the end of the test. This parameter highly depends on the type of dust cloud, with a remarkable dependence upon particle size distribution. Fumagalli et

Hazard class	$k_{ST}[bar\frac{m}{s}]$	Type of explosion
St0	0	No explosion
St1	< 200	Weak explosion
St2	$201 - 300$	Strong explosion
St3	> 300	Very strong explosion

Table 2.2: Hazard class of explosible dusts (Source: OSHA CPL 03-00-008)

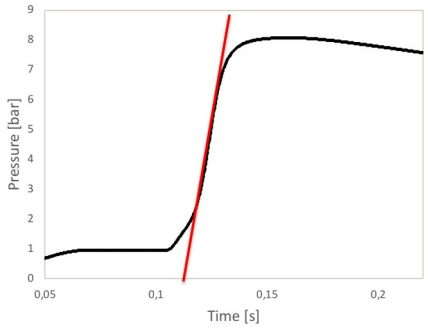

Figure 2.16: Typical evolution of a pressure profile during an explosion (the slope of the red line is the k_{ST})

al. recently published a detailed review [12] on the major techniques and criticalities about k_{ST} estimation.

2.2 Runaway Boundaries for PFRs

During the history of reactors, the constant work and efforts allowed the identification of runaway boundaries and the optimization of process safety. Before the establishment of a rigorous classification and mathematical modelling of chemical reactors, most of the industrial processes (such as synthesis of sulfuric acid, soap and synthetic rubber, production of nitrogen, and so on) were designed and put into operation based only on laboratory experimentations. Moreover, the industrial syntheses were mostly carried out in batch reactors. In the first decades of 1900, the concepts of unit operations, reactors classification and so on arose, leading to a growing interest in the

mathematical modeling of chemical processes. In particular, since most of the industrial syntheses of interest (like the production of sulfuric and nitric acid, nitrations, sulfonations, etc...), were fast and strongly exothermic, there was interest in characterizing the thermal stability of the synthesis reactor (in order to prevent the triggering of runaway phenomena and consequent accidents). The first scientists who investigated potentially runaway reactions systematically were Semenov, Todes, and Frank-Kamenetzkii [37]. They are actually acknowledged as pioneers because they tried to describe in a rigorous procedure both the phenomena of the self-heating and the explosion-like temperature rise in a reacting system. The criteria derived from their studies are still used today and set the basis for any safety assessment involving chemical reactors. According to Semenov theory, cooled batch processes could be operated safe under normal operating conditions (upset operating conditions had not been taken into account) only if the reactions were moderately exothermic and proceed slowly (we can consider a reaction rate slow if its characteristic time is around 20 times higher than that time of the cooling). Just before and during the years of the Second World War, a lot of studies were aimed to define general models to define runaways in a generic chemical reactor, in order to identify the most performing apparatus for a given reaction of interest. Particularly, continuous reactors such as Continuously Stirred Tank Reactors (CSTRs) and Plug Flow Reactors (PFRs), due to their major production, were extensively analyzed by mathematicians and physicists concerning all the aspects of their thermal stability. Unfortunately, numerical calculations were far from being performed, therefore, scientists focused their attention on CSTRs rather than PFRs, since they can be described (in the steady-state operation) by algebraic equations. In 1956, Bilous and Amundson published a work concerning the stability and sensitivity of a tubular reactor (PFR) [24]. As they noticed, a mathematical approach similar to that one used for CSTRs, that is using the perturbation method, was not applicable because it would have led to writing a system of partial differential equations. At that time, the solution of PDE system wasn't numerically feasible, therefore they moved toward a new approach: they introduced, for the first time, the concept of parametric sensitivity. The parametric sensitivity is defined as the system sensitivity behavior with respect to changes in its parameters. By changing these values, the system can answer with desired or undesired behaviors. When a system operates in the parametrically sensitive region, its performance becomes unreliable and a small variation of the input parameters translates into a big variation of

output parameters. In order to detect runaway boundaries, they considered the thermal response of the system, represented by the steady-state temperature profile along the reactor length, as the target behavior to be analyzed as a function of the variation of some model parameters. Their approach was very rigorous since they analyzed both sinusoidal and step like parameters variations: anyway, the conclusion was that the two methods led to the same results in terms of reactor parametric sensitivity. They studied the changes of the reactor temperature and concentration profile as a function of perturbations of different model parameters, like reactor wall temperature, inlet reactant concentration, global heat transfer coefficient, etc.., and their conclusion was that a parametric sensitivity region could exist. In 1959, Barkelew [23] tried to find a simple criterion for a PFR, starting from the observation that the equations describing its steady-state behavior are not substantially different with respect to the ones of a BR: time is basically replaced by the axial coordinate of the tubular reactor. In particular, he observed that regions of remarkable parametric sensitivity with respect to the initial temperature and the cooling efficiency could be easily recognizable simply looking at the temperature vs. time (or axial coordinate) profiles and, using such an observation, he was the first who differentiated between sensitive and insensitive operating region of a BR/PFR.

We start with mass and energy balance for a batch reactor:

$$\frac{dC}{dt} = -k(T) \cdot C^n \tag{2.2}$$

$$\rho \cdot c_p \cdot \frac{dT}{dt} = -\Delta H \cdot k(T) \cdot C^n - UA \cdot (T - T_{cool}) \tag{2.3}$$

With initial conditions

$$C(t=0) = C_0 \qquad T(t=0) = T_0 \tag{2.4}$$

We can the introduce the following quantities:

- Maximum temperature rise ΔT_{max}

$$\Delta T_{max} = T_{max} - T_{cool} \tag{2.5}$$

- Dimensionless temperature rise θ_{max}

$$\theta_{max} = \frac{E_{att}}{R \cdot T_{cool}^n} \cdot T_{max} - T_{cool} \tag{2.6}$$

- Reacting strength S

$$S = \frac{-\Delta H \cdot C_0}{\rho \cdot c_p \cdot T_{cool}} \cdot \frac{E_{att}}{R \cdot T_{cool}} \tag{2.7}$$

- Cooling intensity N, that is an alternative formulation of the Semenov number

$$N = \frac{U \cdot A}{\rho \cdot c_p \cdot V \cdot k_0 \cdot exp\left(\frac{E_{att}}{R \cdot T_{cool}}\right) \cdot C_0^{n-1}} \tag{2.8}$$

Observing Fig. 2.17, it is possible to notice that the maximum reactor temperature with respect to the coolant temperature shows a sharp transition in correspondence of a particular value of the cooling intensity (that is, it exhibits a huge parametric sensitivity behavior). Barkelew created two different types of diagrams in order to differentiate between insensitive and sensitive operating region for a BR .In the first diagram, he represented the thermal behavior of the system (θ_{max}) as a function of the cooling intensity and the reaction intensity; in the second one, he shows the sets of (S, N) separating the insensitive from the sensitive operating region. Particularly, looking at Figure 2.18, Barkelew showed that all of the curves there represented possessed a common tangential envelope. The points on this envelope could be reported in terms of N, S vs. S couples in order to generate a curve that separated sensitive and insensitive regions of BR operation. All these considerations, as already stated, have been easily extended by Barkelew to PFR using the analogy in between time and axial coordinate (initial and inlet concentrations/temperature, etc ...). Of course, such an approach has strong limitations that will be discovered decades years later. After the studies performed by Barkelew, it was clear that a profound analogy in between the mathematical modelling of batch and plug flow reactors could be established. Therefore, since continuous processes had become a common application for high productivities for a variety of chemical compounds, chemical engineers started to improve the modelling for the detection of the runaway boundary for BRs with the main aim of effectively extending the theory to PFRs.

In 1964, Dente and Collina [27], referring to the thermal stability of PFRs, published a criterion of intrinsic nature that defined the runaway boundary as a critical condition in correspondence of which the temperature vs. axial coordinate profile exhibited a region with positive second-order derivative

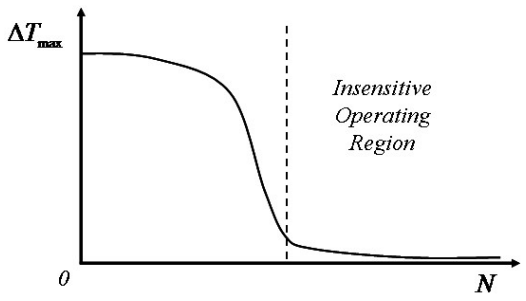

Figure 2.17: Sensitivity of the maximum temperature rise as a function of the cooling intensity N [23]

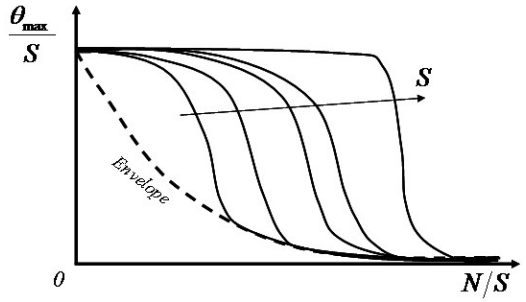

Figure 2.18: First Barkelew diagram showing that all the sensitivity curves have a common envelope [23]

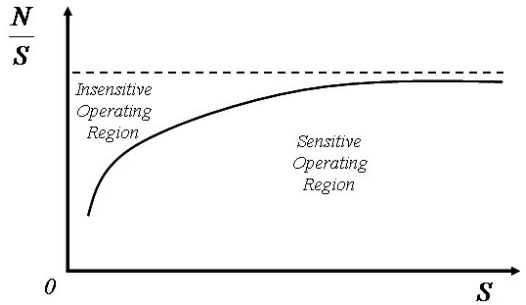

Figure 2.19: Second Barkelew diagram differentiating between sensitive and insensitive operating conditions [23]

(that is, concave profile) somewhere before the hot spot. Superimposing that such a region had to have zero amplitude, the following critical conditions were defined:

$$\frac{d^2\theta}{dz^2} = \frac{d^3\theta}{dz^3} = 0 \tag{2.9}$$

Although developed independently this criterion is identical to that of Thomas for batch reactors [35], with the only difference that was the time replaced by the axial coordinate.

In 1966, Dente and his co-workers published some study [28],where they investigated the runaway behavior of a tubular reactor (PFR) in which two parallel or consecutive reactions occurred. The criterion used in their studies was the same that they had previously proposed for single reactions: it was still based on the reactor behavior in the temperature vs. axial coordinate plane (see Eq. 2.9). After the collection of several sets of reactor numerical simulations, it was observed that a runaway of the outlet yields and selectivity occurred whenever a thermal runaway phenomenon was triggered.

2.2.1 Theories in the '70s

Some years later, in 1970, van Welsenaere and Froment [36] published a work in which they presented two intrinsic criteria for the identification of the runaway boundary. Particularly, they referred to a gas-solid tubular reactor (PFR) where a single irreversible reaction of the first order occurred (reactor walls are considered at a fixed temperature and with densities independent of the temperature) according to the following equations:

$$\frac{dp}{dz} = -A \cdot p \cdot exp\left(-\frac{a}{T} + b\right) \tag{2.10}$$

$$\frac{dT}{dz} = B \cdot p \cdot exp\left(-\frac{a}{T} + b\right) - C \cdot (T - T_w) \tag{2.11}$$

Where

$$A = \frac{M_w \cdot P_T \cdot \hat{\rho}_s \cdot p_0}{\rho} \qquad B = \frac{(-\Delta H) \cdot \hat{\rho}_s \cdot p_0}{c_p} \qquad C = \frac{4U}{c_p \cdot d_T} \qquad z = \frac{l}{v} \tag{2.12}$$

With initial conditions:

$$p(z=0) = p_0 \qquad T(z=0) = T_0 = T_w \tag{2.13}$$

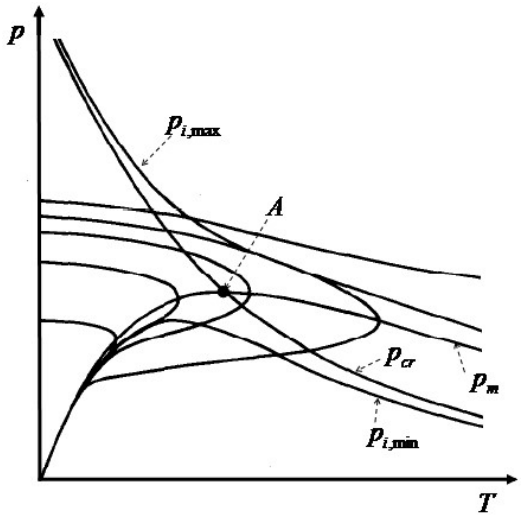

Figure 2.20: p-T phase plane, showing p-T trajectories, maxima curve p_{m}, loci of inflection points ($p_{\mathrm{i,max}}$ and $p_{\mathrm{i,min}}$) and the simplified curve p_{cr}

Apart from these different hypotheses, Eqs. 2.10 and 2.11 presented by Van Welsernaere and Froment can be considered perfectly equivalent to the classical PFR balance equations when the conversion is replaced by the partial pressure p of the reactant in the gas phase and n is limited to 1.

With the implementation of a Runge-Kutta method for the numerical integration of the system describing the reactor, they observed that a pronounced sensitivity of the T vs. z profile, in terms of temperature maxima, existed. Therefore, dividing Eq. 2.11 by 2.10, they obtained a single equation that expresses the dependence of the temperature with respect to the partial pressure: that is, a trajectory in the partial pressure vs. temperature plane (see Fig.2.20).

$$\frac{dT}{dp} = \frac{B}{A} + \frac{C}{A} \cdot \frac{T - T_w}{p \cdot exp\left(-\frac{a}{T} + b\right)} \tag{2.14}$$

Modifying the values of the wall temperature in a certain range, van Welsenaere and Froment noticed that the locus of the partial pressures in correspondence of the temperature maxima defined a curve (p_m) which showed a clear maximum (point A in Fig. 2.20). The analytical expression of such a curve is easily calculable and it can be used to find the critical values of the

maximum temperature and pressure for each wall temperature involved.

$$p_m = \frac{T - T_w}{\frac{B}{C} \cdot exp\left(-\frac{a}{T_m} + b\right)} \tag{2.15}$$

Van Welsenaere and Froment concluded that the conditions in correspondence of the maximum of the p_m vs. T_m curve are considered critical from the safety point of view and can be employed to identify the runaway boundary. It is worth noticing that this criterion is based on an intrinsic property of the system.

Secondarily, van Welsenaere and Froment aimed their work on the reactor behavior in the T vs z plane and they concluded that the hot-spot became more and more important (in terms of magnitude) as the inflection points occurred before the temperature maximum. Such an observation is also based on the conclusions of previous works such as those of Thomas [35] and Dente [28]. Differentiating Eq. 2.11 with respect to z and equating it to zero, it is possible to obtain an equation, which is a function of T and p, expressing the locus of the inflection points in the T vs. z plane. Particularly, investigating the sign of such an equation, it is possible to define two limit curves, called $p_{i,min}$ and $p_{i,max}$, that bound the region of the T vs. z curve where its concavity is downwards (see Fig. 2.20). Whenever an intersection in between a $p - T$ trajectory and $p_{i,min}$ or $p_{i,max}$ occurs, an inflection point is detected. It is found that the intersection of the $p - T$ trajectories with pi,max always occurs after the intersection with the pm-curve and therefore, corresponds to an inflexion point beyond the maximum in the T vs z curve. Conversely, not all the $p-$T trajectories have an intersection with$p_{i,min}$: that is, some T vs. z curves do not have inflexion points before their maximum. As a tentative approximation, van Welsenaere and Froment postulated that to avoid inflection points before the maximum of the T vs z curve, and therefore runaway, the $p - T$ trajectory representing the chosen conditions should not intersect the $p_{i,min}$ curve. But such a condition is too conservative. Following the Thomas' approach [35], they tried to superimpose that the two inflection points were coincident and occurred before the maximum. Although their mathematical approach was not completely exact (they referred to as a simplified treatment), they succeed in describing a critical curve, called p_{cr}, which has been reported in Fig. 2.20. In the end, the second criterion of van Welsenaere and Froment can be summarized as follows: runaway occurs whenever a $p - T$

trajectory intersects the p_{cr} curve. The critical trajectory that defines the runaway boundary is that one tangent to the p_{cr} curve.

These two runaway criteria are considered equivalent since they substantially predict the same critical trajectory in the $p - T$ plane.

During the remaining years of the '70s, no significant improvements regarding the definition of new runaway criteria for PFRs were documented. Anyway, it is worth to notice that some works concerning the coolant flow direction in a PFR were published. In 1972, Luss and Medellin [30] observed that the sensitivity behavior of a PFR with counter-current external cooling was quite different from that one described for parallel current external cooling. The situation was further complicated by the possible existence of multiple steady states, which had not been observed previously for constant and co-current external cooling.

Years later, in 1979, Degnan and Wei [26] noticed that the counter-current operating mode of a PFR led to greater possibilities of runaway triggering with respect to the co-current one, since near the reactor inlet the temperature difference between the internal reacting mixture and the external coolant generally reached a minimum, while the reaction and the heat generation rates were at their maximum. This condition highly impacts the first part of the reactor, potentially enhancing the reaction velocity. Anyway,no new runaway criterion was proposed.

2.2.2 New models in the '80s

During the early '80s, many efforts have been done with the target of finding generalized approaches for the detection of runaway boundaries in all the chemical reactors used in process industry. In order to achieve such a goal, it was necessary to deeply study all the aspects related to both the thermal behavior of the different reactors and the relative parametric sensitivity with respect to the variation of a number of operating parameters (that is, refining the mathematical modelling of such systems), together with the eventual steady-state multiplicity conditions.

Particularly, in 1981, Soria Lopez and his co-workers [33] published a work on the parametric sensitivity of a fixed bed catalytic reactor (PFR) analyzing the influence of the thermal gradients along the direction of the coolant flow. In order to describe the system, they solved classical PFR balance equations but they replaced the concentration by the partial pressure of the gaseous reactant, as it has been previously done by van Welsenaere and

Froment [36] (see Eq. 2.10 and Eq. 2.11). At that time, most of the runaway criteria discussed for PFRs were based on geometric properties exhibited by the temperature vs. conversion trajectory (reactant conversion was used as independent variable instead of the axial coordinate) corresponding to the solution of the equation resulting by dividing thermal balance equation by mass balance equation [21],[36]. It is peculiar that the solution of such an equation always predicts the occurrence of a maximum in the reactor temperature profile (that is, the so-called hot-spot always appears). For the batch reactors this was a safe approach because, as time passes, conversion unavoidably increases from 0 to 1: in the typical case where the coolant temperature does not exceed the initial temperature, a temperature maximum must be always reached. But, in tubular reactors, the finite length of the reactor can limit conversion: as a matter of fact, when taking the axial coordinate as the independent variable, we may have the situation where no maximum occurs in the temperature profile. Soria Lopez and his co-workers defined such a situation as Pseudo-Adiabatic Operation (PAO), since the global heat transfer coefficient U was not equal to zero (therefore, we are not in real adiabatic conditions) but, contextually, the reactor approached a maximum when $z \to \infty$ (of course such a maximum can correspond to runaway conditions). In other situations, Soria Lopez et al. observed that a Maximum occurred at a Finite Axial Reactor Position and they referred to it as (MFARP). PAO and MFARP operations are two different thermal responses of a PFR under different operative conditions and their behavior in the meaning of sensitivity had to be deeply analyzed in order to establish a congruous runaway criterion.

Indeed, the criterion developed by Soria Lopez et al. can be interpreted as an extension of the first runaway criterion proposed by van Welsenaere and Froment: basically, Eq. 2.15 for the partial pressure in correspondence of the temperature maximum along the reactor axis (considering the possibility of the occurrence of the PAO region) is changed in:

$$p_m = \frac{T_m - T_{cool}(T_m)}{\frac{B}{C} \cdot exp\left(-\frac{a}{T_m} + b\right)} \tag{2.16}$$

where the coolant temperature $T_{cool}(T_m)$ is that one in correspondence of the maximum temperature T_m. Imposing the derivative of such an equation with respect to the temperature equal to zero, the maximum of the pm curve can

be evaluated: that is, runaway boundary can be identified. Moreover, Soria Lopez proposed some algebraic simplification in order to easily calculate the maximum of the p_m curve that led to a numerical error minor than 4% in the estimation of the critical conditions.

In 1982, Morbidelli and Varma published the first of a series of studies concerning the concept of parametric sensitivity in chemical reactors as an intrinsic criterion to describe runaway boundaries. In this preliminary study, they analyzed the parametric sensitivity of a PFR in order to establish the critical values of the dimensionless adiabatic temperature rise (B) and Stanton number (St) defining both runaway and stable operations for all positive-order exothermic reactions with finite activation energies, and reactor inlet temperatures.

In 1985, Morbidelli and Varma published a new work that defined the runaway boundary using a generalized criterion based on the normalized parametric sensitivity of the reactor temperature maximum θ^* (that is, the so-called *objective function*) with respect to any system parameter Φ [32].

The local sensitivity of the dependent variableθ^*, with respect to the input parameter Φ, is defined as the first derivative of the dependent variable with respect to the input parameter:

$$s(\theta^*, \Psi) = \frac{\partial \theta^*(\Psi)}{\partial \Psi} = \lim_{\Delta\Psi \to 0} \frac{\theta^*(\Psi + \Delta\Psi) - \theta^*(\Psi)}{\Delta\Psi} \tag{2.17}$$

Even if higher-order derivatives can be calculated, the treatment to first-order ones is preferred because most applications are based on linear sensitivity analysis. Related to local sensitivity, the normalized sensitivity is defined as:

$$S(\theta^*, \Psi) = \frac{\psi}{\theta^*} \frac{\partial \theta^*(\Psi)}{\partial \Psi} = \frac{\Psi}{\theta^*} s(\theta^*, \Psi) \tag{2.18}$$

The original paper developed the criterion referring to batch and plug flow reactors but an extension to CSTRs would be published in the following year [25]. Notably, Morbidelli and Varma showed that the critical Semenov number, Ψ_{cr}, defined as the value where $S(\theta^*, \Phi)$ is maximum, is the same for any possible choice of the system parameters Ψ. This indicates that when the system enters into the parametrically sensitive region, it becomes simultaneously sensitive to all the parameters that affect its behavior [37]. This fact gives great generality to the definition of the parametrically sensitive region, which may then be taken as the boundary between runaway and safe system behavior.

It is worth noting that the sign of the normalized objective sensitivity $S(\theta^*, \Phi)$ can be either positive or negative and, such a sign, has a specific meaning: a positive (negative) value indicates that the temperature maximum increases (decreases) as the magnitude of the parameter with respect to the sensitivity is calculated increases. Thus, if the sensitivity is positive, the transition from non-runaway to runaway behavior occurs as this parameter is increased, while if the sensitivity is negative, the same transition occurs when the corresponding parameter is decreased [37]. Therefore, in order to develop a general definition for the detection of the runaway boundary, it is convenient to refer to the absolute value of the maximum of the normalized sensitivity function.

Past the half of the '80s, in 1986, Henning and Perez [29] proposed an intrinsic criterion for PFRs based on the behavior of local sensitivity of reactor temperature (T) to the inlet temperature, T_{in}, as a function of the axial coordinate l:

$$\frac{dS(T, T_{in})}{dl} = \frac{d}{dl}\left(\frac{dT}{dT_{in}}\right) \tag{2.19}$$

With the inlet condition:

$$S(T, T_{in}) = 1 \tag{2.20}$$

The Henning and Perez criterion defined the critical condition as the first occurrence of a minimum on the$S(T, T_{in}) - l$ curve before the temperature maximum on the $T - l$ trajectory (see Figure 2.21). In order to interpret this criterion, it is important to refer to both the thermal balance equation for PFR and the $S(T, T_{in}) - l$ critical curve. The first term of the thermal balance equation corresponds to the heat power generated inside the reactor while the second one is the heat power removed by the cooling system. From the inlet up to the minimum point, the $S(T, T_{in}) - l$ critical trajectory decreases monotonically; this means that the first derivative with respect to inlet temperature for the heat transferred is greater than that for the heat produced. At the minimum point, these derivatives are equal and beyond it they have an opposite behavior. Namely, beyond the minimum, the limiting curve presents a zone where the sensitivity with respect to variations of T_{in} for the heat generated is greater than that for the heat transfer: that is, critical conditions arise.

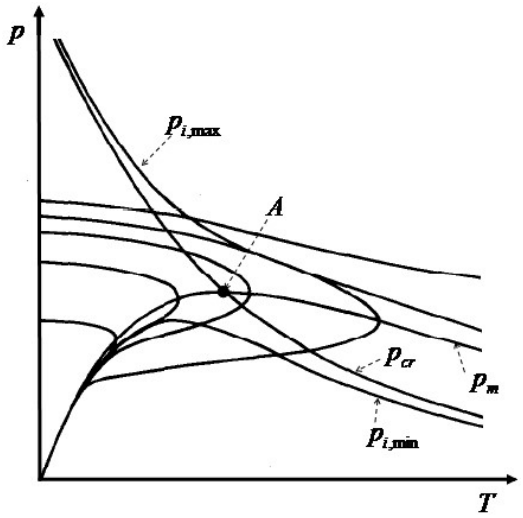

Figure 2.21: $S(T, T_{\text{in}})$ as a function of the axial coordinate l for different values of the ratio of reactant to coolant heat capacity for a PFR (τ_{PFR}).[29]

2.2.3 Recent works

In 1998, Wu et al. [38] studied the influence of the occurrence of the PAO region on the determination of the runaway boundaries using the generalized parametric sensitivity (objective function: temperature maximum, θ^*) but using two different models for its calculation: the first was focused on solving the dimensionless form of mass and energy balance equations, that means employing the so-called z-MV criterion; the second by solving their ratio, that is referring the so-called x-MV criterion.

It is interesting to underline that when the reactor operates in the PAO region, the z-MV criterion is able to determine that the reactor is too short for developing a local temperature maximum (the temperature-axial coordinate profile is a monotonically increasing function) and, therefore, it automatically selects the temperature value at the reactor outlet asθ^* in the sensitivity calculation (because it is the maximum along z). On the contrary, when the conversion is taken as the independent variable, the PFR model becomes identical to the BR model. Therefore, we are considering the possibility of complete conversion, which can only be achieved in reactors of infinite length. It follows that the x-MV criterion does not account for the occurrence of the PAO region, thus providing runaway boundaries that are always more conservative compared to those predicted by the z-MV criterion [37].

In 1999, another sort of revolution occurred: the group of Zaldivar and his co-workers developed the so-called divergence criterion for the detection of the runaway boundaries in BRs [34] and, in 2003, they extended it to whatever type of reactor [39]. Starting from the assumption that the dynamics of a reacting system can be always represented by a system of ordinary differential equations (ODEs), that suitably describes material and energy balances in the general form:

$$\frac{dx_i}{dt} = F_i[\bar{x}(t)] \tag{2.21}$$

They showed that each state of the reacting system corresponded to a unique point onto the state space, which is called state point, and the system state time evolution was represented as a motion along a trajectory. According to the Liouville's theorem [39], there is a relation between the state space volume of a N-dimensional dynamical system and its divergence. This relation can be expressed as:

$$V(t) = V(0) \cdot exp\left[\int_0^t div\{F_i[\bar{x}(t)]\}dt\right] \tag{2.22}$$

Where:

$$div\{F_i[\bar{x}(t)]\} = \sum_{i=1}^{N} \frac{\partial F_i[\bar{x}(t)]}{\partial x_i} \tag{2.23}$$

Hence, for a dynamical system, the rate of change of an infinitesimal volume $V(t)$, following an orbit $\bar{x}(t)$, is given by the divergence of the flow, which is locally equivalent to the trace of the $F_i[\bar{x}(t)]$ Jacobian. Even if for dissipative systems, as chemical reactors are, the divergence unavoidably decreases as time approaches ∞, it has been observed in [34] that when the system is operated under potentially runaway conditions it exhibits, over a certain period of time, a state space volume expansion. This means that trajectories originating from nearby starting points will diverge and such a feature can be correlated with the parametric sensitivity of the reactor temperature with respect to the system constitutive parameters or initial conditions. Therefore, taking into account such a correlation between parametric sensitivity and the divergence of nearby trajectories, Strozzi et al. defined a general criterion for runaway detection. Notably, a reactor is operating under runaway conditions when the divergence of the ODEs system describing its thermal behavior becomes positive on a section of the reaction path.

$$div\{F_i[\bar{x}(t)]\} > 0 \tag{2.24}$$

This criterion is so general that it can be easily applied to both controlled (there are suitable equations expressing temperature control strategy, e.g. isothermal) and uncontrolled (typically, when the reactor operates in the isoperibolic temperature control mode, coolant temperature is assumed to be constant for all process duration) systems independently on the reactor type (CSTR, PFR, BR, SBR).

Nevertheless, such a general criterion needs to be subjected to a single constraint in order to be in accordance with both theoretical and experimental evidence on runaway detection. This constraint implies a fast reaction that does not produce directly heat [39]. For describing the kinetics of the reacting systems of interest, usually the minimum number of global reactions (NR) is utilized; therefore, thanks to the stoichiometric constraint, the NC number of moles of each species can be computed from the NR extent-of-reactions, which are easily related to the conversion of some reactants or intermediates. Hence, the NC material balances can be recast in NR balance equations for the NR extent-of-reactions, one of these being that of the fast reaction that does not produce or consume heat. In particular, such an extent-of-reaction can generate a strong volume contraction (synthesized in a non-runaway condition according to the divergence criterion) in the N-dimensional state space arising by considering that extent-of-reaction in the divergence computation, but a global expansion (runaway) in the (N-1)-dimensional space arising by not considering that extent-of-reaction into the divergence computation. Therefore, as a general constraint for the runaway criterion based on divergence, all contributions arising from extent-of-reactions that are not related to heat evolutions must be disregarded into the divergence calculation. This assumption is necessary in order to avoid evaluation errors due to the presence of strongly negative terms (the divergence is a sum with sign) that are not related to the runaway phenomenon.

Apart from this expedient, the divergence criterion can be acknowledged as the actual maximum powerful tool capable of detecting explicitly the runaway boundaries for whatever type of chemical reactor and reaction path. As well as the sensitivity parametric criterion, it is one of the most used nowadays, whereas the other methods here described are interesting mainly from a historical point of view and are rarely employed in current applications.

Method of lines

The method of lines (MOL) is a numerical method dedicated to solving time and space dependent PDEs. Schiesser W. E. [52] published one of the first books about this topic, and he made a lot of efforts to develop and popularize the MOL. Its stability and application for effectively solving different types of PDEs has been deeply studied in the past,[49],[50],[56]. There are also a lot of dedicated works aimed to effectively apply it inside computer codes, such as $MATLAB^{\text{TM}}$, due to its extremely intuitive structure [53] [54] [55]. It found recent applications in solving the heat equation in multidimensional domains [44], and in 1-D chemical reactive systems [48]. Still today it is finding new research interests, with the extension of the method to fractional derivatives [51].

The main idea behind it is to transform PDEs into ODEs. This is accomplished by discretizing the spatial derivative operator. Thus, the final problem appears as an ODEs system, since the spatial derivatives have been transformed into algebraic formulas, which structure depends on the type of discretization chosen. Finally, a proper time integrator needs to be chosen in order to obtain the final result. The following diagram shows the generic algorithm to implement the MOL.

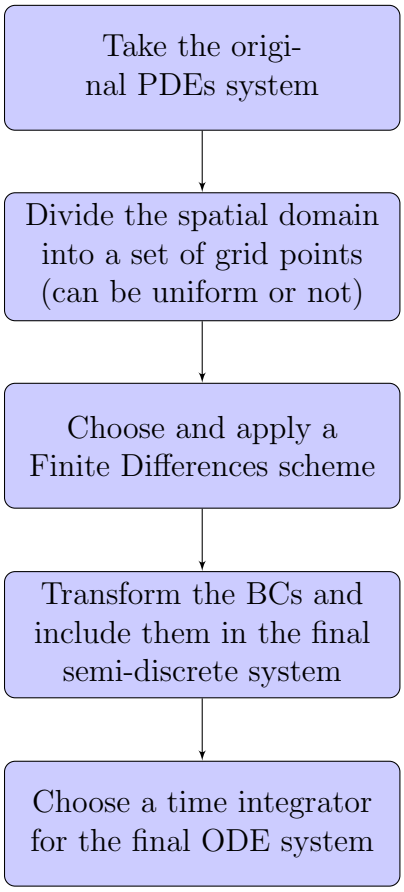

3.1 PDEs structure

The PDEs structure depends upon the specific problem. Although,without loss of generality for the purposes of this work, we will take as an example the simple 1-D diffusion equation:

$$u_t = Du_{xx}, \qquad x \in (0,1) \tag{3.1}$$

Where u_t is the subscript notation for $\frac{\partial u(x,t)}{\partial t}$, and for $k-th$ order derivatives the dependent variable is repeated k times, such as $u_{xx} = \frac{\partial u(x,t)}{\partial^2 x}$. D is a generic positive constant.In this section, $u$is considered a single independent variable, but the whole discussion can be extended to $\bar{u}$ as a vector of several independent variables, resulting in system of PDEs. This equation, despite

his simplicity, is able to characterize both the heat equation and the Fick's law, namely the basis for all the equations that will be analyed through this work. The equation 3.1 must be supplemented with two BCs and one IC. We consider as initial condition:

$$u_{t=0} = u_{t_0} \tag{3.2}$$

And as BCs:

$$u_{x=0} = a, \qquad a \in \mathbb{R} \tag{3.3}$$

$$\left.\frac{\partial u}{\partial x}\right|_{x=1} = 0 \tag{3.4}$$

The left term is a Dirichelet condition, while the right one is a Neumann condition. From now on, we will consider this example in order to discuss the implementation fo the MOL.

3.2 Generation of the spatial grid

Now that the equation to solve is defined, it is possible to approach his numerical solution. The general idea behind this is the following: instead of trying to know the solution over the continuous domains of space and time, we decide at first to estimate the spatial derivatives in a finite subset of $n+1$ nodes, distributed over the original domain (in this case the set $[0,1]$). In this way, the continuous spatial derivative operator $\frac{\partial u(x,t)}{\partial x}$ is approximated by using the piecewise linear function that takes the value u_i in x_i for $i = 0, 1..., n$(Note: while the grid nodes are numbered from 1 to $n+1$, corresponding to n intervals, the subscripts of the related elements are numbered from 0 to n). The resulting grid of the points that discretized the original domain $[0,1]$ is also referred to as a *mesh*, despite it is a term that often refers to multidimensional domains. For 1-D domains, where the points are naturally ordered, we can classify the type of grids under the following groups:

- Arbitrary grids
- Adaptive grids

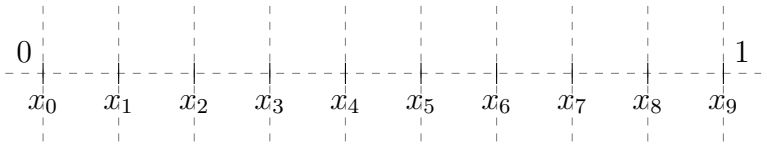

Figure 3.1: Example of uniform grid with 10 nodes

An arbitrary grid is a grid chosen a priori, and it remains exactly the same for the whole computation. An adaptive grid is a grid that changes his structure during the resolution of the associated problem. The idea of adaptive grids is the local refinement. As an example, consider a simple function $f : \mathbb{R} \to \mathbb{R}$. If the solution exhibits a sharp increase at some point, the spatial operator approximation will be less accurate. Thus, an adaptive grid algorithm will provide a local refinement of the original mesh around the points where the approximation is less accurate. It could be possible to solve preemptively such issue by taking an extremely fine uniform grid. Though, this approach is not optimal, since bigger grids lead to bigger discretizied problems (the dimension of the final ODE system is up to $(n+1)$, and each equation contains discretization matrices with size up to $(n+1)^2$), leading to extremely high computational times. Also, this procedure is unefficient because it wastes a lot of computational time over parts of the domain where the solution is smooth (and hence, no fine grids are required). This leads the introduction of non-uniform grids and adaptive ones. For the purposes of this work, since adaptive grids have not been yet applied to such problems, we will discuss uniform and non-uniform arbitrary grids.

Uniform grids (1-D)

A uniform grid is a grid over a domain where the distance between each point is constant. Considering the domain $D : [0, 1]$, we will have $n+1$ nodes, with the distance between two points equal to $h = \frac{1}{n}$. Fig. 3.1 shows an example of a uniform grid.

Non-uniform grids (1-D)

A non-uniform grid, as the name suggests, is a grid made of nodes with any disposition. In this case the distance between two point is not a constant

anymore, and we will refer to it as

$$h_i = x_i - x_{i-1} \qquad i = 1, ...n \tag{3.5}$$

The number of points in the grids is always $n + 1$.

The most convenient way to localize such nodes is to introduce a function $F(\tilde{x}_i) : D \to D$, where $\tilde{x}_i$ is the respective uniform grid over the domain, made of $n + 1$ nodes. $F(\tilde{x}_i)$ should respect some rule in order to describe efficiently the non-uniform grid:

- $F(\tilde{x}_i)$ is monotonically increasing
- $F(\tilde{x}_i)$ is bijective

As an example, we show how the grid changes if we consider the non-uniform grid generated by $F(\tilde{x}_i) = x^2$. The function is consistent in the domain. Fig. 3.2 compares the uniform grid with the non-uniform one. It is noticeable how the grid generated by the function is more refined in the first half of the domain, and more sparse in the other. The choice of an arbitrary non-uniform grid allows the user to highly increase the resolutive algorithm performance, enhancing the precision of the spatial operator approximation. The important element in the choice of the function $F(\tilde{x}_i)$ for an arbitrary grid is the generation of a mesh that results refined where it is needed (thus, where the solution exhibits a sharp behavior). This intrinsically requires to predict how the solution of the PDEs evolves. While in general this is not a given fact, we will see that for the specific problems analysed, it is actually well known how the solution behaves (and it will be discussed later). Now that the discretization of the domain has been defined, the next step consists in providing a suitable discretization for the spatial derivatives.

3.3 Discretization of the spatial derivates

Once that the domain has been divided in nodes, it is necessary to express continuum operators, like derivatives, as functions of node values. Finite Differences (FD), approximate derivatives as linear functions of the node values. We will call $\frac{d^k f}{dx^k}$ the $k - th$ order derivative of a generic function f (derivable at least $k + 1$ times) with respect of the space x (we will keep the dissertation on 1-D domains, but it can be extended to multi-dimensional domains).

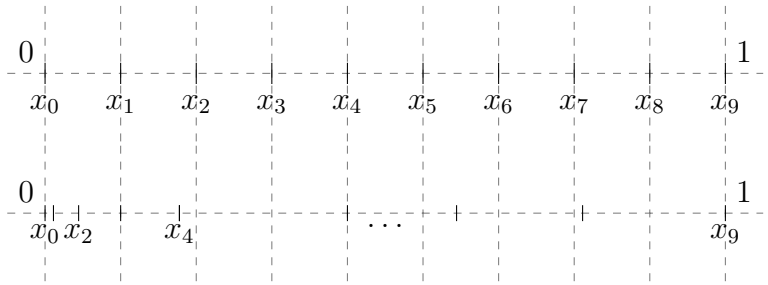

Figure 3.2: Comparison between a uniform grid and a non-uniform one, generated by $F(\tilde{x}_i) = x^2$

3.3.1 Uniform grids

On a uniform grid, the most simple FD scheme for the derivatives of f on the grid point x_i can be deduced by writing the Taylor series expansions of f in the proximity points x_{i+1} and x_{i-1}, centered on the mid point x_i:

$$f_{i+1} = f_i + \frac{h}{1!}\left.\frac{df}{dx}\right|_{x_i} + \frac{h^2}{2!}\left.\frac{d^2f}{dx^2}\right|_{x_i} + \frac{h^3}{3!}\left.\frac{d^3f}{dx^3}\right|_{x_i} + \frac{h^4}{4!}\left.\frac{d^4f}{dx^4}\right|_{x_i} + ... \tag{3.6}$$

$$f_{i-1} = f_i - \frac{h}{1!}\left.\frac{df}{dx}\right|_{x_i} + \frac{h^2}{2!}\left.\frac{d^2f}{dx^2}\right|_{x_i} - \frac{h^3}{3!}\left.\frac{d^3f}{dx^3}\right|_{x_i} + \frac{h^4}{4!}\left.\frac{d^4f}{dx^4}\right|_{x_i} + ... \tag{3.7}$$

Substracting Eq. 3.6 from Eq. 3.7 we get:

$$f_{i+1} - f_{i-1} = 2\frac{h}{1!}\left.\frac{df}{dx}\right|_{x_i} + 2\frac{h^3}{3!}\left.\frac{d^3f}{dx^3}\right|_{x_i} + ... \tag{3.8}$$

$$\left.\frac{df}{dx}\right|_{x_i} = \frac{f_{i+1} - f_{i-1}}{2h} - \frac{h^2}{3!}\left.\frac{d^3f}{dx^3}\right|_{x_i} + ... \tag{3.9}$$

If $h \to \infty$:

$$\left.\frac{df}{dx}\right|_{x_i} = \frac{f_{i+1} - f_{i-1}}{2h} + \mathcal{O}(h^2) \tag{3.10}$$

The formula presented in Eq. 3.10 is the *centered FD* scheme, because the estimated function is "central" respect to the grid points required in the stencil. This formula offers an approximation proportional to h^2, since the higher order elements are negligible as $h \to \infty$. Different approximations can

be deduced from Taylor expansions. From Eq. 3.6 we cab obtain:

$$\left.\frac{df}{dx}\right|_{x_i} = \frac{f_{i+1} - f_i}{h} + \frac{h}{2!}\left.\frac{d^2 f}{dx^2}\right|_{x_i} + ... = \frac{f_{i+1} - f_i}{h} + \mathcal{O}(h) \tag{3.11}$$

And from Eq. 3.7:

$$\left.\frac{df}{dx}\right|_{x_i} = \frac{f_i - f_{i-1}}{h} + \frac{h}{2!}\left.\frac{d^2 f}{dx^2}\right|_{x_i} + ... = \frac{f_i - f_{i-1}}{h} + \mathcal{O}(h) \tag{3.12}$$

Equation 3.11 is called *upwind scheme*, Eq. 3.3.1 is called *downwind scheme* instead. Those formulas are non centered, and they have an important physical interpretation: they represent the "flow of information". Fluid dynamics equations are almost always coupled with a fluid that moves with a certain velocity $\mathbf{v}$. Upwind and downwind schemes reflect that fact that a quantity can be transported in the same fluid direction, or in countercurrent. Thus, these two latter schemes find a lot of applications in numerical methods for solving fluid dynamic equations. It is noticeable that they also are less accurate than the centered scheme ($\mathcal{O}(h)$ vs $\mathcal{O}(h^2)$).

Of course it is possible to generate different schemes, by considering additional function approximations based always on Taylor expansions, leading to more complex stencils. This is an example of a fourth-order biased-upwind for the first derivative:

$$\left.\frac{df}{dx}\right|_{x_i} = \frac{-f_{i-3} + 6f_{i-2} - 18f_{i-1} + 10f_i + 3f_{i+1}}{12h} + \mathcal{O}(h^4) \tag{3.13}$$

Second order derivatives A scheme for the second order derivative can be generating by summing Eq. 3.6 and Eq. 3.7:

$$f_{i+1} + f_{i-1} = 2f_i + 2\frac{h^2}{2!}\left.\frac{d^2 f}{dx^2}\right|_{x_i} + 2\frac{h^4}{4!}\left.\frac{d^4 f}{dx^4}\right|_{x_i} \tag{3.14}$$

$$\left.\frac{d^2 f}{dx^2}\right|_{x_i} = \frac{f_{i+1} - 2f_i + f_{i-1}}{h^2} + \mathcal{O}(h^2) \tag{3.15}$$

That is the classical second order centered scheme for the second derivative.

3.3.2 Accuracy and order

We introduced FD schemes related to different orders of approximations: those are generally obtained by considering stencils involving more grid points to estimate the derivative operator. The order of approximation represents the error in the solution due to the discrete scheme involved. The error is always reduced by decreasing the step h, until it reaches a status where the solution does not change by further decreasing h. This is called *grid independence*. As an example, for a first order scheme, if the grid spacing is halved the error is halved, for a second order scheme the error would reduce by a factor of four. Anyway, while high order stencils seem more appealing, due to their increased accuracy, it should not be forgotten that they also generate less sparse matrices, leading to higher computational costs and memory usage. It is important to select an adequate order of approximation for each specific problem. In general, some practical guideline can be proposed[55]:

- First-order spatial derivatives (representing advection or convection) are usually best approximated using upwind FD schemes (since they represent the transport phenomenon)
- Second-order derivatives (representing diffusion or dispersion) are usually best approximated using centered FD schemes (according to *Fick's law* and *Fourier's law*, diffusion has no preferential direction).

It is also important to notice that the ODE generated by the implementation of FD schemes must be still time integrated, leading to additional time-discretization issues.

3.3.3 Non-uniform grid

The stencils generated on uniform grids can be extended to arbitrarily spaced ones. In this case, instead of a constant h, we have the irregular steps h_i (see Eq. 3.5). For the first derivative, we still get the Taylor polynomials at x_i:

$$f_{i+1} = f_i + \frac{h_i}{1!}\left.\frac{df}{dx}\right|_{x_i} + \frac{h_i^2}{2!}\left.\frac{d^2f}{dx^2}\right|_{x_i} + \frac{h_i^3}{3!}\left.\frac{d^3f}{dx^3}\right|_{x_i} + \frac{h_i^4}{4!}\left.\frac{d^4f}{dx^4}\right|_{x_i} + ... \tag{3.16}$$

$$f_{i-1} = f_i - \frac{h_{i-1}}{1!}\left.\frac{df}{dx}\right|_{x_i} + \frac{h_{i-1}^2}{2!}\left.\frac{d^2f}{dx^2}\right|_{x_i} - \frac{h_{i-1}^3}{3!}\left.\frac{d^3f}{dx^3}\right|_{x_i} + \frac{h_{i-1}^4}{4!}\left.\frac{d^4f}{dx^4}\right|_{x_i} + ... \tag{3.17}$$

We get then by subtraction:

$$f_{i+1} - f_{i-1} = (h_i + h_{h-1}) \left.\frac{df}{dx}\right|_{x_i} + \frac{(h_i^2 - h_{h-1}^2)}{2!} \left.\frac{d^2 f}{dx^2}\right|_{x_i} + \frac{(h_i^3 - h_{h-1}^3)}{3!} \left.\frac{d^3 f}{dx^3}\right|_{x_i} + ... \tag{3.18}$$

$$\left.\frac{df}{dx}\right|_{x_i} = \frac{f_{i+1} - f_{i-1}}{h_i + h_{h-1}} + (h_i - h_{h-1}) + ... \tag{3.19}$$

$$\tag{3.20}$$

Note that in this case the scheme is only first order accurate.

3.3.4 General algorithm

It would be interesting having an approach to generate a stencil of each order of accuracy and derivative, given an arbitrary spaced grid. A lot of studies have been done in this way, with the aim of generating a general algorithm. The main idea is to define the number of points required by the stencil, and then evaluate the discretization coefficients (called *weights*). Studies have been done in order to generate these algorithms and implement them in computer codes [40] [45] [46], but they were often limited to low order derivatives or applicable on uniform grids only. Fornberg developed a compact formula for generating FD schemes for every order of derivative and accuracy, on arbitrarily spaced 1-D grids [41], [42]. The algorithm requires as input data:

- The location x_i where the derivatives should be estimated
- Grid point locations x_0, x_1...., that can be positioned arbitrarily
- Stencil width
- Highest derivative m needed

The algorithm gives as output the coefficients required to approximate all the derivatives from 0 to $m - th$ order:

$$\left.\frac{d^k f}{dx^k}\right|_{x=x_i} \simeq \sum_{i=0}^{n} c_i^k f(x_i) \qquad k = 0, 1...m \tag{3.21}$$

As an example, Table 3.1 gives the coefficients for a centered 9-point stencils for first, second, thrid and fourth order derivatives, until 8-th order accuracy, on a uniform grid. Table 3.2 gives the same results with an upwind stencil.

This algorthm is extremely powerful, since it allows to simply implement in a computer code, such as $MATLAB^{\mathrm{TM}}$and $SCILAB$, a tool to estimate FD schemes for every stencil, 1-D grid, order and accuracy.

Algorithm derivation [42] Let us consider again a generic funcion $f(x)$, derivable at least $k+1$ times, on the grid $x_0, x_1...x_n$. The Lagrange interpolation polynomial bases on $j+1$ function values is then:

$$p_j(x) = \sum_{i=o}^{j} L_{i,j}(x) f_i \qquad j = 0, 1...n \tag{3.22}$$

Where

$$L_{i,j}(x) = \frac{(x-x_0)...(x-x_{n-1})(x-x_{n+1})...(x-x_j)}{(x_n-x_0)...(x_n-x_{n-1})(x_n-x_{n+1})...(x_n-x_j)} \tag{3.23}$$

Let us assume to approximate the derivatives at the position x=0:

$$\left.\frac{d^k f(x)}{dx^k}\right|_{x=0} \simeq \left.\frac{d^k p_j(x)}{dx^k}\right|_{x=0} = \sum_{i=o}^{j} \left.\frac{d^k L_{i,j}(x)}{dx^k}\right|_{x=0} \cdot u_i = \sum_{i=o}^{j} c_{i,j}^k \cdot u_i \tag{3.24}$$

The subscript j in the coefficient $c_{i,j}^k$ indicates the stencil width. Applying Taylor formula we get then:

$$L_{i,j}(x) = \sum_{i=o}^{j} \left.\frac{d^k L_{i,j}(x)}{dx^k}\right|_{x=0} \cdot \frac{x^k}{k!} = \sum_{i=o}^{j} c_{i,j}^k \cdot \frac{x^k}{k!} \tag{3.25}$$

From Eq.3.23 we get the recursion relations (which are different if $i = j$):

$$L_{i,j}(x) = \frac{x - x_j}{x_i - x_j} L_{i,j-1}(x) \tag{3.26}$$

$$L_{j,j}(x) = \left[\frac{\prod_{\nu=0}^{j-2}(x_{j-1} - x_\nu)}{\prod_{\nu=0}^{j-1}(x_j - x_\nu)}\right](x - x_{j-1}) L_{j-1,j-1}(x) \tag{3.27}$$

n	$\mathcal{O}$	x_{i-4}	x_{i-3}	x_{i-2}	x_{i-1}	x_i	x_{i+1}	x_{i+2}	x_{i+3}	x_{i+4}
1	2				$-\frac{1}{2}$	0	$\frac{1}{2}$			
	4			$\frac{1}{12}$	$-\frac{2}{3}$	0	$\frac{2}{3}$	$-\frac{1}{12}$		
	6		$-\frac{1}{60}$	$\frac{3}{20}$	$-\frac{3}{4}$	0	$\frac{3}{4}$	$-\frac{3}{20}$	$\frac{1}{60}$	
	8	$\frac{1}{280}$	$-\frac{4}{105}$	$\frac{1}{5}$	$-\frac{4}{5}$	0	$\frac{4}{5}$	$-\frac{1}{5}$	$\frac{4}{105}$	$-\frac{1}{280}$
2	2				1	-2	1			
	4			$-\frac{1}{12}$	$\frac{4}{3}$	$-\frac{5}{2}$	$\frac{4}{3}$	$-\frac{1}{12}$		
	6		$\frac{1}{90}$	$-\frac{3}{20}$	$\frac{3}{2}$	$-\frac{49}{18}$	$\frac{3}{2}$	$-\frac{3}{20}$	$\frac{1}{90}$	
	8	$-\frac{1}{560}$	$\frac{8}{315}$	$-\frac{1}{5}$	$\frac{8}{5}$	$-\frac{205}{72}$	$\frac{8}{5}$	$-\frac{1}{5}$	$\frac{8}{215}$	$-\frac{1}{560}$
3	2			$-\frac{1}{2}$	1	0	-1	$\frac{1}{2}$		
	4		$\frac{1}{8}$	-1	$\frac{13}{8}$	0	$-\frac{13}{8}$	1	$-\frac{1}{8}$	
	6	$-\frac{7}{240}$	$\frac{3}{10}$	$-\frac{169}{120}$	$\frac{61}{30}$	0	$-\frac{61}{30}$	$\frac{169}{120}$	$-\frac{3}{10}$	$\frac{7}{240}$
4	2			1	-4	6	-4	1		
	4		$-\frac{1}{6}$	2	$-\frac{13}{2}$	$\frac{28}{3}$	$-\frac{13}{2}$	2	$-\frac{1}{6}$	
	6	$\frac{7}{240}$	$-\frac{2}{5}$	$\frac{169}{60}$	$-\frac{122}{15}$	$\frac{91}{8}$	$-\frac{122}{15}$	$\frac{169}{60}$	$-\frac{2}{5}$	$\frac{7}{240}$

Table 3.1: List of weights for centered schemes in uniform grids (Source: Fornberg B., 1988)

n	$\mathcal{O}$	x_i	x_{i+1}	x_{i+2}	x_{i+3}	x_{i+4}	x_{i+5}	x_{i+6}
1	1	-1	1					
	2	$-\frac{3}{2}$	2	$-\frac{1}{2}$				
	3	$-\frac{11}{6}$	3	$-\frac{3}{2}$	$\frac{1}{3}$			
	4	$-\frac{25}{12}$	4	-3	$\frac{4}{3}$	$-\frac{1}{4}$		
2	1	1	-2	1				
	2	2	-5	4	-1			
	3	$\frac{35}{12}$	$-\frac{26}{3}$	$\frac{19}{2}$	$-\frac{14}{3}$	$\frac{11}{12}$		
	4	$\frac{15}{4}$	$-\frac{77}{6}$	$\frac{107}{6}$	-13	$\frac{61}{12}$	$-\frac{5}{6}$	
3	1	-1	3	-3	1			
	2	2	$-\frac{5}{2}$	9	-12	7	$-\frac{3}{2}$	
	3	$-\frac{17}{4}$	$\frac{71}{4}$	$-\frac{59}{2}$	$\frac{49}{2}$	$-\frac{41}{4}$	$\frac{7}{4}$	
4	1	1	-4	6	-4	1		
	2	3	-14	26	-24	11	-2	
	3	$\frac{35}{6}$	-31	$\frac{137}{2}$	$-\frac{242}{3}$	$\frac{107}{2}$	-19	$\frac{17}{6}$

Table 3.2: List of weights for upwind schemes in uniform grids (Source: Fornberg B., 1988)

By substitutions of relation in Eq. 3.25, we get recursion relations for the FD scheme weights:

$$c_{i,j}^{k} = \frac{1}{x_j - x_i}(x_j c_{i,j-1}^{k} - k c_{i,j-1}^{k-1}) \tag{3.28}$$

$$c_{j,j}^{k} = \left[\frac{\prod_{\nu=0}^{j-2}(x_{j-1} - x_\nu)}{\prod_{\nu=0}^{j-1}(x_j - x_\nu)}\right](k c_{j-1,j-1}^{k-1} - x_{j-1} c_{j-1,j-1}^{k}) \tag{3.29}$$

Starting from the trivial value $c_{0,0}^{0} = 1$, all the subsequent coefficients can be evaluated by applying these recursion formulas.

3.4 Translation of the boundary conditions

Until now, we just mentioned the boundary conditions of the problem, which actually arise for the characterization of the spatial derivative operator. The translation of the boundary conditions into the method of lines is a crucial step, as they are a very important aspect of the problem definition. Differentiation matrices do not take into account what actually happens at the boundary of the problem. It is then necessary to pass the information contained in the boundary conditions to the system, in order to have an ODE system that still describes coherently our original problem.

As a reminder, we report the main types of boundary conditions:

- Dirichlet conditions
- Neumann conditions
- Robin conditions

There are several strategies to include the BCs into the discretized problem, some of them consists in simple approximations which can be sometimes convenient, whereas others are more rigorous but they need a deeper analysis of the problem. According to our example, we have to implement a Dirichlet (eq. 3.3) and a Neumann condition (eq. 3.4).

3.4.1 Elimination of the unknown variables

The idea of this method is to include the boundary conditions directly into the discretized form of problem, with the introduction of a proper auxiliary

vector. Let's consider the basic discretized problem generated by a 3-point-centered scheme for the second derivative.

$$\begin{bmatrix} u_{1,t} \\ u_{2,t} \\ u_{3,t} \\ \vdots \\ \vdots \\ u_{n-1,t} \end{bmatrix} = \frac{1}{h^2} \begin{bmatrix} -2 & 1 & & & & \\ -1 & 2 & -1 & & & \\ & -1 & 2 & -1 & & \\ & & \ddots & \ddots & & \\ & & & \ddots & \ddots & \\ & & & -1 & 2 \end{bmatrix} \begin{bmatrix} u_1 \\ u_2 \\ u_3 \\ \vdots \\ \vdots \\ u_{n-1} \end{bmatrix} \tag{3.30}$$

Implementing Dirchelet BCs

In this case, the solution is straightforward. The approximated 3-point scheme at the grid node x_1 needs the function value u_0 in order to be computed. Such information, that is the value of the function u at the node x_0, it is given by the Dirichelet BC.

$$u_{1,t} = \frac{u_0 - 2 \cdot u_1 + u_2}{h^2} \tag{3.31}$$

And it is analytically implementable with the introduction of an auxiliary vector:

$$\begin{bmatrix} u_{1,t} \\ u_{2,t} \\ u_{3,t} \\ \vdots \\ \vdots \\ u_{n-1,t} \end{bmatrix} = \frac{1}{h^2} \begin{bmatrix} -2 & 1 & & & & \\ -1 & 2 & -1 & & & \\ & -1 & 2 & -1 & & \\ & & \ddots & \ddots & & \\ & & & \ddots & \ddots & \\ & & & -1 & 2 \end{bmatrix} \begin{bmatrix} u_1 \\ u_2 \\ u_3 \\ \vdots \\ \vdots \\ u_{n-1} \end{bmatrix} + \frac{1}{h^2} \begin{bmatrix} a \\ 0 \\ 0 \\ \vdots \\ \vdots \\ \vdots \end{bmatrix} \tag{3.32}$$

Implementing Neumann BCs

This method can be extended to more complex forms of BCs, such as Neumann conditions. In this case it is necessary to introduce eq. 3.4 in discretized form. It is important to notice that, in order to not lose accuracy in the final solution, the FD scheme selected for the eventual BCs should have an order of accuracy equal to the main discretized problem. In this example, a two-point scheme for the firts derivative is an adequate choice. For more accurate

discretization, non-centered schemes should be taken for the approximations of the BCs.

$$u_{n-1,t} = \left.\frac{\partial u}{\partial x}\right|_{x=n} \approx \frac{u_n - u_{n-1}}{h} = 0 \tag{3.33}$$

That means:

$$u_n = u_{n-1} \tag{3.34}$$

Now, as done above, the 3-point scheme can be extended at the node x_n with the relation for the function value u_n just found.

$$u_{n-1,t} \approx \frac{u_{n-2} - 2 \cdot u_{n-1} + u_n}{h^2} = \frac{u_{n-2} - 2 \cdot u_{n-1} + u_{n-1}}{h^2} = \frac{u_{n-2} - u_{n-1}}{h^2} \tag{3.35}$$

Hence, it is sufficient to modify the coefficient at the position n, nin the discretization matrix. The final system that takes in account all the BCs becomes then:

$$\begin{bmatrix} u_{1,t} \\ u_{2,t} \\ u_{3,t} \\ \vdots \\ \vdots \\ u_{n-1,t} \end{bmatrix} = \frac{1}{h^2} \begin{bmatrix} -2 & 1 & & & & \\ -1 & 2 & -1 & & & \\ & -1 & 2 & -1 & & \\ & & \ddots & \ddots & & \\ & & & \ddots & \ddots & \\ & & & -1 & 1 \end{bmatrix} \begin{bmatrix} u_1 \\ u_2 \\ u_3 \\ \vdots \\ \vdots \\ u_{n-1} \end{bmatrix} + \frac{1}{h^2} \begin{bmatrix} a \\ 0 \\ 0 \\ \vdots \\ \vdots \\ 0 \end{bmatrix} \tag{3.36}$$

One the biggest downsides of this technique is the need to compute the values of the function at the boundary, since the ODE system does not take them directly into account.

3.4.2 Introduction of fictious nodes

The idea of this methods is to introduce in the system the discretized form for the boundaries of the domain $u_{0,t}$ and $u_{n,t}$. This leads to the introduction of the fictious nodes x_{-1} and x_{n+1}, located outside the domain. It is then needed to elaborate these new, fictious terms. Also the new coefficients introduced in the discretization matrix (with a dimension now equal to $(n+1) \times (n+1)$) must be estimated.

Implementing Dirchelet BCs

Since the value of the function is fixed on the node x_0, here it is sufficient to write the relative raw in the equation system such that eq.3.3 is respected.

$$u_{0,t} \approx \frac{0 \cdot u_{n-1} - 0 \cdot u_0 + 0 \cdot u_1}{h^2} + a = a \tag{3.37}$$

This still requires the implementation of an auxiliary vector:

$$\begin{bmatrix} u_{0,t} \\ u_{1,t} \\ u_{2,t} \\ \vdots \\ \vdots \\ u_{n-1,t} \\ u_{n,t} \end{bmatrix} = \frac{1}{h^2} \begin{bmatrix} 0 & 0 & & & & & \\ -1 & 2 & -1 & & & & \\ & -1 & 2 & -1 & & & \\ & & \ddots & \ddots & & & \\ & & & \ddots & \ddots & \ddots & \\ & & & -1 & 2 & -1 & \\ & & & & \cdots & \cdots & \end{bmatrix} \begin{bmatrix} u_0 \\ u_1 \\ u_2 \\ \vdots \\ \vdots \\ u_{n-1} \\ u_n \end{bmatrix} + \begin{bmatrix} a \\ 0 \\ 0 \\ \vdots \\ \vdots \\ \vdots \\ 0 \end{bmatrix} \tag{3.38}$$

Implementing Neumann BCs

In this case, the term $u_{n,t}$ becomes:

$$u_{n,t} \approx \frac{u_{n-1} - 2u_n + u_{n+1}}{h^2} \tag{3.39}$$

The function value u_{n+1} can be still evaluated by using a FD scheme on the BC, such as a 2-point centered stencil.

$$u_{n,t} \approx \frac{u_{n+1} - u_{n-1}}{2h^2} = 0 \tag{3.40}$$

Which gives

$$u_{n+1} = u_{n-1} \tag{3.41}$$

Eq. 3.39 can be rewritten as:

$$u_{n,t} = 2 \cdot \frac{u_{n-1} - u_n}{h^2} \tag{3.42}$$

The final system becomes then:

$$\begin{bmatrix} u_{0,t} \\ u_{1,t} \\ u_{2,t} \\ \vdots \\ \vdots \\ u_{n-1,t} \\ u_{n,t} \end{bmatrix} = \frac{1}{h^2} \begin{bmatrix} 0 & 0 & & & & & \\ -1 & 2 & -1 & & & & \\ & -1 & 2 & -1 & & & \\ & & \ddots & \ddots & & & \\ & & & \ddots & \ddots & \ddots & \\ & & & -1 & 2 & -1 & \\ & & & & 2 & -2 & \end{bmatrix} \begin{bmatrix} u_0 \\ u_1 \\ u_2 \\ \vdots \\ \vdots \\ u_{n-1} \\ u_n \end{bmatrix} + \begin{bmatrix} a \\ 0 \\ 0 \\ \vdots \\ \vdots \\ \vdots \\ 0 \end{bmatrix} \tag{3.43}$$

3.4.3 Introduction of Algebraic Equations

Another alternative to include BCs into the problem, is to translate them in algebraic equation. The result is a Differential Algebraic Equation(DAE) system. The DAE system is generated with the implementation of a Mass matrix M, a matrix that is mainly made of zeros, with 1 on the diagonals corresponding to internal nodes.

$$M_{i,i} = 1, \qquad i = 1, ..n \tag{3.44}$$

$$M_{i,i} = 0, \qquad i = 0, n+1 \tag{3.45}$$

The final system would appear in the form:

$$M \cdot (\vec{u}^T) = f(\vec{u}^T) \tag{3.46}$$

This approach is extremely general, since it allows to take in account a lot of BCs type, without modifying the original discretization matrices.

Implementing Dirchelet BCs

Eq. 3.3 can be implemented in this way (according to the final structure of the problem):

$$0 = a - u_{0,t} = a - u_0 \tag{3.47}$$

And it can be implemented in a DAE system in this way:

$$\begin{bmatrix} 0 & & & & & \\ & 1 & & & & \\ & & \ddots & & & \\ & & & \ddots & & \\ & & & & 1 & \\ & & & & & 0 \end{bmatrix} \begin{bmatrix} u_{0,t} \\ u_{1,t} \\ u_{2,t} \\ \vdots \\ \vdots \\ u_{n-1,t} \\ u_{n,t} \end{bmatrix} = \frac{1}{h^2} \begin{bmatrix} -h^2 & & & & & & \\ -1 & 2 & -1 & & & & \\ & -1 & 2 & -1 & & & \\ & & \ddots & \ddots & & & \\ & & & \ddots & \ddots & \ddots & \\ & & & -1 & 2 & -1 & \\ & & & & \dots & \dots & \end{bmatrix} \begin{bmatrix} u_0 \\ u_1 \\ u_2 \\ \vdots \\ \vdots \\ u_{n-1} \\ u_n \end{bmatrix} + \begin{bmatrix} a \\ 0 \\ 0 \\ \vdots \\ \vdots \\ \vdots \\ 0 \end{bmatrix} \tag{3.48}$$

Implementing Neumann BCs

Eq. 3.4 can be interpreted in this way:

$$0 = \left.\frac{\partial u}{\partial x}\right|_{x=1} = -\frac{u_n - u_{n-1}}{h} \tag{3.49}$$

The final system becomes then:

$$\begin{bmatrix} 0 & & & & & \\ & 1 & & & & \\ & & \ddots & & & \\ & & & \ddots & & \\ & & & & 1 & \\ & & & & & 0 \end{bmatrix} \begin{bmatrix} u_{0,t} \\ u_{1,t} \\ u_{2,t} \\ \vdots \\ \vdots \\ u_{n-1,t} \\ u_{n,t} \end{bmatrix} = \frac{1}{h^2} \begin{bmatrix} -h^2 & & & & & & \\ -1 & 2 & -1 & & & & \\ & -1 & 2 & -1 & & & \\ & & \ddots & \ddots & & & \\ & & & \ddots & \ddots & \ddots & \\ & & & -1 & 2 & -1 & \\ & & & & -h & h & \end{bmatrix} \begin{bmatrix} u_0 \\ u_1 \\ u_2 \\ \vdots \\ \vdots \\ u_{n-1} \\ u_n \end{bmatrix} + \begin{bmatrix} a \\ 0 \\ 0 \\ \vdots \\ \vdots \\ \vdots \\ 0 \end{bmatrix} \tag{3.50}$$

3.5 Solving the semi-discrete ODEs system

Once FD schemes have been applied, we have a DAEs or ODEs system. Hence, only time derivative needs to be computed. There is plenty of time integrators: Euler, modified Euler, leapfrog methods, Runge-Kutta (RK) and backward differentiation formulas (BDF) methods, and so on. The very

important concepts of accuracy, stability, and ODE stiffness have been introduced. In the next chapters, some of these ideas are pursued further and illustrated with additional example applications. The environment $MATLAB$, which has been used for this work, is provided with several functions dedicated to ODEs integrations. We recall to [55] for a more detailed discussion.

$MATLAB$ is provided with the ODE solver $ode15s$, which can be applied to stiff ODEs systems with singular mass matrix, that are, namely, DAEs. Other solvers, such as $ode23s$, can only be applied to problems with a constant mass matrix.

Numerical stability

It is worth asking if the full discretized problem (FD scheme and time integrator) is stable. MOL has been subject of several works aimed at studying its stability [50] [49] [56]. In general, one of the most important results is the Lax-Richtmyer theorem, that provides convergence criterion by applying FD schemes to PDEs.

Theorem 2 (of Lax-Richtmyer) *[47] Given a consistent finite difference method for a well-posed linear initial value problem, the method is convergent if and only if it is stable.*

In order to prove this theorem, sometimes it is sufficient to perform a Von-Neumann analysis on the full discretized equations. The Von-Neumann method is based on the assumptions of the existence of a Fourier decomposition of the solution over the finite computational domain in space. This implies the presence of periodic boundary conditions or, from another point of view, that we investigate the stability of the scheme applied at the interior points far enough from the boundaries. The main concept of this method is to study the evolution of the numerical error produced at each step. In this work , we present an alternative to Von-Neumann stability analysis: an eigenvalue based method often referred to as *matrix method*.

This method has two advantages:

1. It allows to estimate the influence of BCs, since we calculate the eigenvalues of the full discretization matrix (assuming they can be evaluated)

2. It allows to study separately the effect of spatial and temporal discretizations.

We show as example an application to our former PDE:

$$u_t = Du_{xx}, \qquad x \in (0,1)$$

If we apply a 3-point-centered stencil we obtain again the following ODEs system:

$$\begin{bmatrix} u_{0,t} \\ u_{1,t} \\ u_{2,t} \\ \vdots \\ \vdots \\ u_{n,t} \end{bmatrix} = \frac{1}{h^2} \begin{bmatrix} 2 & -1 & & & & \\ -1 & 2 & -1 & & & \\ & -1 & 2 & -1 & & \\ & & \ddots & \ddots & & \\ & & & \ddots & \ddots & \\ & & & -1 & 2 \end{bmatrix} \begin{bmatrix} u_0 \\ u_1 \\ u_2 \\ \vdots \\ \vdots \\ u_n \end{bmatrix} \tag{3.51}$$

If we then apply an Explicit Euler method, with time step Δt we get the system:

$$\frac{1}{\Delta t} \left(\begin{bmatrix} u_0 \\ u_1 \\ u_2 \\ \vdots \\ \vdots \\ u_n \end{bmatrix}^{k+1} - \begin{bmatrix} u_0 \\ u_1 \\ u_2 \\ \vdots \\ \vdots \\ u_n \end{bmatrix}^{k} \right) = \frac{1}{h^2} \begin{bmatrix} 2 & -1 & & & & \\ -1 & 2 & -1 & & & \\ & -1 & 2 & -1 & & \\ & & \ddots & \ddots & & \\ & & & \ddots & \ddots & \\ & & & -1 & 2 \end{bmatrix} \begin{bmatrix} u_0 \\ u_1 \\ u_2 \\ \vdots \\ \vdots \\ u_n \end{bmatrix}^{k} \tag{3.52}$$

Where k is the time integration step index. We can obtain then:

$$\begin{bmatrix} u_0 \\ u_1 \\ u_2 \\ \vdots \\ \vdots \\ u_n \end{bmatrix}^{k+1} = \frac{\Delta t}{h^2} \begin{bmatrix} 2 & -1 & & & & \\ -1 & 2 & -1 & & & \\ & -1 & 2 & -1 & & \\ & & \ddots & \ddots & & \\ & & & \ddots & \ddots & \\ & & & -1 & 2 \end{bmatrix} \begin{bmatrix} u_0 \\ u_1 \\ u_2 \\ \vdots \\ \vdots \\ u_n \end{bmatrix}^{k} + \begin{bmatrix} u_0 \\ u_1 \\ u_2 \\ \vdots \\ \vdots \\ u_n \end{bmatrix}^{k} \tag{3.53}$$

$$\begin{bmatrix} u_0 \\ u_1 \\ u_2 \\ \vdots \\ \vdots \\ u_n \end{bmatrix}^{k+1} = \frac{\Delta t}{h^2} \begin{bmatrix} 2+\frac{h^2}{\Delta t} & -1 & & & & \\ -1 & 2+\frac{h^2}{\Delta t} & -1 & & & \\ & -1 & 2+\frac{h^2}{\Delta t} & -1 & & \\ & & \ddots & \ddots & & \\ & & & \ddots & \ddots & \\ & & & -1 & 2+\frac{h^2}{\Delta t} \end{bmatrix} \begin{bmatrix} u_0 \\ u_1 \\ u_2 \\ \vdots \\ \vdots \\ u_n \end{bmatrix}^{k} \tag{3.54}$$

From the eigenvalues of the full discretization matrix (which higly depends upon the spatial discretization stencils), it is possible to establish stability conditions. For more detailed discussion about this topic, we recall to this book [43].

Mathematical models

In this section, the mathematical models proposed to approach the k_{ST} estimation of an explosive dust in a 20L sphere, and the Plug Flow Reactor with its sensitivity analysis are presented.

The aim of this section is to highlight the PDEs generated under conditions and hypotheses proposed, focusing on the structure of the final problem. As a reminder, we recommend taking separately the variable names used for the two presented models, since they have substantially different meanings.

4.1 Estimation of k_{ST} of explosive dusts in a 20 L apparatus

We already mentioned the definition of k_{ST} and its importance in assessing risks related to dust explosions in Chapter 2. Estimations of this parameters are still done mainly by experimental tests. Such tests are particularly expensive (between 2000-2500 €), and they account for a single test. This means that, in a context where it is necessary to evaluate the effect of particle size distribution, an experimental set-up would have absurd costs. Also, the experiments require a certain quantity of dust, that are often neither cheap nor easy to carry to testing facilities. For these reasons, the utility of theoretical predictive models naturally arises. This work aims to predict the k_{ST} of explosive dust, by developing a model that simulates what happens in a 20 L Siwek sphere. This allows for simplifications in the hypothesis: for example, it neglects the need for taking in account secondary explosions, the ignition of the dust cloud is forced by the use of pyrotechnical ignitors, and the dust cloud can be assumed already homogeneously dispersed inside the bomb.

4.1.1 Model description

The idea behind the model is to represent a forced explosion of an organic dust cloud in a closed vessel. The proposed model is applicable to organic dust only, as it will be explained later on. The following dissertation is a summary of the work that we propose in this article [57].

In order to obtain a system of PDEs it is of primary importance to delineate what are the physical phenomena involved. In the considered case we have:

- A dust cloud dispersed in a closed volume
- The ignition of pyrotechnical ignitors (that is, a chemical reaction)
- The heat generated by ignitors is exchanged by convection and radiation to both the dust particles and the surrounding air
- Particles react do the heating from ignitors, triggering pyrolysis and devolatization reactions
- Pyrolysis/Devolatization produce volatiles species that are sent in the air (so we have both mass transfer and energy transfer, since the reaction is overall exothermic)
- The overall process increases the pressure in the closed vessel

Each single element will be analysed an modelled properly, assuming reasonable assumption and simplification when needed. For what concerns the variables state inside the sphere, due to low volume (20 L) it is reasonable to assume that the gas phase is homogeneously mixed. Thus, there are no gradients of temperature or concentration are present inside the vessel. This is extremely important to be considered in this study, since we expect that in bigger apparata, such as the 1 m^3 ISO vessel, this hypothesis is not consistent. The following diagram gives a tentative idea of the model structure.

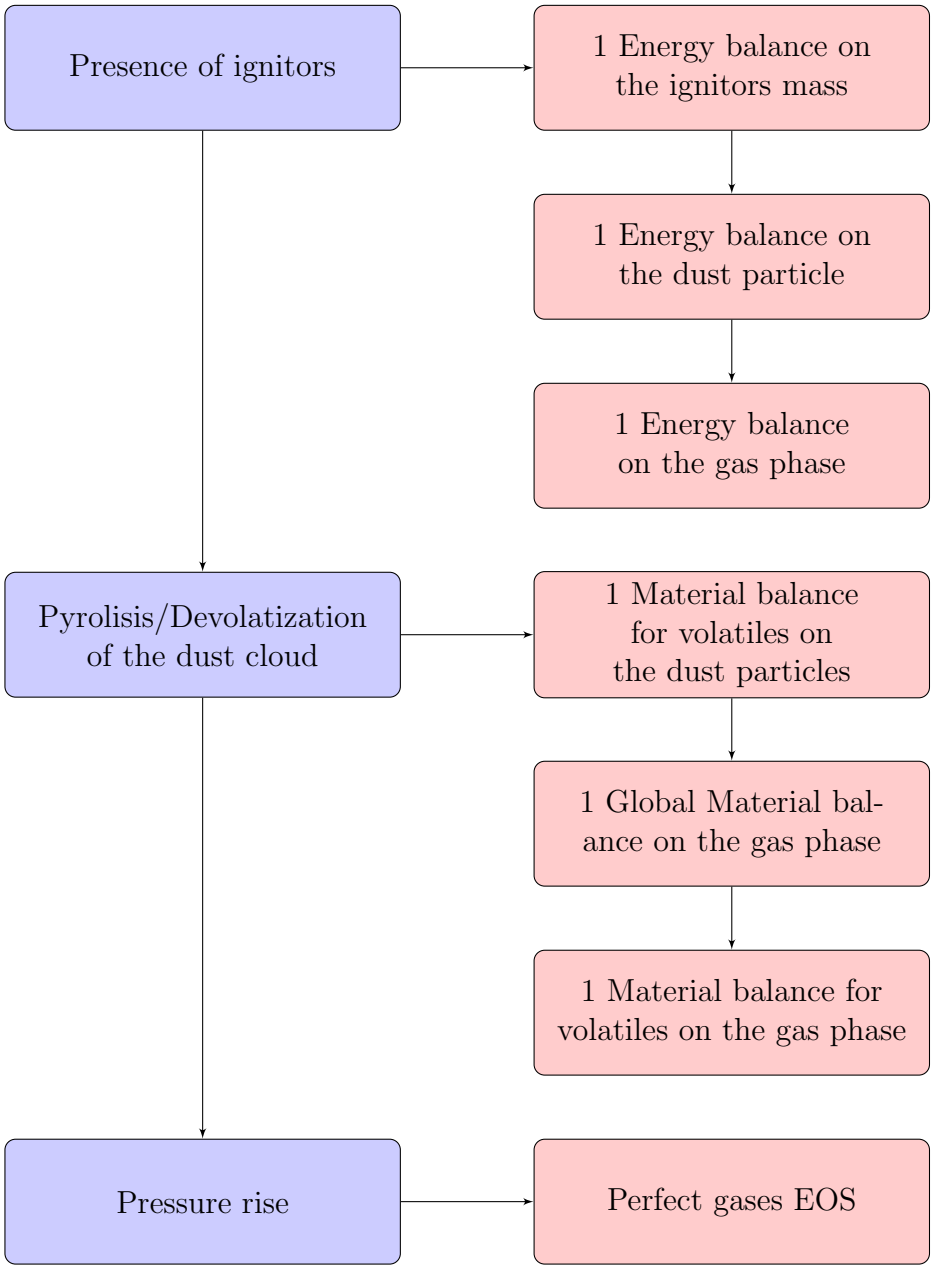

4.1.2 Ignitors model

The standard 20L Siwek apparatus test is processes with 2.4g of ignitors composed by [10], with a total released energy equal to 10 kJ:

- 30% Barium Nitrate ($Ba(NO_3)_2$), MW=261.335 $\frac{g}{mol}$
- 30% Barium Peroxide, MW=169.33 $\frac{g}{mol}$
- 40% Zirconium (Zr), MW=91.22 $\frac{g}{mol}$

Ignitors are triggered with an electrical spark, decomposing Barium Nitrate and Peroxide. Their decomposition produces oxygen, that promotes Zirconium combustion. The combustion of ignitors is extremely violent, and it generates a violent fireball, occupying the whole sphere volume in short times.

Modeling such a phenomenon is a complex task because the oxidation kinetics of both nano and micro Zr particles has not been yet rationalized from a chemical-physical point of view. Therefore, a simplified modeling of the ignitors bursting phenomenon is proposed. We carried out a standard 20 L test (thanks to A. Fumagalli) without any dust inside the sphere in order to evaluate the contribution of the ignitors in terms of heat exchanged with the air inside the test chamber. The corresponding air temperature increase was deducted by applying the perfect gas law on the $p-t$ curve provided by the test:

$$T(t) = \frac{P_{exp}(t) \cdot V_{sphere}}{R \cdot mol_{air}} \tag{4.1}$$

Where $P_{exp}(t)$ is the experimental pressure from the test, V_{sphere} is the sphere volume, R is the perfect gas constant ($8.314 \frac{J}{mol \cdot K}$) and mol_{air} are the moles of air inside the sphere (overtime this is not a constant, due to the combustion, but the value does not change considerably). The temperature increase has been estimated at about 322°C, which corresponds to a total energy released of about 7.783 kJ. Starting from the experimental evidence that no traces of Barium Nitrate, Barium Peroxide, and Zr can be found into the chamber after the ignitors bursting and the amount of heat exchanged by convection with the internal wall of the sphere is negligible, this means that a consistent amount of heat which must be either irradiated towards the internal sphere wall (as no combustible dust particles are present inside the sphere) or consumed for other endothermic phenomena such as the combined heating and partial/total fusion of the Zirconium particles. Based on this observation, the following simplified ignition mechanism, that tries to separate the convective phenomenon (responsible for the heating of the air inside the sphere) from both the radiating and the heating/melting phenomena, can be proposed:

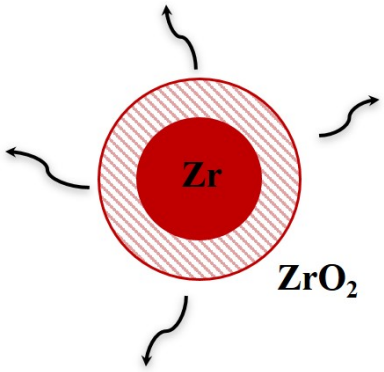

Figure 4.1: Zirconium burning particle

1. Barium Nitrate and Barium Peroxide decompose providing both heat and oxygen to oxidize violently the Zr particles

2. ZrO_2 is formed very rapidly, starting from the outside layer of each Zr particle, as the oxygen diffuses inside the Zr particles

3. this complex oxidation phenomenon produces incandescent hybrid particles (Zr - molten Zr and ZrO_2-molten ZrO_2) which are cooled down by the combined effect of both convection with surrounding air and radiation towards the internal sphere walls (represented in Fig. 4.1)

These last two phenomena can be modelled independently one from the other assuming that:

- The unknown turbulent conditions under which the heat is transferred from the hybrid incandescent particles to the air inside the sphere can be reproduced by fitting the experimental $T - t$ profile obtained by detonating the ignitors inside the empty sphere: this will account for a total amount of heat released equal to 7.783 kJ

- The remaining 2.217 kJ (complement to 10 kJ) must be taken into account in both the heating/melting and radiative terms. As endothermic phenomena linked to the ignitors do not take part in the bursting of another dust inside the sphere, only radiative term should be considered and consequently modelled; particularly, it can be postulated that the hybrid particles are formed of molten ZrO_2 only and they radiate

heat starting from an initial temperature 2715°C (that is ZrO_2 melting point).

It is possible then to write an energy balance equation on a Zirconium particle, which radiates towards the sphere wall:

$$\begin{cases} \dfrac{dT_{Zr}}{dt} = -\dfrac{\sigma A_{zr}}{\rho_{Zr} V_{Zr} c_{p,Zr}} (T_{Zr}^4 - T\mid_{wall}^4) \\ I.C. \qquad T_{Zr}(t=0) = 2715°C \\ A.C. \qquad T|_{wall} = 20°C \end{cases} \tag{4.2}$$

Where dT_{Zr} is the temperature of the particle,σ is the Stefan-Boltzmann constant, T is the temperature inside the vessel,$\frac{A_{zr}}{V_{zr}}$ is the particle surface/volume area, $c_{p,Zr}$ is the specific heat of Zirconium and $\rho_{p,Zr}$ its density. Also the energy balance on the gas phase is needed. If we consider only the convective term coming from the ignitors combustion Q_{ign} we get then:

$$\begin{cases} \rho_{air} \cdot V_{sphere} \cdot c_{p,air} \dfrac{dT}{dt} = Q_{ign} \\ I.C. \qquad T_{air}(t=0) = 25°C \end{cases} \tag{4.3}$$

The quantities presented in Eq. 4.3 are the same of Eq. 4.2, with the subscript *air* indicating gas phase properties. The term Q_{ign} has been estimated using a cubic spline on the curve produced by the test with ignitors loaded only.

The solution of Eq. 4.2 permits to describe the cooling of the incandescent hybrid particles thanks to the radiation towards the sphere walls: particularly, the integral contribution of such a power is approximately 0.65 kJ (hence, a very small amount).

4.1.3 Pyrolisys-Devolatilization model

Solids pyrolysis or devolatilization models abound in the scientific literature but, from a practical point of view, they can be classified in two different groups:

a Models based on the assumption that the solid decomposes directly to volatiles only after reaching a critical temperature [58]

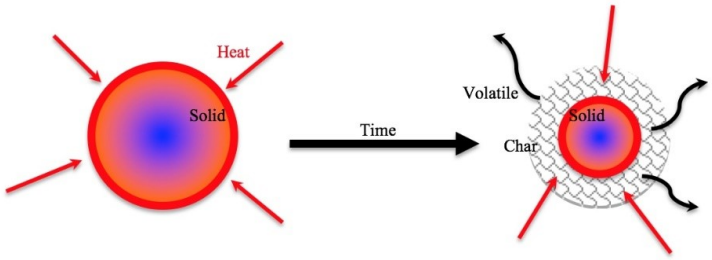

Figure 4.2: Sketch of a single dust particle pyrolysis mechanism

b Models incorporating a kinetic mechanism for the devolatilization process, often inferred from thermo-gravimetric analyses, which allows the solid to decompose over a characteristic temperature range [64] [62].

In the present work, the second approach is applied. For the sake of simplicity, the pyrolysis kinetics is assumed to take place through a single devolatilization step, where part of the solid (**S**) is transformed in volatile compounds (**V**), but a portion, which can be determined using thermogravimetric data, remains as char, the so-called skeleton. The reacting part of the solid **S** is called **r**. This hypothesis is consistent with different organic dust, such as aspirin and sugar [57].

In this way it is possible to consider constant the volume of the bursting particle and, consequently, the porosity of the particle (That is the ratio between the solid residual and the unburned particle) becomes an expression of the combustion rate. In addition, the volatiles leave the particle as they are formed, being immediately available for the combustion process. Fig. 4.2 provides a sketch of the applied model. The subsequent model will require an additional information: the *particle residual*, that will be determined via experimental tests, based on thermogravimetric analysis (TGA)

Thermogravimetric analysis Thermogravimetric analysis (TGA) is an evaluation technique that measures the variation of the mass of a substance as a function of its temperature (that it can be changed according to a predefined temperature ramp or kept constant over a given time interval). It is used to analyze decomposition and/or evaporation rates, oxidation, material purity and many other properties. The temperatures used during thermogravimetric analysis can reach over 1000°C. There are several different

types of furnaces used for thermogravimetric analysis. The furnaces are programmable so that the temperature can be precisely changed at the desired rate. Inside the furnace, there is a pan where the sample is placed when it is ready for analysis. During analysis, data are collected and plotted as mass versus temperature, as shown in Fig. 4.3. In TGA, the exchange of materials between the sample and the immediate surroundings must be possible. The crucible is therefore either open or covered using a lid with a hole. The measurements are normally performed with a dynamic temperature program at rates between 0.5 and 50 $\frac{K}{min}$, often at 20 $\frac{K}{min}$. A starting temperature of 25°C to 30°C is used in order to detect possible drying of the sample. The final temperature is usually relatively high, (e.g. 600°C for organic substances or ¿1000°C for inorganic samples) because in most cases the decomposition of the sample is also of interest. Most TGA experiments use an inert sample pure gas. This is done so the sample only reacts to temperature during decomposition. When the sample is heated in an inert atmosphere this is called pyrolysis. Pyrolysis is the chemical decomposition of organic materials by heating in the absence of oxygen or any other reagents. Organic samples are often pyrolyzed under a nitrogen atmosphere. The carbon black formed during the pyrolysis process or present in the sample as an additive (e.g. in polymers) is then burnt in an air atmosphere. A purge gas or at least a balance protection gas must be used for all measurements. Most TGA curves display weight losses. These are typically caused by:

- Chemical reactions (decomposition and loss of water of crystallization, combustion, reduction of metal oxides)
- Physical transitions (vaporization, evaporation, sublimation, desorption, drying).

Occasionally a gain in weight is observed. This can result from:

- Chemical reactions (reaction with gaseous substances in the purge gas such as O_2, CO_2 with the formation of non-volatile or hardly volatile compounds)
- Physical transitions (adsorption of gaseous substances on samples such as active charcoal).

In this work, standard TG tests under nitrogen flux will be used to fit the Arrhenius parameters for the pyrolysis kinetics. As all the tests have been

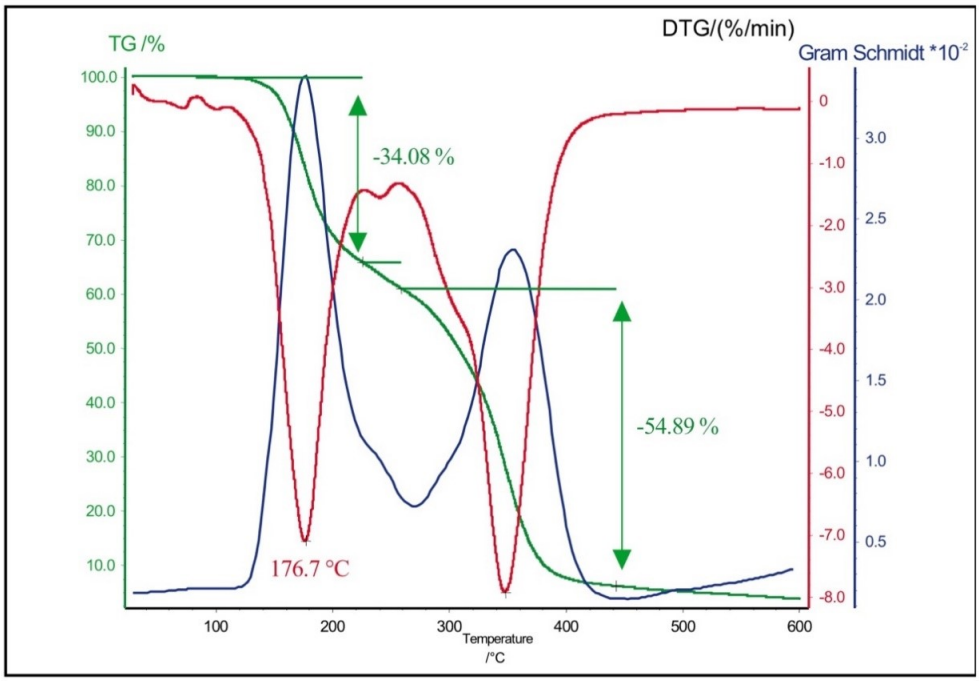

Figure 4.3: TGA of aspirin

taken from the available literature, the heating rates can be different from one test to another. Anyway, this will not be a problem in order to determine reliable devolatilization kinetics as it will be discussed in the next chapter.

4.1.4 Volatiles combustion characterization

Until now, we described how ignitors interact with the system, triggering the combustion of dust particles, and how dust generates volatiles, by introducing the model mentioned above. It is important to remember that the "real" explosion occurs in the gas phase, where pyrolysed sub-products react with the oxygen inside the air. The gas phase reaction needs then to be defined.

We address the gas phase combustion with a lumped pseudo-first order kinetic, described by its constant $k_{c,T}$ $[\frac{1}{s}]$. Due to this strong simplification introduced in the oxidation rate equation, it is necessary to express the combustion kinetic constant as a function of the most representative chemical-physical phenomena involved in the combustion process. Particularly, the

characteristic time of the homogeneous combustion step, t_c, can be roughly estimated as:

$$t_c = \frac{\delta}{S_t} \tag{4.4}$$

δ is the flame thickness, normally about $0.5 - 1\ mm$ [61], and S_t is the turbulent burning velocity of the volatiles which can be estimated with the following relation [65]:

$$S_t = S_{lam}\left(1 + 3.5\frac{u'^{0.5}}{S_{lam}}\right) \tag{4.5}$$

In this case S_{lam} is the laminar burning velocity of the combustible gases and u' is the velocity fluctuation, which was estimated to be, in the 20 L sphere after the usual delay time of 60 ms, equal to 2.68 $\frac{m}{s}$ [60].

Finally, the kinetic constant for the homogenous combustion of the volatiles, can be estimated by knowing the characteristic time t_c:

$$k_{c,T} = \frac{1}{t_c} = \frac{S_{lam}\left(1 + 3.5\frac{u'^{0.5}}{S_{lam}}\right)}{\delta} \tag{4.6}$$

Still, one term remains opened: the laminar burning velocity of the combustible gases S_{lam}. This is one of the most relevant criticalities in the problem definition, because the composition of the volatiles exiting from the bursting dust particles is unknown and it varies in time so quickly that no reliable pyrolysis model can be applied. For this reason, we decide to use the laminar burning velocity of methane in stoichiometric conditions, due to these reasons:

- For the most organic dust, methane is the pyrolysis species produced in major amounts during the bursting process
- Even relevant amount of hydrogen which can be expulsed from the dust does not alter in a significant way the laminar burning velocity of methane
- In the temperatures interval where the k_{ST} of a given organic dust lies (which is between 500-1400°C), the combustion rate is not the controlling phenomenon of the kinetics of the overall deflagration [63]

4.1.5 Balance equations

Now, all the involved phenomena in the dust explosion inside a 20 L sphere have been described and addressed. It is possible then to compute all the necessary material and energy balances required.

The needed balance equations are:

- Material balance on the solid
- Global material balance for the volatiles
- Volatiles material balance in the gas phase
- Energy balance on a single dust particle
- Energy balance on gas phase

This is a summary of the hypotheses imposed for dust explosions, that will be applied in order to compute material and energy balances:

1. 1-D system, spherical symmetry
2. Negligible resistance to mass transfer and diffusion with respect to the convection of the gas phase
3. No secondary reactions for non-volatiles species
4. Thermal equilibrium between solid and volatiles
5. Quasi steady-state assumption for the gas phase
6. The particles preserve their total volume, but their porosity increases during the pyrolysis. This means that the particle volume is constant. The volatiles are produced by the particle, but a portion of the solids generates a sort of residual matrix that is not pyrolyzed.
7. Equal molar and massive velocities
8. The turbulent burning flame velocity is determined by applying a correction on the laminar burning velocity
9. The laminar burning velocity is evaluated as methane stoichiometric combustion

Infinitesimal volume V and surface S of the spherical particle are respectively equal to:

$$\partial V = r^2 \cdot \sin\theta \cdot \partial r \cdot \partial\theta \cdot \partial\phi \tag{4.7}$$

$$\partial S = r^2 \cdot \sin\theta \cdot \partial r \cdot \partial\theta \cdot \partial\phi \tag{4.8}$$

r, θ and ϕ are the standard radius, polar and azimuthal angle for spherical coordinates.

Material balance on the solid

The pyrolysis reaction scheme is:

$$\mathbf{S} \rightarrow \mathbf{V}$$

It is convenient to write the global material balance on the reacting fraction of the solid **r**:

$$\frac{\partial m_{\mathbf{S},\mathbf{r}}}{\partial t} = -k \cdot \rho^n_{\mathbf{S},\mathbf{r}} \cdot V_t \tag{4.9}$$

$$\rho_{\mathbf{S},\mathbf{r}} = \frac{m_{\mathbf{S},\mathbf{r}}}{V_t} = \frac{m_{\mathbf{S}}}{V_t} - \frac{m_{\mathbf{S},0} \cdot \beta}{V_t} \tag{4.10}$$

$$\beta = \frac{m_{\mathbf{S},f}}{m_{\mathbf{S},0}} \tag{4.11}$$

Where: m indicates mass $[kg]$, then $m_{\mathbf{S},\mathbf{r}}$ is the unreacted mass in the particle, $m_{\mathbf{S}}$ is the particle initial mass. k is a kinetic constant for the pyrolysis $[\frac{1}{s}]$ with an order of reaction n $[-]$, $\rho_{\mathbf{S},\mathbf{r}}$ is the effective density of the particle $[\frac{kg}{m^3}]$, V_t is the particle volume $[m^3]$. β is the *particle residual* $[-]$, determined via TGA analysis ($m_{\mathbf{S},0}$ and $m_{\mathbf{S},f}$ are respectively the initial and final mass of dust after the TGA test), performed with a heating rate of 10°C. For the kinetic constant k, we choose the same approach proposed by Fumagalli [63], with a modified Arrhenius equation, leading to the material balance:

$$\begin{cases} \dfrac{\partial \rho_{\mathbf{S},\mathbf{r}}}{\partial t} = -A \cdot exp\left(-\dfrac{E_a \left(1 - \chi\left(\dfrac{\rho_{\mathbf{S},\mathbf{r},0} - \rho_{\mathbf{S},\mathbf{r}}}{\rho_{\mathbf{S},\mathbf{r},0}}\right)\right)}{RT_p} \right) \rho^n_{\mathbf{S},\mathbf{r}} \\ I.C. \qquad \rho_{\mathbf{S},\mathbf{r}}(t=0) = \rho_{\mathbf{S},\mathbf{r},0} = \rho_{\mathbf{S},app,0}(1-\beta) \end{cases} \tag{4.12}$$

Where T_p is the particle temperature $[K]$. Here we introduced:

A,E_a,χ Are kinetic parameters, that will be estimated with the TGA analysys

$\rho_{\mathbf{S},app,0}(1-\beta)$ That is the density of the mass that effectively contributes to pyrolysis

Global material balance for the volatiles

In order to write the indefinite material balance equation for the volatiles present into the gas phase ("void fraction") of the solid dust particle, it is necessary to define an apparent volatiles density as:

$$\rho_{\mathbf{V},app} = \frac{m_{\mathbf{V}}}{V_t} = \frac{m_{\mathbf{V}}}{V_{\mathbf{V}}}\frac{V_{\mathbf{V}}}{V_t} = \rho_{\mathbf{V}} \cdot \varepsilon \tag{4.13}$$

$$\varepsilon = \frac{V_t - V_{\mathbf{S}}}{V_t} \tag{4.14}$$

Where $m_{\mathbf{V}}$ is the mass of volatiles, $V_{\mathbf{V}}$ is the volume of volatiles, and ε is the porosity of the particle (which increases over time, due to pyrolysis).

The balance equation is directly written into spherical coordinates to be consistent with the symmetry of the analyzed system:

$$\frac{\partial \rho_{\mathbf{V},app}}{\partial t} + \frac{\partial}{\partial r}(\rho_{\mathbf{V},app} \cdot v_r) + \frac{2}{r}(\rho_{\mathbf{V},app} \cdot v_r) = k \cdot \rho_{\mathbf{S},\mathbf{r}} \tag{4.15}$$

By imposing steady-state conditions and using porosity ε we get:

$$\frac{\partial}{\partial r}(\rho_{\mathbf{V}} \cdot \varepsilon \cdot v_r) = -\frac{2}{r}(\rho_{\mathbf{V}} \cdot \varepsilon \cdot v_r) + k \cdot \rho_{\mathbf{S},\mathbf{r}} \tag{4.16}$$

We introduced a new variable ν:

$$\nu = \rho_{\mathbf{V}} \cdot \varepsilon \cdot v_r \tag{4.17}$$

And we get the indefinite material balance in the following form:

$$\begin{cases} \dfrac{\partial}{\partial r}(\nu) = -\dfrac{2}{r}(\nu) + k\rho_{\mathbf{S},\mathbf{r}} \\ B.C. \qquad \nu|_{r=0} = 0 \end{cases} \tag{4.18}$$

The $B.C.$ represents the center of the particle, where we have zero density.

Material balance for the volatiles in the gas phase

The mass flow rate of volatiles enters in the gas phase since they are exiting from the surfaces of the N_p dust particles of average radius R:

$$m_{\mathbf{V}} = \nu|_{r=R} \cdot \pi \cdot 4R^2 \cdot N_p \tag{4.19}$$

$\nu|_{r=R}$ is the massive flux of volatiles exiting from the external surface of a single dust particle. In this equation we clearly notice the impact of the particle size, represented by the average radius R, and the effect of dust concentration, that influences N_p.

From this definition, it is possible to calculate the concentration ($\rho_{\mathbf{V}}$, $\frac{kg}{m^3}$) of volatiles inside the sphere (gas phase):

$$\begin{cases} \dfrac{\partial \rho_{\mathbf{V}}}{\partial t} = \dfrac{\nu|_{r=R} \cdot \pi \cdot 4R^2 \cdot N_p}{V_{sphere}} - k_{c,T} \cdot \rho_{\mathbf{V}} \\ I.C. \qquad \rho_{\mathbf{V}}(t=0) = 0 \end{cases} \tag{4.20}$$

Where$k_{c,T}$ can be estimated through Eq. 4.6. The $I.C.$ represents the absence of volatiles as the explosion begins.

Energy balance on a spherical particle

Let us now write the energy balance equation for the whole dust particle (on the control volume, V_t).

Hypothesizing that the heat capacity of the solid phase ($\mathbf{S}$) is constant and much greater than that one of the gaseous phase (volatiles $\mathbf{V}$), we have the general form:

$$\rho_{\mathbf{S},eff} \cdot c_{p,\mathbf{S}} \frac{\partial T_p}{\partial t} = -\nabla(h\mathbf{v} + \mathbf{q}) - q_{pyr} \tag{4.21}$$

Where: T_p is the particle temperature $[K]$, $\rho_{\mathbf{S},eff}$ is an effective solid density, $c_{p,\mathbf{S}}$ is the specific heat capacity for the solid phase $[\frac{J}{kg \cdot K}]$ $\mathbf{q}$ is the conductive heat flux $[\frac{J}{m^2 s}]$, q_{pyr} is the thermal power associated with pyrolysis reaction, h is the enthalpy of the volatiles per unit of volume (we refer only to the gaseous phase because the solid phase cannot be subjected to convective fluxes) $[\frac{J}{m^3}]$.

The general terms are closed in these forms:

$$\rho_{\mathbf{S},eff} = \rho_{\mathbf{S}}(1 - 0.5\varepsilon) = \rho_{\mathbf{S}}(1 - \bar{\varepsilon}) \tag{4.22}$$

$$h = \rho_{\mathbf{V},app} \cdot c_{p,\mathbf{V}} \cdot T_p \tag{4.23}$$

$$\mathbf{q} = -\bar{\lambda}\nabla T_p \tag{4.24}$$

$$q_{pyr} = \Delta H_p \cdot k \cdot \rho^n_{\mathbf{S},\mathbf{r}} \tag{4.25}$$

Thermal convection is closed with the Fourier's law and pyrolysis thermal power is a standard reaction heat power. ΔH_p is the endothermic reaction enthalpy for the pyrolysis reaction $[\frac{J}{kg}]$.$\bar{\lambda}$ is the mean thermal conductivity of the system $[\frac{W}{m^2K}]$. The thermal conductivity of the system is not constant overtime, due to pyrolysis. We consider then an average conductivity, defined with the mean porosity $\bar{\varepsilon}$

$$\bar{\lambda} = \lambda(1 - \bar{\varepsilon}) \tag{4.26}$$

In this case, λ is the conductivity of the pure solid, that is a datum easier to be recovered or estimated.

It is possible now to close the global energy balance on the particle form Eq. 4.21 in this form, by applying spherical coordinates:

$$\rho_{\mathbf{S}}(1 - \bar{\varepsilon}) \cdot c_{p,\mathbf{S}} \frac{\partial T_p}{\partial t} = \lambda(1 - \bar{\varepsilon}) \frac{\partial^2 T_p}{\partial r^2} + \frac{2\lambda(1 - \bar{\varepsilon})}{r} \frac{\partial T_p}{\partial r} - c_{p,\mathbf{V}} \left[T_p \frac{\partial \nu}{\partial r} + \nu \frac{\partial T_p}{\partial r} + \frac{2}{r}(\nu \cdot T_p) \right] - \Delta H_p \cdot k \cdot \rho^n_{\mathbf{S},\mathbf{r}} \tag{4.27}$$

Equation 4.27 needs to be supplemented with 1 $I.C$ and 2 $B.Cs.$. As initial condition, the particle temperature is equal to external air temperature, since nothing yet happened. As first boundary conditions, we have no thermal flux at the particle core. The second $B.C.$ is more complex, since it must take in account what happens at the particle surface:

- Ignitors are radiating towards particles (they are the source of heat that actually activates pyrolysis)
- Particles then exchange heat towards the air due to both convection and radiation (because particles can reach extremely high temperature)

Ignitors are constituted by other radiating particles, leading to an extremely complex phenomenon to be modelled. In order to simplify the implementation of ignitors, it was hypothesized that, as the number of hybrid incandescent particles irradiating on a single dust particle is very high (500 or higher if we have a dust particle of about 30 μm), the ignitors behave as a sort of "hot radiating cloud" whose temperature varies according to a modified version of Eq. 4.2:

$$\begin{cases} \dfrac{dT_{Zr}}{dt} = -\dfrac{\sigma A_{zr}}{\rho_{Zr} V_{Zr} c_{p,Zr}} (T_{Zr}^4 - T\mid_{r=R}^4) \\ I.C. \qquad T_{Zr}(t=0) = 2715°C \end{cases} \tag{4.28}$$

Basically, we assume that the ignitors particles now only radiate towards the dust cloud, and not towards the bomb surface anymore. The final energy balance equation for the particle becomes then:

$$\begin{cases} \rho_{\mathbf{S}}(1-\bar{\varepsilon}) \cdot c_{p,\mathbf{S}} \dfrac{\partial T_p}{\partial t} = \lambda(1-\bar{\varepsilon}) \dfrac{\partial^2 T_p}{\partial r^2} + \dfrac{2\lambda(1-\bar{\varepsilon})}{r} \dfrac{\partial T_p}{\partial r} - \\ \qquad\qquad\qquad\qquad c_{p,\mathbf{V}} \left[T_p \dfrac{\partial \nu}{\partial r} + \nu \dfrac{\partial T_p}{\partial r} + \dfrac{2}{r}(\nu \cdot T_p) \right] - \Delta H_p \cdot k \cdot \rho_{\mathbf{S},\mathbf{r}}^n \\ I.C. \qquad T_p(t=0) = 25°C \\ B.C.(1) \quad \left. \dfrac{\partial T_p}{\partial r} \right|_{r=0} = 0 \\ B.C.(2) \quad \lambda(1-\bar{\varepsilon}) \left. \dfrac{\partial T_p}{\partial r} \right|_{r=R} = -h_c(T_p|_{r=R} - T) - \varepsilon_{em} \cdot \sigma(T_p|_{r=R}^4 - T^4) - \\ \qquad\qquad\qquad\qquad \sigma(T_p|_{r=R}^4 - T_{Zr}^4) \end{cases} \tag{4.29}$$

h_c is the heat transfer coefficient $[\frac{W}{m^2 s}]$, which can be estimated via standard techniques such as [59], and ε_{em} is an emissivity factor $[-]$.

Energy balance on the gas phase

In order to close the system of partial differential equations constituting the predictive model, it is necessary to write an energy balance equation on the phase gas contained in the sphere. The key assumptions are listed in the following:

- Uniform gas phase temperature (this means that no thermal diffusion occurs inside the sphere)

- Negligible amount of pyrolyzed gases into the sphere with respect to the air introduced during the dust inlet
- All the dust particles burst at the same time inside the sphere.

The balance equation becomes then:

$$\begin{cases} \rho_{air} \cdot V_{sphere} \cdot c_{p,air} \dfrac{\partial T}{\partial t} = Q_{ign} + \Delta H_c \cdot k_{c,T} \cdot \rho_{\mathbf{V}} \cdot V_{sphere} + \\ \qquad\qquad h_c \cdot A_p \cdot N_p(T_p|_{r=R} - T) + \varepsilon_{em} \cdot \sigma \cdot N_p(T_p|^4_{r=R} - T^4) \\ I.C. \qquad T(t=0) = 25°C \\ A.C. \qquad Q_{ign} = spline(t_{exp}, Q_{ign,exp}, t) \end{cases} \tag{4.30}$$

As already mentioned, the thermal power from ignitors Q_{ign} is deducted with experimental data, by using the results of a test performed with ignitors loaded only.

Deflagration index estimation

Now all the balance equations to describe the evolution of both mass of the involved substances and temperature inside the 20 L vessel have been defined. We should recall, however, that based on the definition of k_{ST} 2.1, a pressure profile is required. This relation was modified using the ideal gas law in order to express the maximum rate of pressure rise as a function of the rate of gas phase temperature rise (which is directly known from the solution of the PDEs system). The resulting formula is therefore:

$$k_{ST} = \left(n_{air} \frac{R}{V_{sphere}} \right) \left. \frac{dT}{dt} \right|_{max} V_{sphere}^{\frac{1}{3}} \tag{4.31}$$

The term $\left. \dfrac{dT}{dt} \right|_{max}$ is evaluated from the system solution.

4.1.6 Final model

As a reminder, we report all the balance equations used to describe a dust explosion in a 20 L sphere.

$$\begin{cases} \dfrac{\partial \rho_{\mathbf{S},\mathbf{r}}}{\partial t} = -A \cdot exp\left(-\dfrac{E_a \left(1 - \chi\left(\dfrac{\rho_{\mathbf{S},\mathbf{r},0} - \rho_{\mathbf{S},\mathbf{r}}}{\rho_{\mathbf{S},\mathbf{r},0}}\right)\right)}{RT_p} \right) \rho^n_{\mathbf{S},\mathbf{r}} \\ \dfrac{\partial}{\partial r}(\nu) = -\dfrac{2}{r}(\nu) + k \cdot \rho_{\mathbf{S},\mathbf{r}} \\ \dfrac{\partial \rho_{\mathbf{V}}}{\partial t} = \dfrac{\nu|_{r=R} \cdot \pi \cdot 4R^2 \cdot N_p}{V_{sphere}} - k_{c,T} \cdot \rho_{\mathbf{V}} \\ \rho_{\mathbf{S}}(1-\bar{\varepsilon}) \cdot c_{p,\mathbf{S}} \dfrac{\partial T_p}{\partial t} = \lambda(1-\bar{\varepsilon}) \dfrac{\partial^2 T_p}{\partial r^2} + \dfrac{2\lambda(1-\bar{\varepsilon})}{r} \dfrac{\partial T_p}{\partial r} - \\ \qquad\qquad c_{p,\mathbf{V}} \left[T_p \dfrac{\partial \nu}{\partial r} + \nu \dfrac{\partial T_p}{\partial r} + \dfrac{2}{r}(\nu \cdot T_p) \right] - \Delta H_p \cdot k \cdot \rho^n_{\mathbf{S},\mathbf{r}} \\ \rho_{air} \cdot V_{sphere} \cdot c_{p,air} \dfrac{\partial T}{\partial t} = Q_{ign} + \Delta H_c \cdot k_{c,T} \cdot \rho_{\mathbf{V}} \cdot V_{sphere} + \\ \qquad\qquad h_c \cdot A_p \cdot N_p (T_p|_{r=R} - T) + \varepsilon_{em} \cdot \sigma \cdot N_p (T_p|^4_{r=R} - T^4) \end{cases} \tag{4.32}$$

With the following ICs:

$$\begin{cases} \rho_{\mathbf{S},\mathbf{r}}(t=0) & = \rho_{\mathbf{S},app,0}(1-\beta) \\ \rho_{\mathbf{V}}(t=0) & = 0 \\ T_p(t=0) & = 25°C \\ T_{ign}(t=0) & = 2715°C \\ T(t=0) & = 25°C \end{cases} \tag{4.33}$$

And BCs:

$$\begin{cases} \nu|_{r=0} = 0 \\ \left.\dfrac{\partial T_p}{\partial r}\right|_{r=0} = 0 \\ \lambda(1-\bar{\varepsilon}) \left.\dfrac{\partial T_p}{\partial r}\right|_{r=R} = -h_c(T_p|_{r=R} - T) - \varepsilon_{em} \cdot \sigma(T_p|^4_{r=R} - T^4) - \\ \qquad\qquad \sigma(T_p|^4_{r=R} - T^4_{Zr}) \end{cases} \tag{4.34}$$

And, from the PDEs system solution, we deduce the k_{ST} with this relation:

$$k_{ST} = \left(n_{air} \frac{R}{V_{sphere}} \right) \left. \frac{dT}{dt} \right|_{max} V_{sphere}^{\frac{1}{3}} \tag{4.35}$$

The proposed model requires a certain amount of physical-chemical properties, some of those need to be evaluated with TGA experiments. For this reason, we selected 8 types of organic dusts, we evaluated their specific properties, and applied the MOL in order to solve the PDEs system and estimate their k_{ST}, comparing the results with available experimental measurements, taking also in account for different particle size distributions. The selected substances are:

- Aspirin
- Cork
- Corn starch
- Niacin
- Polyethylene
- Polystyrene
- Sugar
- Wheat flour

Results will be discussed in the next chapter.

4.2 Plug Flow Reactor models

A plug flow reactor consists basically of a vessel, a tube or a duct, through which the reacting fluid flows, in a continuous reaction process. These reactors have normally a cylindrical geometry, characterized by a constant cross-sectional area and a constant diameter. The plug flow is a simple model of the velocity profile of a fluid through a pipe, where the velocity is assumed to be constant across any cross-section perpendicular to the axis of the pipe. As a consequence of this hypothesis, it is assumed that there is no mixing in the direction of the flow and complete mixing in the perpendicular direction. In

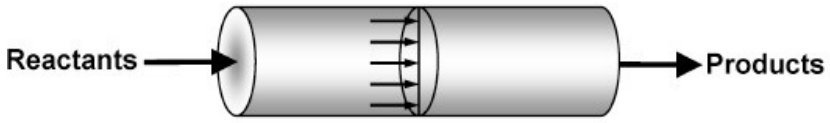

Figure 4.4: Simple Plug Flow reactor scheme

the standard model, both molecular diffusion and dispersive mixing processes are neglected. As long as the axial dimension of the reactor is much larger than the radial one, which is the case for tubular reactors, it is consistent to postulate the neglection of radial effects, such as radial dispersion. In a real PFR process, the temperature control is accomplished by the installation of a thermal jacket on the reactor. It is possible to install a temperature controller, in order to modulate the inlet temperature, according to the information of the temperature profile given by the eventual thermocouples installed along the tube.

A brief summary on process control

Any process or system is subjected to perturbations. Such perturbations, for a chemical process, can be random errors coming from outside, like a variation on the inlet temperature or a composition change in a feed. The process itself also can induce perturbations: an exothermic reaction will increase over time the temperature of a system, with all the possible consequences. For such reasons, controlling variables in process industry has always been a critical and deeply studied aspect[67], with the aim of improving the system performance and also keeping it at a stable state.

Some needed definitions are reported[1]:

Process variable Every generic variable y that characterizes a system (note: all process variables must be considered time dependent)

Measured variable The numerical value y_m associated with the variable y, it requires a measurement system

Controlled varialble A process variable which value must be controlled

[1]For a more detailed discussion, we recommend this book [66]

Manipulated variable The variable that is manipulated in order to control the system

Set-point The target value y_{sp} of the controlled variable y

Historically, until the '40s we see process variable controllers entirely based on human action: the operator has complete freedom in modifying the system status, depending on his personal knowledge and experience and on the available on-line data for the process. Between the '40s and '70s, analogical controllers have been introduced. These type of control strategy is aimed to automate the procedure, by using a signal coming from a measurement instrument. This signal, which intensity is proportional to the entity of the measure, is sent to a device able to elaborate it and to act on the system in a suitable way. However, analogical controllers never found a solid application in process industry. Lately, we find digital controllers. In this case, the signal from the measurement device is transformed in a digital signal, it can be read by a software that produces as answer another digital signal, that will be sent to devices able to modify the state of the system (generally, valves). Digital controllers are still today the most used devices in the field of process variable control.

Actually, three main control strategies can be used:

- Open loop
- Feed-forward control
- Feed-back control

With open loop, it is indicated a system without any automatized control action. An example of this is complete human action based control. The feed-forward strategy, schematized in Fig. 4.5, tries to predict the effect that the measured disturbance will have on the system, and suppresses it before it starts affecting it. This strategy is used for suppression of external errors. It must be noticed, though, that an efficient feed-forward system requires a good predictive model, able to evaluate how disturbances will affect the system. In complex environments, such as chemical reactors, this is rarely accomplished.

The feed-back control, schematized in Fig. 4.6 works as it follows:

1. Measures the output variable y, that is already influenced by the disturbances

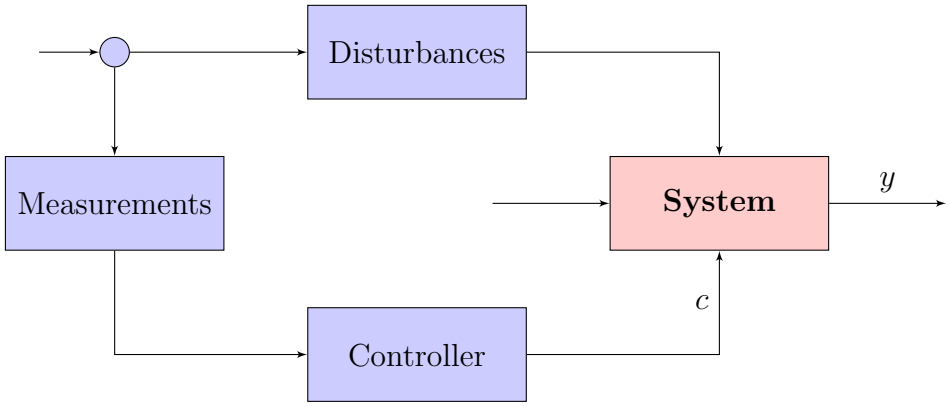

Figure 4.5: Feed-forward control scheme

2. The measured variable y_m is sent to the controller
3. The controller produces an error ε ($\varepsilon(t) = y_{sp} - y_m(t)$), evaluated by comparing the measured variable y_m with the desired set-point value y_{sp}
4. The signal c is then generated by the controller
5. Based on the value of the signal c, the manipulated variable is modified in order to stabilize the system

The main drawback of the feed-back control is that it acts after the disturbances have influenced the system: this means that the control action will always operate under a certain *delay*. However, it does not require a model that predicts the behavior of the system, and for this reason it is the most common strategy used in order to monitor industrial processes. Since this work is based on the application of feed-back strategies for the control of the temperature of a PFR, a brief description of the main feed-back control logics is produced.

P controller The proportional controller, as the name suggests, elaborates a signal over time $c(t)$ that is proportional to the error ε:

$$c(t) = K_p \cdot \varepsilon + c_s$$

Where:

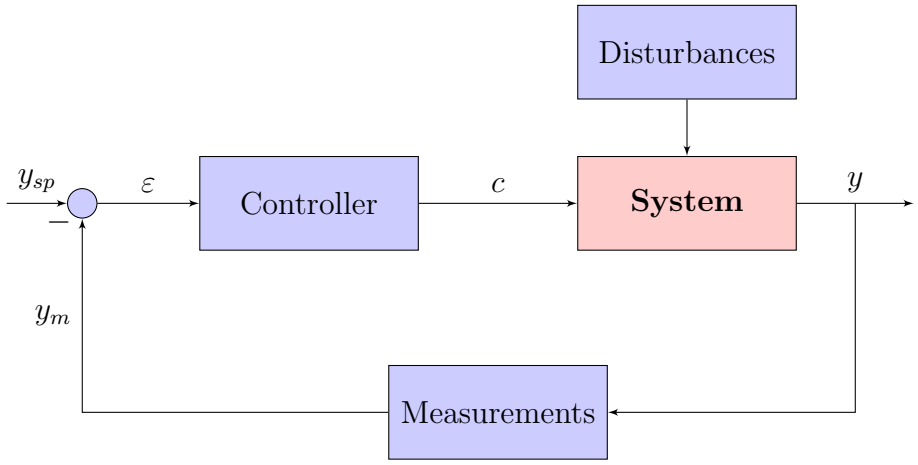

Figure 4.6: Feed-back control scheme

- K_p is the static gain of the controller (-)
- c_s is the bias signal of the controller

The controller becomes more sensitive to the error ε as K_p increases.

PI controller THe proportional-integral controller introduces the error integral.

$$c(t) = K_p \cdot \varepsilon + \frac{K_p}{\tau_i} \int_0^t \varepsilon(t)dt + c_s$$

The main function of the integral time τ_i can be resumed with: assuming a constant error ε, after a time equal to τ_i, the integral term repeats the action of the proportional term. Due to the integral property, a PI controller is able to mitigate even small errors.

$$\frac{K_p}{\tau_i} \int_0^{t=\tau_i} \varepsilon dt = K_p \varepsilon$$

PID controller

$$c(t) = K_p \cdot \varepsilon + \frac{K_p}{\tau_i} \int_0^t \varepsilon(t)dt + K_p \tau_D \frac{d\varepsilon}{dt} + c_s$$

τ_D is the time derivative constant. The action of the derivative component is to anticipate the error behavior. Assuming a constant error over time, the derivative component is none. The main drawback of the PID controller is to introduce in the system heavy oscillattions, that can lead to instability.

4.2.1 1-D PFR models

The PFR models proposed are developed upon base hypotheses acknowledged for this type or reactors. We won't discuss them excessively, since they have been already deeply studied and validated in former works. Basically, we analyze axial PFRs (with one spatial dimension). This a summary of the hypotheses imposed for all the proposed PFR models:

1. Flat velocity profile along the reactor radial coordinate
2. No radial variations in concentrations or temperature
3. Perfect mixing in the radial direction
4. Presence of axial gradients in concentration and temperature (diffusion)
5. Constant reacting mixture density (reasonable for some liquids; valid also for gases only if there is neither pressure drop nor any large temperature change)
6. Constant inlet velocity, which is equal to the axial velocity

PFR model with constant temperature jacket

If we consider a jacket around the reactor with a constant temperature, we have the following transport equations: Material balance equation:

$$\frac{\partial C_i}{\partial t} = -\frac{\partial}{\partial x}\left(-\wp_i \cdot \frac{\partial C_i}{\partial x}\right) - v_x \cdot \frac{\partial C_i}{\partial x} + R_i \qquad i = 1, ..., NC \tag{4.36}$$

Where C_i is the concentration of the $i-th$ substance $[\frac{mol}{m^3}]$, x is the spatial direction $[m]$, t is the time $[s]$, $\wp_i$ is the diffusion coefficient for i $[\frac{m^2}{s}]$, v_x is the velocity of the fluid inside the reactor $[\frac{m}{s}]$, R_i is the reaction term $[\frac{mol}{m^3 s}]$.

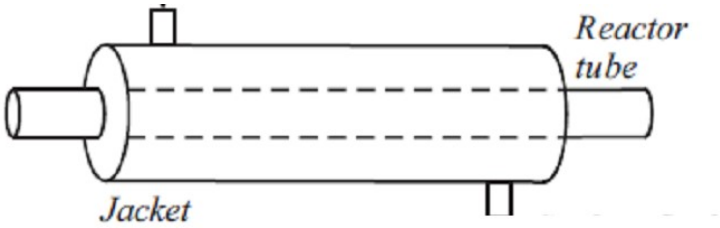

Figure 4.7: Simple Plug Flow reactor scheme

We will have as much equation as much components NC are present inside the reactor. With the following ICs and BCs:

$$\begin{cases} IC & C_i(t=0,x) = C_0 \\ B.C.(1) & C(t,x=0) = C_0 \\ B.C.(2) & \left.\dfrac{\partial C_i}{\partial x}\right|_{x=L} = 0 \end{cases} \tag{4.37}$$

The BCs represent respectively a constant inlet inside the reactor, and no material transport at the reactor exit. Reactor energy balance equation:

$$\frac{\partial T}{\partial t} = -\frac{\partial}{\partial x}\left(-\frac{\alpha}{\rho c_{p,mix}} \cdot \frac{\partial T}{\partial x}\right) - v_x \cdot \frac{\partial T}{\partial x} + \sum_{j=1}^{NR} \frac{\Delta H_{rxn,j}}{\rho \cdot c_{p,mix}} \cdot R_j - \frac{4U_i}{d_i \cdot \rho \cdot c_{p,mix}} \cdot (T - T_{cool}) \tag{4.38}$$

Where T is the reactor temperature $[K]$, α is the thermal diffusion coefficient $[\frac{m^2}{s}]$, ρ is the fluid density $\frac{kg}{m^3}$, $c_{p,mix}$ is the average specific heat of the fluid $\frac{J}{kg \cdot K}$, $\Delta H_{rxn,j}$ is the enthalpy reaction for the reaction j $\frac{J}{kg}$, U_i is the global heat exchange coefficient between reactor and jacket $\frac{W}{m^2 K}$, d_i is the internal diameter $[m]$, T_{cool} is the cooling/heating fluid temperature. NR is the total number of reactions considered. With the following ICs and BCs:

$$\begin{cases} IC & T(t=0,x) = T_{in} \\ B.C.(1) & T(t,x=0) = T_{in} \\ B.C.(2) & \left.\dfrac{\partial T}{\partial x}\right|_{x=L} = 0 \end{cases} \tag{4.39}$$

Their meaning is substantially the same as the ones for the material balances. The implication of t a constant temperature reactor is of course a simplification, which allows for avoiding the addition of other balance equations to

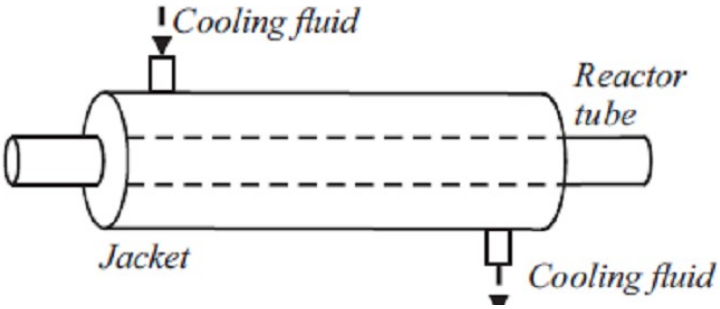

Figure 4.8: Simple Plug Flow reactor scheme

the problem. In real cases, we never have constant temperature jackets, but it can be almost reached with high fluid velocities inside the jacket.

PDEs with this structure are also referred to as *advection diffusion reaction equations*.

PFR model with constant inlet temperature in the jacket

If we want to consider instead a more realistic situation, we should consider the fact that the fluid does not have a constant profile, since it interacts with the reactor itself. In this case, Material and energy equations for the reactor keep the same structure of Eq. 4.37 and Eq. 4.38, with the only difference that T_{cool} is not a constant anymore, but it is a new variable, that requires an energy balance on the jacket in order to be estimated. For this equation, we consider a jacket with only advection term. The jacket balance equation appears then in this form:

$$\frac{\partial T_{cool}}{\partial t} = -v_{cool} \cdot \frac{\partial T_{cool}}{\partial x} - \frac{4U_i}{d_i \cdot \rho_{cool} \cdot c_{p,cool}} \cdot (T - T_{cool}) - \frac{4U_e}{d_e \cdot \rho_{cool} \cdot c_{p,cool}} \cdot (T_{cool} - T_{env}) \tag{4.40}$$

Where v_{cool} is the cooling system velocity $[\frac{m}{s}]$, U_e is the global heat exchange coefficient between jacket and external air $\frac{W}{m^2 K}$, ρ_{cool} is density of the thermoregulating fluid $\frac{kg}{m^3}$, $c_{p,cool}$ is its specific heat $[\frac{J}{kg \cdot K}]$, d_e is the external diameter $[m]$, T_{env} is the air temperature. With the following IC and BC:

$$\begin{cases} IC & T(t=0,x) = T_{cool,IN} \\ B.C. & T_{cool}(t, x=0) = T_{cool,IN} \end{cases} \tag{4.41}$$

PFR model with temperature controller

In this case, the presence of a temperature controller is considered. For a PFR, the temperature control action is very complex to be realized because there is a temperature profile along the reactor itself. It is also impossible to collect the function $T_m(t, x)$, that is the measured temperature as a continuous function of time and axial coordinate. What is actually done is the installation of a single or some thermocouples along the reactor tube. The collected temperatures will be recorded and elaborated by the digital controller in order to establish what should be the value of the manipulated variable. But what is the manipulated variable? For PFRs, a good way to control the temperature of the system is to manipulate the heat exchanged by the reactor jacket. This can be done in two different ways:

- Manipulating the flow rate of the coolant/heating fluid
- Manipulating the inlet temperature of the coolant/heating fluid

The second strategy will be considered for the controlled PFR model. As it will be explained later, the considered case study will use a thermoregulating system that exploits a mixture of molten salts as the cooling/heating medium. A molten salt heat exchanger is always provided with its own thermoregulating system (the temperature of the molten salts mixture is an important parameter to keep under a certain range), and thus controlling the inlet temperature is generally an easy task to be performed in a real process. So, starting from the PDE systems previously presented (section 4.8), the inlet temperature $T_{cool,IN}$ is not a constant anymore, but a system variable, manipulated by the temperature control system. It is important to notice that the implementation of the first strategy, based on manipulating the flow rate of the coolant/heating medium, would change the final PDE system in a different way, and it will not be analyzed in this work.

Considering a single thermocouple at the reactor outlet (so at $x = L$), we have the following control equation for the P controller:

$$\left.\frac{\partial T_{cool}}{\partial t}\right|_{x=0} = K_p \left.\frac{\partial T}{\partial t}\right|_{x=L} \tag{4.42}$$

And the following relation for the PI controller:

$$\left.\frac{\partial T_{cool}}{\partial t}\right|_{x=0} = K_p \left[\left.\frac{\partial}{\partial t}\right|_{x=L} - \frac{1}{\tau_i}(T_{sp} - T(t, x = L))\right] \tag{4.43}$$

PID controller won't be considered, due to the instability introduced in the system. If more thermocouples are installed, it is necessary to introduce a function that decides how to use the multiple measured data: some options can be to consider only the maximum temperature recorded, or to use a mean of the measured values. Their effect on the system behavior should be deeply studied, since it can affect the stability of the system. It is important to notice that the number of thermocouples must be limited, since they require a certain physical portion of the reactor in order to be installed. For this reason, the maximum number achievable is between 3 and 5 thermocouples. The positioning of the thermocouple is another crucial parameter: a thermocoupled placed near the hot-spot of the reactor will generate great errors ε and could potentially induce high fluctuations of the manipulated variable, leading to an unstable system. By the other side, a thermocouple installed in a stable point of the system, will have minimal impact on the system, leaving uncontrolled the part of the reactor where the high exothermicity takes place.

The proposed equations replace the boundary condition of the jacket energy balance (eq. 4.41) in this way:

$$\begin{cases} IC & T(t=0,x) = T_{cool,IN} \\ B.C. & \left.\dfrac{\partial T_{cool}}{\partial t}\right|_{x=0} = K_p \left.\dfrac{\partial T}{\partial t}\right|_{x=L} \end{cases} \tag{4.44}$$

For the P controller and:

$$\begin{cases} IC & T(t=0,x) = T_{cool,IN} \\ B.C. & \left.\dfrac{\partial T_{cool}}{\partial t}\right|_{x=0} = K_p \left[\left.\dfrac{\partial T}{\partial t}\right|_{x=L} - \dfrac{1}{\tau_i}(T_{sp} - T(t,x=L)) \right] \end{cases} \tag{4.45}$$

For the PI option.

4.2.2 Case study: Oxidation of Naphthalene

Now that we developed models for characterizing a generic 1-D PFR under several conditions, the proposed system needs to be closed. The material and energy balances have still an open term inside them: the reaction term R. Unfortunately, due to the extremely high variety of existing chemical processes, it is not possible to establish a single relation able to describe every

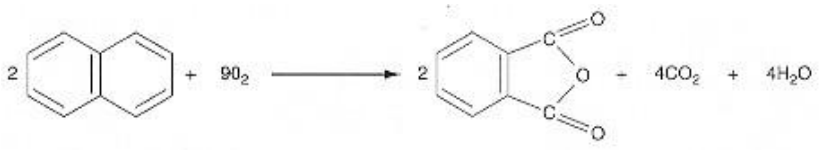

Figure 4.9: Napthalene oxidation reaction scheme

possible reaction. For this reason, it is necessary to define the class of reactions that we want to take in account. For the purposes of this work, it was necessary to select reactions that have been both already studied in the current literature, in order to have a solid comparison for evaluating the quality of results, and also would lead to a numerically stable final algorithm. The oxidation of napthalene has been chosen as the candidate to be studied. This reaction has already been studied in the'70s [36], in the '80s [29], it has been reconsidered by Varma et al. [37].The main reaction scheme is shown in Fig. 4.9 The main target of these works was the implementation of sensitivity criteria in order to define and better understand the safety issues of this process, by defining the parametric sensitivity boundary regions. Naphthalene oxidation is a highly exothermic reaction ($\Delta H = -428kcal/mol = -1792kJ/mol$) [36], carried out commercially on a V_2O_5 catalyst with a lifetime of 2-4 years and it is deactivated mainly in hot spots. The temperature operating condition is in a range between 380°C and 450°C. The reaction runs in a multitubular reactor with thousands of tubes with a diameter of 1 inch and a length of 2 meters, thermoregulated by circulating molten salts. Fig 4.10 shows the process flow diagram. Naphthalene is an aromatic hydrocarbon produced from oil and used mainly for the production of phthalic anhydride (PA). Phthalic anhydride is a toxic, white crystalline compound used in the manufacture of phthaleins and other dyes, resins, plasticizers, and insecticides, so it is a versatile intermediate in organic chemistry. The primary use of phthalic anhydride is as a chemical intermediate in the production of plastics from vinyl chloride. Phthalate esters that function as plasticizers are derived from phthalic anhydride. Phthalic anhydride has another major use in the production of polyester resins and other minor uses in the production of alkyd resins used in paints and lacquers, certain guys, insect repellents, and urethane polyester polyols. Phthalic anhydride has also been used as a rubber scorch inhibitor and retarder. The second largest outlet for PA is in unsaturated polyester resins (UPR) which are usually blended with glass

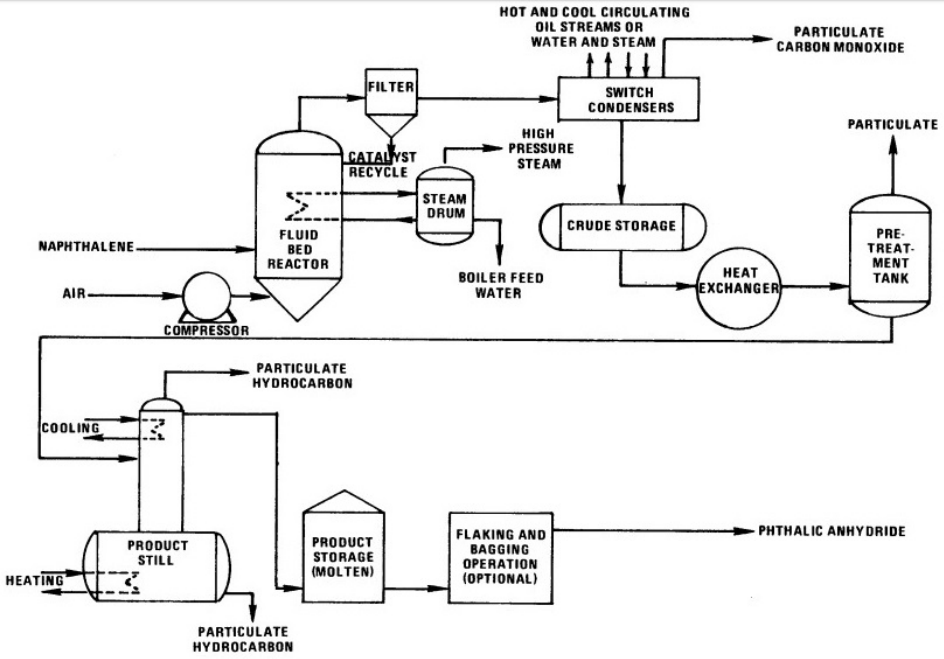

Figure 4.10: Napthalene oxidation process scheme

fibers to produce fiberglass-reinforced plastics. Principal markets are construction, marine and transportation. The third largest outlet is PA-based alkyd resins that are used in solvent-based coatings for architectural, machinery, furniture and fixture applications. Small volume uses for PA include the manufacture of dyes and pigments, detergents, herbicides and insecticides, fire retardants, saccharin and polyester resin cross-linking agents.

According to [36], napthalene oxydation can be assumed to be treated as a pseudo first-order reaction in gas phase, with the following relation for the reaction term R, defined for the $i-th$ component:

$$R_i = \nu_i \cdot A \cdot exp\left(\frac{-E_{att}}{RT}\right) \cdot P_O \cdot P_{napht} \cdot \rho_S \tag{4.46}$$

Where A is the pre-exponential factor $\frac{1}{s}$, E is the activation energy $[\frac{J}{mol}]$, P_O is the partial pressure of oxygen $[Pa]$, which remains constant in the reactor since this reactant is in excess, ρ_{cat} is density of the catalyst $[\frac{kg}{m^3}]$, and ν_i is the $i-th$ reactant stoichiometric coefficient in the reaction scheme. It can be noticed that eq. 4.46, expresses the reaction term as a function of the partial naphtalene pressure P_{napht}, while mass balances are expressed as function of concentration. This is easily solved by using the perfect gases law, that is a fairly reasonable assumption, considering the high temperatures involved in the process. The term p_{napht} can be replaced by:

$$P_{napht} = \frac{MW \cdot P}{\rho} \cdot C_{napht} \tag{4.47}$$

Where MW is the reacting mixture average molecular weight $[\frac{g}{mol}]$, P is total pressure $[Pa]$ and ρ is the average reacting mixture density $[\frac{kg}{m^3}]$, which is considered constant. And then the mass balance results closed.

Cooling/heating system

The naphthalene oxidation process requires a thermoregulating system in order to work. Basic concepts of temperature control have been already introduced in section 4.2.1. The PFR tubular jacket requires a suitable fluid that controls the reactor temperature. The choice of the fluid is a very important aspect: the temperature range required by the process is the first discriminant that should be looked at. For the purposes of naphthalene oxidation, the jacket should process a fluid in a range between 350-450°C.

Water, of course, can't fit the case. Another option could be pressurized steam. However, the pressures required for such temperatures would give a lot of problems, due to the high shell-side pressure exerted. The best choice for such processes is the use of molten salts as cooler/heater. Molten salts find a lot of application in the process industry [69]. When we refer to them as cooling/heating means, we call them as Heat Transfer Salts (HTS). The application of molten salt for temperature control was originally developed as a heat exchanger for use in the chemical and petroleum process industries, namely the Houdry catalytic cracking and refining units [70]. Nowadays, molten salts are regularly used as heating/cooling media for processes that require high temperatures. It is also possible to produce steam from the outlet heated salts exiting the exothermic process. Considering the temperature range required, we choose a standard HTS for such application, that is a mixture of nitrates, specifically $40\%NaNO_2$, $7\%NaNO_3$, $53\%KNO_3$. Its boiling point is 142,2°C (288F). The average physical properties of molten salts have been taken from literature graphs [68]. All of the system parameters are summarized in table 4.1.

4.2.3 Nondimensional models

Now that the PDE systems are complete, it is possible to perform its nondimensionalization. The nondimensionalization grants those benefits:

- Keep the variables numeric values in a small range (usually between 0 and 1)
- Introduce adimensional parameters with physical interpretation
- Once adimensional parameters are generated, the proposed model acquires more generality and ease of application for similar case studies

For such reasons, the nondimensional proposed model can be effectively extended to all studies on PFR that take in account:

1. One axial dimension for the reactor
2. Material and thermal axial diffusion for the reactor
3. A cooling/heating system

Parameter	Value	Unit	**Parameter**	Value	Unit
A	11.16	$\frac{kmol}{kg \cdot s \cdot kPa^2}$	T_{in}	625	K
E	$1.134 \cdot 10^8$	$\frac{J}{mol}$	ΔH	$1.289 \cdot 10^9$	$\frac{J}{kmol}$
ρ	1.293	$\frac{kg}{m^3}$	c_p	1044	$\frac{J}{Kg \cdot K}$
U	9.61	$\frac{W}{m^2 K}$	MW	29.48	$\frac{kg}{kmol}$
$\wp$	$2 \cdot 10^{-5}$	$\frac{m^2}{s}$	T_{cool}	625	K
ρ_{cat}	1300	$\frac{kg}{m^3}$	v_0	$0.1 - 1.0$	$\frac{m}{s}$
P	101325	Pa	$v_{0,cool}$	$0.1 - 0.5$	$\frac{m}{s}$
P_0	21070	Pa	ρ_{cool}	1820	$\frac{kg}{m^3}$
α	$2.5 \cdot 10^{-5}$	$\frac{m^2}{s}$	$c_{p,cool}$	2.23	$\frac{KJ}{kg \cdot K}$

Table 4.1: List of naphthalene oxidation physical-chemical parameters

Adimensional number	Description
Arrhenius number	$\gamma = \dfrac{E_{att}}{RT_{in}}$
Damkholer number	$Da = \dfrac{L \cdot A \cdot e^{(-\gamma)} \cdot \rho_{cat} P_0 \cdot P \cdot MW}{\rho \cdot v_0}$
Stanton number	$St = \dfrac{4U \cdot L}{d_i \cdot \rho \cdot c_p v_0}$
Coolant Stanton number	$St_c = \dfrac{4U \cdot L}{d_e \cdot \rho_{cool} \cdot c_{p,cool} \cdot v_{0,cool}}$
Adiabatic temperature rise	$B = \dfrac{(-\Delta H) \cdot C_{in}}{\rho c_p T_{in}} \gamma$
Material diffusion parameter	$\delta = \dfrac{\wp}{L v_0}$
Thermal diffusion parameter	$\lambda = \dfrac{\alpha}{L v_0}$

Table 4.2: List of adimensional parameters

4. A temperature controller that uses as manipulated variable the inlet cooling/heating medium temperature

5. A single phase with a first-order reaction, or a reaction that can be treated in this way

We produce then a list of all the nondimensional parameters and variables introduced in the system. Table 4.2 lists all the nondimensional parameters involved in the problem. It is important to notice that each parameter has a well-defined physical interpretation. For example, the Damkholer number is a ratio between reaction rate and convective mass transport rate. As the Damkohler number increases, it means that the reaction rate is higher than the mass transport rate, leading to a so-called mass transfer regime: the chemical reaction is faster then the mass transport, hence the overall chemical reaction rate is decided by the mass transfer.

Table 4.3 shows the nondimensional variables, including their values range. In this case, conversion is a number that shows the amount of reactant that is effectively reacted.

Adimensional variable	Description	Range
Conversion	$\chi = \dfrac{C_{in} - C_{napht}}{C_{in}}$	$0 \leq \chi \leq 1$
Dimensionless temperature	$\theta = \dfrac{T - T_{in}}{T_{in}}\gamma$	$\theta \geq 0$
Dimensionless wall temperature	$\theta_w = \dfrac{T_{cool} - T_{in}}{T_{in}}\gamma$	$\theta_w \geq 0$
Dimensionless axial coordinate	$z = \dfrac{l}{L}$	$0 \leq z \leq 1$
Dimensionless time	$\tau = \dfrac{tv_0}{L}$	$\tau \geq 0$

Table 4.3: List of adimensional variables

We proceed then with the generation of nondimensional PFR models.

PFR model with constant wall temperature

In this case, the system takes in account only the reactor material and energy balances:

$$\begin{cases} \dfrac{\partial \chi}{\partial \tau} = \delta \dfrac{\partial^2 \chi}{\partial z^2} - \dfrac{\partial \chi}{\partial z} + Da \cdot exp\left(\dfrac{\theta}{1 + \dfrac{\theta}{\gamma}}\right) \cdot (1 - \chi) \\ \dfrac{\partial \theta}{\partial \tau} = \lambda \dfrac{\partial^2 \theta}{\partial z^2} - \dfrac{\partial \theta}{\partial z} + B \cdot Da \cdot exp\left(\dfrac{\theta}{1 + \dfrac{\theta}{\gamma}}\right) \cdot (1 - \chi) - St(\theta - \theta_w) \end{cases} \tag{4.48}$$

Note that in this case the cooling/heating medium temperature θ_w is a constant. With the following ICs and BCs:

$$\begin{cases} I.C.s & \chi(\tau=0,z)=0 \\ & \theta(\tau=0,z)=0 \\ B.C.s & \chi(\tau,z=0)=0 \\ & \left.\dfrac{\partial\chi}{\partial z}\right|_{z=1}=0 \\ & \theta(\tau,z=0)=0 \\ & \left.\dfrac{\partial\theta}{\partial z}\right|_{z=1}=0 \end{cases} \tag{4.49}$$

PFR model with cooling/heating system

The adimensional PDE systems shows in order: material balance equation, reactor energy balance equation and jacket energy balance equation.

$$\begin{cases} \dfrac{\partial\chi}{\partial\tau}=\delta\dfrac{\partial^2\chi}{\partial z^2}-\dfrac{\partial\chi}{\partial z}+Da\cdot exp\left(\dfrac{\theta}{1+\dfrac{\theta}{\gamma}}\right)\cdot(1-\chi) \\ \dfrac{\partial\theta}{\partial\tau}=\lambda\dfrac{\partial^2\theta}{\partial z^2}-\dfrac{\partial\theta}{\partial z}+B\cdot Da\cdot exp\left(\dfrac{\theta}{1+\dfrac{\theta}{\gamma}}\right)\cdot(1-\chi)-St(\theta-\theta_w) \\ \dfrac{\partial\theta_w}{\partial\tau}=-\dfrac{\partial\theta_w}{\partial z}-St_c(\theta-\theta_w)-St_e(\theta_w-\theta_{env}) \end{cases} \tag{4.50}$$

With the following ICs and BCs:

$$\begin{cases} I.C.s & \chi(\tau=0,z)=0 \\ & \theta(\tau=0,z)=0 \\ & \theta_w(\tau=0,z)=0 \\ B.C.s & \chi(\tau,z=0)=0 \\ & \left.\dfrac{\partial\chi}{\partial z}\right|_{z=1}=0 \\ & \theta(\tau,z=0)=0 \\ & \left.\dfrac{\partial\theta}{\partial z}\right|_{z=1}=0 \\ & \theta_w(\tau,z=0)=0 \end{cases} \tag{4.51}$$

PFR model with temperature controller

For the temperature control, we consider a single thermocouple placed in position z_c. As already stated, the PDE system maintains the same structure of Eq. 4.50, the temperature control equation substitutes the cooling/heating system BC. If a P controller is installed we get:

$$\begin{cases} I.C.s & \chi(\tau=0,z)=0 \\ & \theta(\tau=0,z)=0 \\ & \theta_w(\tau=0,z)=0 \\ B.C.s & \chi(\tau,z=0)=0 \\ & \left.\dfrac{\partial\chi}{\partial z}\right|_{z=1}=0 \\ & \theta(\tau,z=0)=0 \\ & \left.\dfrac{\partial\theta}{\partial z}\right|_{z=1}=0 \\ & \left.\dfrac{\partial\theta_w}{\partial\tau}\right|_{z=0}=K_p\left.\dfrac{\partial\theta}{\partial\tau}\right|_{z=z_c} \end{cases} \tag{4.52}$$

With a PI control logic we have instead:

$$\begin{cases} I.C.s & \chi(\tau=0,z)=0 \\ & \theta(\tau=0,z)=0 \\ & \theta_w(\tau=0,z)=0 \\ B.C.s & \chi(\tau,z=0)=0 \\ & \left.\dfrac{\partial\chi}{\partial z}\right|_{z=1}=0 \\ & \theta(\tau,z=0)=0 \\ & \left.\dfrac{\partial\theta}{\partial z}\right|_{z=1}=0 \\ & \left.\dfrac{\partial\theta_w}{\partial\tau}\right|_{z=0}=K_p\left[\left.\dfrac{\partial\theta}{\partial\tau}\right|_{z=z_c}-\dfrac{1}{\tau_i}(\theta_{sp}-\theta(t,z=z_c))\right] \end{cases} \tag{4.53}$$

Results

In this part we present the result of the application of MOL to the models described in previous chapters. We will discuss both how the MOL has been implemented and the significance of the results achieved.

5.1 Simulation of k_{ST}

The model to simulate the k_{ST} of organic dusts is a mix of ODEs and second and first-order PDEs. Note that every single term in Eq. 4.32 is coupled with other variables, hence they must be treated together. The MOL with the mass matrix apporach, leading to a final DAEs system suits perfectly the problem introduced. We produce Eq. 4.32 in an alternative form, in order to simplify the subsequent application of the Method of Lines:

$$
\begin{cases}
\dfrac{\partial T_p}{\partial t} = \dfrac{\lambda}{\rho_{\mathbf{S}} \cdot c_{p,\mathbf{S}}} \dfrac{\partial^2 T_p}{\partial r^2} + \left(\dfrac{2\lambda}{\rho_{\mathbf{S}} \cdot c_{p,\mathbf{S}} \cdot r} - \nu \dfrac{c_{p,\mathbf{V}}}{\rho_{\mathbf{S}} \cdot (1-\bar{\varepsilon}) \cdot c_{p,\mathbf{S}}} \right) \dfrac{\partial T_p}{\partial r} - \\
\qquad\qquad T_p \left(\dfrac{c_{p,\mathbf{V}}}{\rho_{\mathbf{S}} \cdot (1-\bar{\varepsilon}) \cdot c_{p,\mathbf{S}}} \right) \dfrac{\partial \nu}{\partial r} - \left(\dfrac{\Delta H_p \cdot k \cdot \rho^n_{\mathbf{S},\mathbf{r}} + c_{p,\mathbf{V}} \cdot \frac{2}{r}(\nu \cdot T_p)}{\rho_{\mathbf{S}} \cdot (1-\bar{\varepsilon}) \cdot c_{p,\mathbf{S}}} \right) \\
0 = -\dfrac{\partial \nu}{\partial r} - \dfrac{2}{r}(\nu) + k \cdot \rho_{\mathbf{S},\mathbf{r}} \\
\dfrac{\partial \rho_{\mathbf{S},\mathbf{r}}}{\partial t} = -A \cdot exp \left(- \dfrac{E_a \left(1 - \chi \left(\dfrac{\rho_{\mathbf{S},\mathbf{r},0} - \rho_{\mathbf{S},\mathbf{r}}}{\rho_{\mathbf{S},\mathbf{r},0}} \right) \right)}{R T_p} \right) \rho^n_{\mathbf{S},\mathbf{r}} \\
\dfrac{\partial \rho_{\mathbf{V}}}{\partial t} = \dfrac{\nu|_{r=R} \cdot \pi \cdot 4R^2 \cdot N_p}{V_{sphere}} - k_{c,T} \cdot \rho_{\mathbf{V}} \\
\dfrac{\partial T}{\partial t} = \dfrac{Q_{ign}}{\rho_{air} \cdot V_{sphere} \cdot c_{p,air}} + \dfrac{\Delta H_c \cdot k_{c,T} \cdot \rho_{\mathbf{V}}}{\rho_{air} \cdot c_{p,air}} + \dfrac{h_c \cdot A_p \cdot N_p (T_p|_{r=R} - T)}{\rho_{air} \cdot V_{sphere} \cdot c_{p,air}} + \\
\qquad \dfrac{\varepsilon_{em} \cdot \sigma \cdot N_p (T_p|^4_{r=R} - T^4)}{\rho_{air} \cdot V_{sphere} \cdot c_{p,air}} \\
\dfrac{dT_{Zr}}{dt} = -\dfrac{\sigma A_{zr}}{\rho_{Zr} V_{Zr} c_{p,Zr}} (T^4_{Zr} - T\,|^4_{r=R})
\end{cases}
\tag{5.1}
$$

We added the energy balance equation for the ignitor because it is a needed variable for the implementation of the BCs 4.34. In the end, we have 6 equations with the following 6 variables to be estimated:

- Temeprature of the dust particle T_p
- Volatiles production rate ν
- Concentration of dust in the reactant part of the solid $\rho_{\mathbf{S},\mathbf{r}}$
- Concentration of volatiles in the sphere $\rho_{\mathbf{V}}$
- Temperature of the gas phase T
- Ignitors cloud temperature T_{zr}

All the other terms present in the equation system are constant, mean values, or functions of the just mentioned variables.

In order to apply the mass matrix $\mathbf{M}$, which will affect the presence of temporal derivatives, it is important to notice that the balance equation for$\rho_{\mathbf{S},\mathbf{r}}$ depends on temperature particle, that is a function defined on the whole discrete particle grid. With this in mind, considering a mesh made of $m+1$ grid points (can be uniform or not, it will not change this formulation), we want to write Eq. 5.1 in the following form:

$$\boldsymbol{M} \cdot \begin{bmatrix} \boldsymbol{T}_p \\ \boldsymbol{\nu} \\ \boldsymbol{\rho}_{\mathbf{S},\mathbf{r}} \\ \rho_{\mathbf{V}} \\ T \\ T_{Zr} \end{bmatrix}_t = \boldsymbol{A} \cdot \begin{bmatrix} \boldsymbol{T}_p \\ \boldsymbol{\nu} \\ \boldsymbol{\rho}_{\mathbf{S},\mathbf{r}} \\ \rho_{\mathbf{V}} \\ T \\ T_{Zr} \end{bmatrix} + f(\boldsymbol{T}_p, \boldsymbol{\nu}, \boldsymbol{\rho}_{\mathbf{S},\mathbf{r}}, \rho_{\mathbf{V}}, T, T_{Zr}) \tag{5.2}$$

Where:

$\boldsymbol{T}_p, \boldsymbol{\nu}, \boldsymbol{\rho}_{\mathbf{S},\mathbf{r}}$ Indicate the vectors defined on the grid points $(T_{p,0}, T_{p,1} ... T_{p,m})$ and so on

$\boldsymbol{A}$ Is a block matrix that contains all the discretization matrices

f Collects all the additional terms inside the equations

The mass matrix $\mathbf{M}$ assumes then this form:

$$\begin{cases} M_{i,j} = 0 & i \neq j \\ M_{i,i} = 0 & i = 0, m+1, m+2, 2(m+1)+1 \leq i \leq 3(m+1) \\ M_{i,i} = 1 & elsewhere \end{cases} \tag{5.3}$$

To summarize, $\mathbf{M}$ is a $(3m+6 \times 3m+6)$ diagonal matrix equal to 0 when time derivatives are neglected or on BCs, and 1 elsewhere (time derivatives are present).

For what concern the structure of $\mathbf{A}$, it is a block matrix always with dimension $(3m+6 \times 3m+6)$, and it contains the discretization matrices for the differential operators, whenever they are present. In this case, we have first and second derivatives. We will call D_1 the discretization matrix for the first derivative and D_2 the one for the second derivative. For now, let us consider for the sake of simplicity that the BCs are already included in D_1

and D_2. If we consider a uniform grid with step Δx, we can decompose $\mathbf{A}$ as it follows:

$$\mathbf{A} = \frac{1}{\Delta x^2} \begin{bmatrix} \boldsymbol{A}_{1,1} & \boldsymbol{A}_{1,2} & \underline{0}_{(m+1,m+1)} & \underline{0}_{(m+1,1)} & \underline{0}_{(m+1,1)} & \underline{0}_{(m+1,1)} \\ \underline{0}_{(m+1,m+1)} & \boldsymbol{A}_{2,2} & \underline{0}_{(m+1,m+1)} & \underline{0}_{(m+1,1)} & \underline{0}_{(m+1,1)} & \underline{0}_{(m+1,1)} \\ \underline{0}_{(m+1,m+1)} & \underline{0}_{(m+1,m+1)} & \underline{0}_{(m+1,m+1)} & \underline{0}_{(m+1,1)} & \underline{0}_{(m+1,1)} & \underline{0}_{(m+1,1)} \\ \underline{0}_{(1,m+1)} & \underline{0}_{(1,m+1)} & \underline{0}_{(1,m+1)} & 0 & 0 & 0 \\ \underline{0}_{(1,m+1)} & \underline{0}_{(1,m+1)} & \underline{0}_{(1,m+1)} & 0 & 0 & 0 \\ \underline{0}_{(1,m+1)} & \underline{0}_{(1,m+1)} & \underline{0}_{(1,m+1)} & 0 & 0 & 0 \end{bmatrix} \tag{5.4}$$

Where:

$$\mathbf{A}_{1,1} = \left[\frac{\lambda}{\rho_{\mathbf{S}} \cdot c_{p,\mathbf{S}}} D_2 + \Delta x \frac{\lambda}{\rho_{\mathbf{S}} \cdot c_{p,\mathbf{S}}} D_1 \circ [r^{-1}] - \Delta x \frac{c_{p,\mathbf{V}}}{\rho_{\mathbf{S}} \cdot (1-\bar{\varepsilon}) \cdot c_{p,\mathbf{S}}} \boldsymbol{\nu} \circ D_1 \right] \tag{5.5}$$

$$\mathbf{A}_{1,2} = \left[-\Delta x \frac{c_{p,\mathbf{V}}}{\rho_{\mathbf{S}} \cdot (1-\bar{\varepsilon}) \cdot c_{p,\mathbf{S}}} \boldsymbol{T_p} \circ D_1 \right] \tag{5.6}$$

$$\mathbf{A}_{2,2} = [-\Delta x D_1] \tag{5.7}$$

$\circ$ indicates the Hadamard product, that is the component wise product between two matrices. $\underline{0}$ Indicates a zero matrix of a given dimension ICs are trivial, since they are all constant values at $t = 0$. For the BCs, we exploit the mass matrix, by applying the definition of the BCs on the points where they are defined, resulting in manually modifying the specific raw of the related discretization matrix, as shown in Chapter 3.

For the time integration of the resulting DAEs, we implemented it in $MATLAB$ with the implicit solver $ode15s$, that can solve DAEs based on Backward Differentiation Formulas. This solver also accounts for stiff problems, that is our case.

Now that the presented PDEs system can be resolved, we should remind that a lot of parameters are required, that depend on the material of dusts, which are listed below:

- MW of the dust
- λ
- $\rho_{\mathbf{S}}$
- $c_{p,\mathbf{S}}$

- $c_{p,\mathbf{v}}$
- ΔH_c
- ΔH_p
- χ
- E_a
- n
- β

Some of these data can be estimated with TGA analysis, others have been searched in the current literature.

The TG curve of each dust was used to fit the lumped pyrolysis kinetics which was included in the mathematical model in order to take into account the rate at which the volatiles are produced from the dust particle. For each dust, the fitting procedure (we used the minimal square method) was carried out until the maximum slope (before any inflection point) of an experimental TG curve occurred. This is a key point for the correct description of the violence of an organic combustible dust: in fact, what happens to the solid residue after the maximum rate of volatiles expulsion does not contribute to the determination of the k_{ST}; therefore, the corresponding part of the TG curve can be neglected.

Also, in order to evaluate the quality of results, we recovered a list of experimental k_{ST}, that were performed on specific average particle size distribution. We use this average radius inside our model.

The present predictive model was validated testing eight organic dust (Aspirin, Cork, Corn starch, Niacin, Polyethylene, Polystyrene, Sugar and Wheat Flour), whose aforementioned constitutive parameters were available in the literature.

5.1.1 Solution of the PDE system

While the target of the work is the estimation of k_{ST}, that is a local information on the pressure vs time curve, we present the solution of the model, for Corn Starch and Niacin dust. Figure 5.1 compares the prediction of the temperature of the gas phase between experimental data and prediction (with a

mean diameter for the Corn Starch sample of 54 μm). We can notice that our prediction shows a slight delay (about 30 μs) compared to the experimental one. It is notable, analysing Fig. 5.2, that the production of volatiles directly influences the temperature rise of the gas phase. This delay can be caused by several factors: first, or model treats the dust sample as it is composed of equal particles. In the experimental test, we have a particle size distribution, with 54 μm as a mean value. It is possible that the dust deposit is composed by a certain amount of smaller particles, which burn faster respect to the diameter we considered. Figure 5.3 shows the evolution of the temperature particle over time and space.

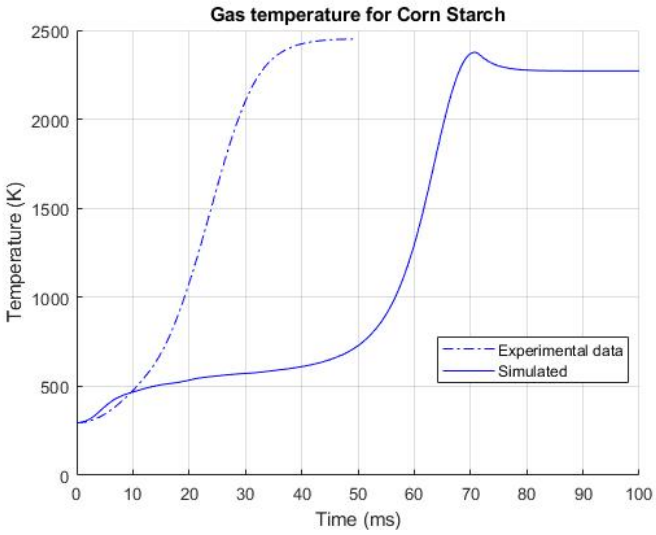

Figure 5.1: Gas temperature for Corn Starch (with average diameter: 54 μm)

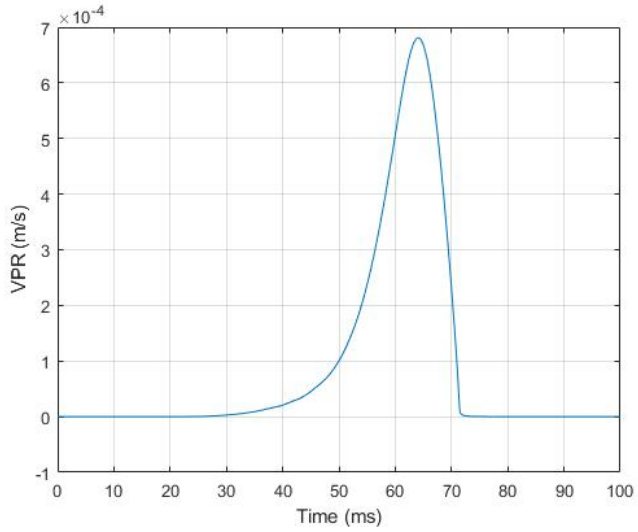

Figure 5.2: Volatile production rate for Corn Starch (with average diameter: 54 μm)

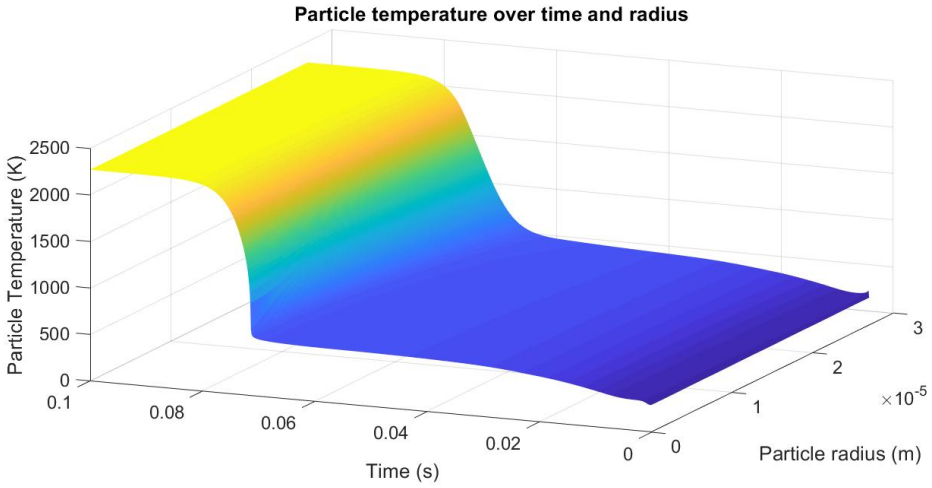

Figure 5.3: Particle temperature for Corn Starch (with average diameter: 54 μm)

Numerical experiments

We compare the results by imposing different tolerances for the convergence of the ODE solver and different FD schemes, with uniform grids. We decided to report the gas temperature for comparisons because it is the most meaningful information for us, since the k_{ST} estimation derives from that. For the choice of the stencil, we applied the *stagewise differentiation* approach [55]: given the discretization matrix for the first derivative D_1 and D_2 for the second one we get for the discretization of the spatial derivative of T_p:

$$\frac{\partial T_p}{\partial r} = D_1 \cdot \boldsymbol{T}_p \tag{5.8}$$

$$\frac{\partial^2 T_p}{\partial r^2} = D_1(D_1 \cdot \boldsymbol{T}_p) \tag{5.9}$$

In this way, from the selection of a stencil for the first derivative, we get recursively the stencil for the second one.

At first we tested the effect of grid dependence on the solution, by imposing Relative Tolerance equal to 1E-6 and Absolute Tolerance equal to 1E-9 as convergence criterion. Table 5.1 shows the computational times. It is notable that the use of a wider stencil, despite leading to less sparse matrices, does not necessarily increases the computational time, due to its greater accuracy.

Scheme	**Grid points**	**Computational time (s)**
3-point-centered	50	8.012669
	100	8.837983
	200	47.711188
	500	179.197717
	1000	776.424542
5-point-centered	50	7.518279
	100	8.847311
	200	28.223463
	500	143.583309
	1000	778.720604

Table 5.1: Computational times with Relative Tolerance equal to 1E-6 and Absolute Tolerance equal to 1E-9

Figure 5.4 shows the solution of the PDE system, comparing the evolution of gas temperature over time with different grids. We see no evidence of grid dependence, since the solutions are completely overlapped considering finer grids.

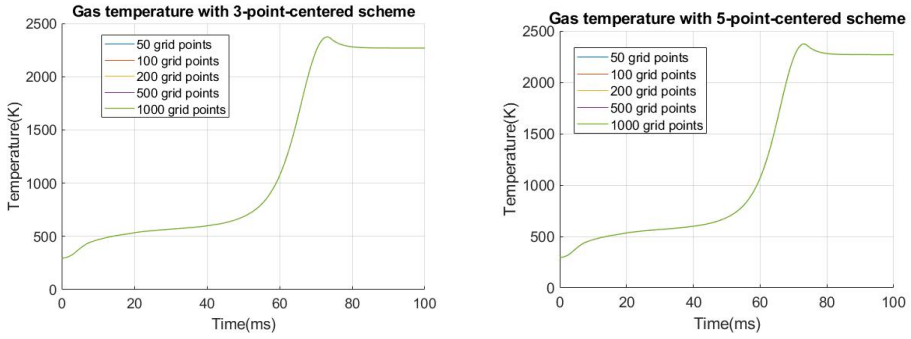

(a) (b)

Figure 5.4: Gas temperature in the sphere with Relative Tolerance=1E-6 and Absolute Tolerance=1E-9, study on grid dependence)

We then tested the performance of the algorithm comparing different schemes and different grids by imposing to the MATLAB ODE solver $ode15s$ Relative Tolerance equal to 1E-3 and Absolute Tolerance equal to 1E-6. Table 5.2 lists the computational times required. We can notice that the use of more complex stencils do not influence the computational time required.

Grid points	**Scheme**	**Computational time (s)**
100	3-point-centered	13.831976
	5-point-centered	14.593603
	7-point-centered	10.603624
	9-point-centered	9.649997
200	3-point-centered	37.635675
	5-point-centered	33.178109
	7-point-centered	30.882259
	9-point-centered	33.128357
500	3-point-centered	661.89405
	5-point-centered	73.2102089
	7-point-centered	76.931104
	9-point-centered	75.410496
1000	3-point-centered	256.424000
	5-point-centered	259.773330
	7-point-centered	245.089124
	9-point-centered	244.271903

Table 5.2: Computational times with Relative Tolerance equal to 1E-3 and Absolute Tolerance equal to 1E-6

It is interested no notice that, despite bringing less spares matrices, the introduction of bigger stencils actually reduces the time required to reach convergence, due to better approximations achieved. Figure 5.5 compares the result for the gas temperature in the bomb. We note that, with the low tolerances imposed, we have slight discrepancies in the solutions, which are not decreased with finer grids.

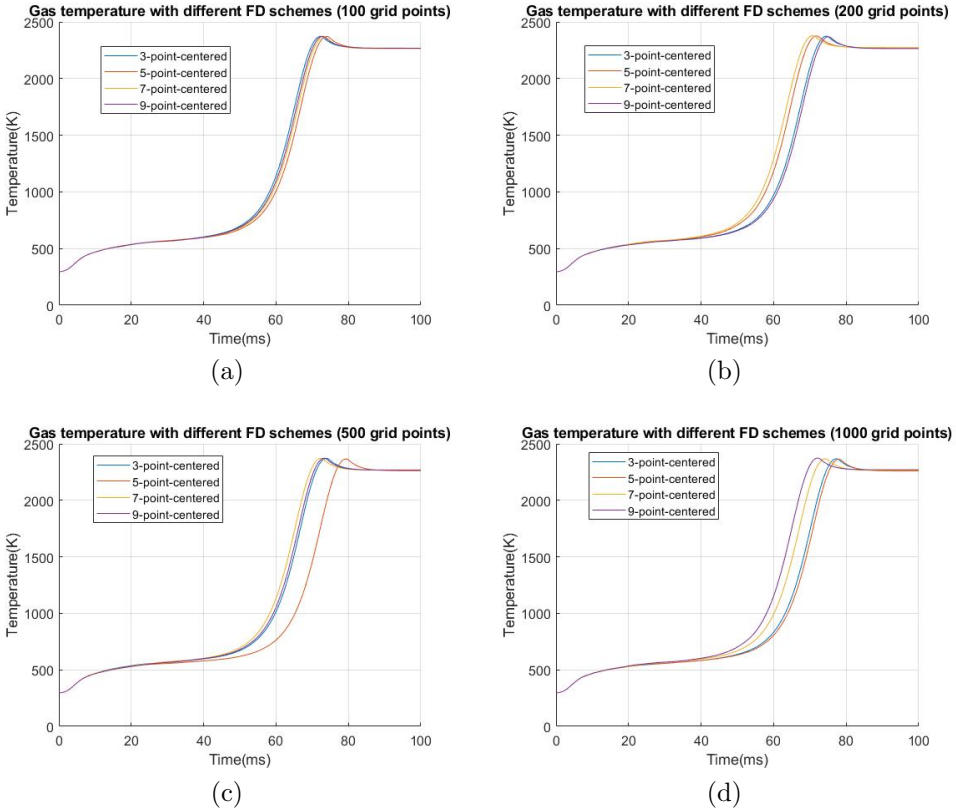

Figure 5.5: With Relative Tolerance=1E-3 and Absolute Tolerance=1E-6)

We tested then with more strict convergence criteria: Relative Tolerance equal to 1E-6 and Absolute Tolerance equal to 1E-9. Table 5.3 lists the computational times.

Grid points	Scheme	Computational time (s)
200	3-point-centered	33.095557
	5-point-centered	37.668125
	7-point-centered	37.998528
	9-point-centered	34.475659
500	3-point-centered	194.973091
	5-point-centered	200.770400
	7-point-centered	182.597067
	9-point-centered	179.109832

Table 5.3: Computational times with Relative Tolerance equal to 1E-6 and Absolute Tolerance equal to 1E-9

Figure 5.6 compares the results for gas temperature solution. We notice that, with decreased tolerances, the curves are overlapped, confirming the stability of the method used.

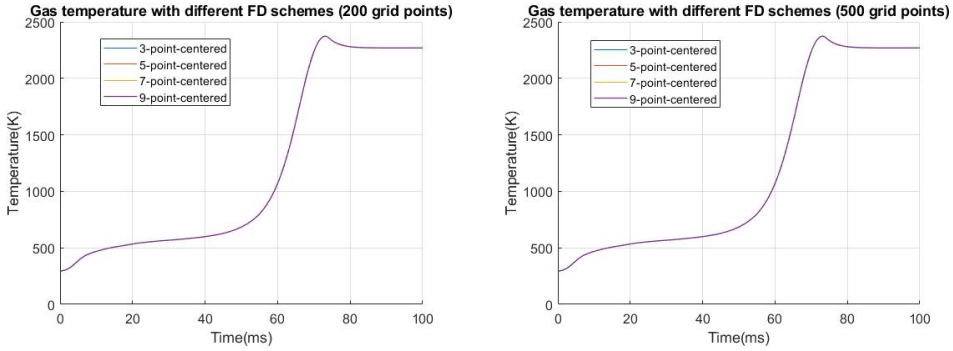

(a) (b)

Figure 5.6: Gas temperature with different schemes and Relative Tolerance=1E-6 and Absolute Tolerance=1E-9)

5.1.2 Aspirin

Figure 5.7 shows the mass loss curve vs temperature which was used to estimate the Aspirin pyrolysis kinetic parameters reported in Table 5.4. The residue at the end of the TG test, β, can be directly viewed observing the

mass loss curve (TG% at 600°C); while, the other pyrolysis kinetic parameters were determined by using the previously described fitting algorithm: particularly, the experimental TG curve was fitted until the occurrence of the maximum rate of weight loss before any inflection point, α, which occurred at 176.70°C.

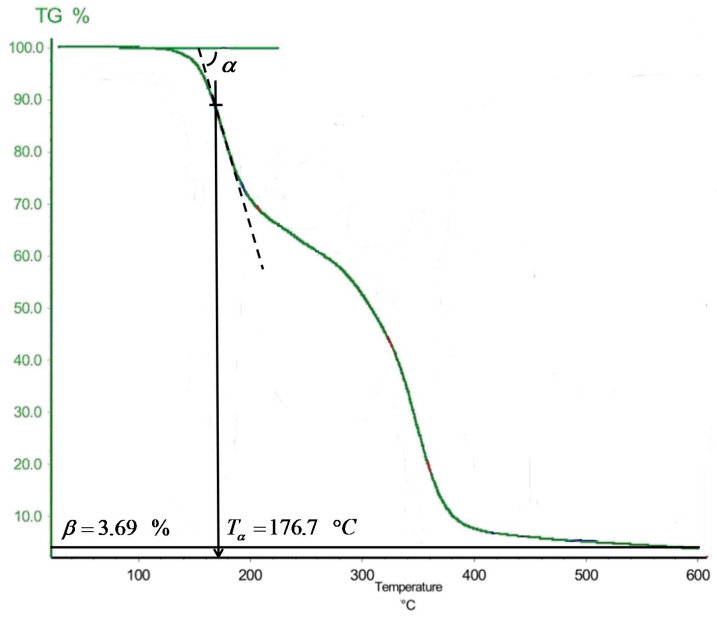

Figure 5.7: TGA for aspirin

Figure 5.8 shows the results of the fitting procedure for Aspirin in terms of comparison between experimental (dotted line) and simulated (using the kinetic parameters listed in Table 5.4) Conversion ζ vs Temperature curve (continuous line). It is worth to notice that the definition of conversion used for the fitting algorithm was the same involved in Eq. 4.32, that is: $\frac{\rho_{\mathbf{S},\mathbf{r},0}-\rho_{\mathbf{S},\mathbf{r}}}{\rho_{\mathbf{S},\mathbf{r},0}}$. As it is possible to notice, the experimental TG curve is perfectly fitted.

Parameter	**Unit**	Value
E_a	$[\frac{J}{mol}]$	1.4225E5
A	$[\frac{1}{s}]$	1.546E11
n	$[-]$	3.09
χ	$[-]$	-0.154
β	$[-]$	0.0369

Table 5.4: Pyrolysis kinetic parameters for Aspirin dust

Finally, Table 5.5 reports all the physical-chemical properties of the aspirin dust searched in the literature which had to be inserted in the predictive model to estimate the value of the k_{ST}. Moreover, it shows the experimental value of the k_{ST} (at a given average diameter of the dust particles) used to validate the model predictions.

In the choice of some parameters to be used it was necessary to introduce some hypothesis as not all of them were present in the literature. As an example, the value of the thermal conductivity which was used it is a standard value for an organic dust. Inserting all these parameters in the mathematical model a k_{ST} value very close to the experimental one was achieved: k_{ST}= 220 $bar\frac{m}{s}$ vs $k_{ST,exp}$= 217 $bar\frac{m}{s}$.

Parameter	**Unit**	Value
MW	$[\frac{g}{mol}]$	180.159
ρ_S	$[\frac{kg}{m^3}]$	1040
$c_{p,\mathbf{S}}$	$[\frac{J}{kgK}]$	893.10
$c_{p,\mathbf{V}}$	$[\frac{J}{kgK}]$	2125
λ	$[\frac{W}{mK}]$	0.165
ΔH_c	$[\frac{J}{kg}]$	2.18E7
ΔH_p	$[\frac{J}{kg}]$	-3.51E5
$k_{ST}\, at\, D_p = 25\mu m$	$[bar\frac{m}{s}]$	213

Table 5.5: Pyrolysis kinetic parameters for Aspirin dust

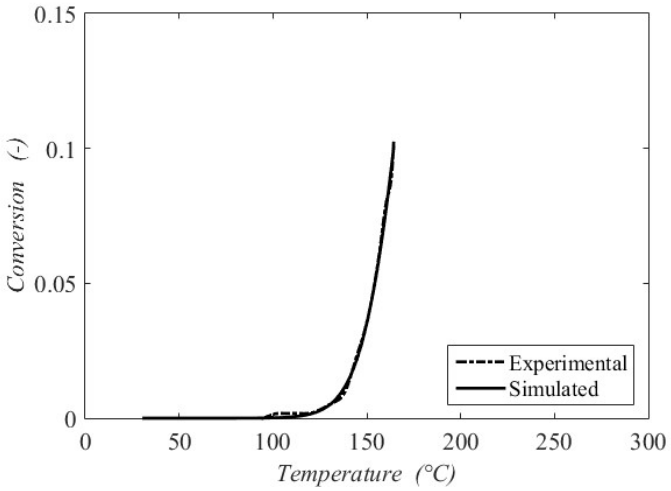

Figure 5.8: Conversion vs. Temperature profile for Aspirin

5.1.3 Cork

As above, Table 5.6 shows the kinetic parameters for the lumped pyrolysis of the cork derived by the fitting of the experimental conversion vs temperature curve (Fig. 5.9). Figure 5.9 also shows the comparison between experimental and simulated (using the estimated kinetic parameters listed in Table 5.6) conversion vs temperature curves. Table 5.7 shows the properties used to simulate the k_{ST} for Cork dust. Inserting all these parameters in the mathematical model a k_{ST} value almost equal to the experimental one was achieved: k_{ST}= 200 $bar\frac{m}{s}$ vs $k_{ST,exp}$= 202 $bar\frac{m}{s}$.

Parameter	**Unit**	Value
E_a	$[\frac{J}{mol}]$	1.114E5
A	$[\frac{1}{s}]$	1.546E11
n	$[-]$	0.862
χ	$[-]$	-0.183
β	$[-]$	0.0487

Table 5.6: Pyrolysis kinetic parameters for Cork dust

Parameter	**Unit**	Value
MW	$[\frac{g}{mol}]$	164.05
ρ_S	$[\frac{kg}{m^3}]$	250
$c_{p,\mathbf{S}}$	$[\frac{J}{kgK}]$	350
$c_{p,\mathbf{V}}$	$[\frac{J}{kgK}]$	1900
λ	$[\frac{W}{mK}]$	0.045
ΔH_c	$[\frac{J}{kg}]$	2.93E7
ΔH_p	$[\frac{J}{kg}]$	-1.52E6
$k_{ST}\, at\, D_p = 42\mu m$	$[bar\frac{m}{s}]$	202

Table 5.7: Pyrolysis kinetic parameters for Cork dust

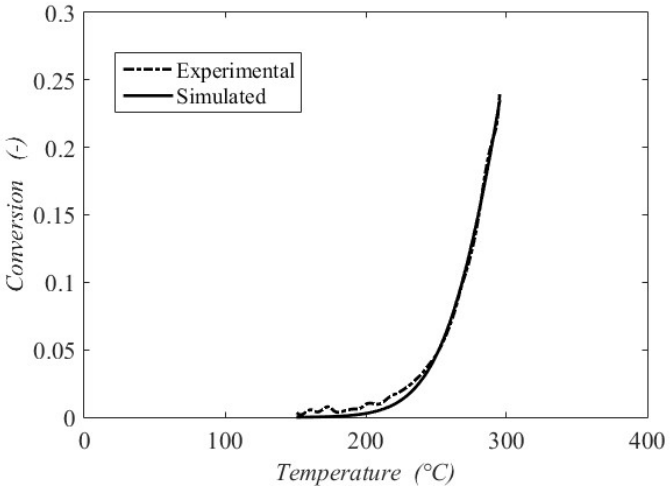

Figure 5.9: Conversion vs. Temperature profile for Cork

5.1.4 Corn starch

Table 5.8 shows the kinetic parameters for the lumped pyrolysis of the cork derived by the fitting of the experimental conversion vs temperature curve (Fig. 5.10). Figure 5.10 also shows the comparison between experimental and simulated (using the estimated kinetic parameters listed in Table 5.8) conversion vs temperature curves. Table 5.9 shows the properties used to simulate the k_{ST} for Corn starch dust. Inserting all these parameters in the

mathematical model a k_{ST} value almost equal to the experimental one was achieved: k_{ST}= 131 $bar\frac{m}{s}$ vs $k_{ST,exp}$= 132 $bar\frac{m}{s}$.

Parameter	**Unit**	Value
E_a	$[\frac{J}{mol}]$	2.220E5
A	$[\frac{1}{s}]$	3.270E9
n	$[-]$	4.54
χ	$[-]$	-0.158
β	$[-]$	0.1101

Table 5.8: Pyrolysis kinetic parameters for Corn starch dust

Parameter	**Unit**	Value
MW	$[\frac{g}{mol}]$	180.156
ρ_S	$[\frac{kg}{m^3}]$	1480
$c_{p,\mathbf{S}}$	$[\frac{J}{kgK}]$	1631
$c_{p,\mathbf{V}}$	$[\frac{J}{kgK}]$	2125
λ	$[\frac{W}{mK}]$	0.167
ΔH_c	$[\frac{J}{kg}]$	1.56E7
ΔH_p	$[\frac{J}{kg}]$	-8.00E5
$k_{ST}\, at\, D_p = 54\mu m$	$[bar\frac{m}{s}]$	132

Table 5.9: Pyrolysis kinetic parameters for Corn starch dust

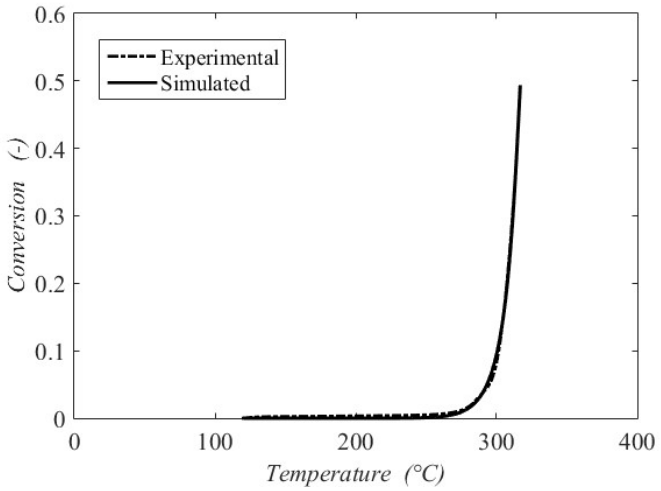

Figure 5.10: Conversion vs. Temperature profile for Corn

5.1.5 Niacin

Table 5.10 shows the kinetic parameters for the lumped pyrolysis of the cork derived by the fitting of the experimental conversion vs temperature curve (Fig. 5.11). Figure 5.11 also shows the comparison between experimental and simulated (using the estimated kinetic parameters listed in Table 5.10) conversion vs temperature curves. Table 5.11 shows the properties used to simulate the k_{ST} for Niacin dust. Inserting all these parameters in the mathematical model a k_{ST} value close to the experimental one was achieved: k_{ST}= 220 $bar\frac{m}{s}$ vs $k_{ST,exp}$= 215 $bar\frac{m}{s}$.

Parameter	**Unit**	Value
E_a	$[\frac{J}{mol}]$	1.328E5
A	$[\frac{1}{s}]$	9.553E14
n	$[-]$	0.94
χ	$[-]$	0.0124
β	$[-]$	9.40E-6

Table 5.10: Pyrolysis kinetic parameters for Niacin dust

Parameter	**Unit**	Value
MW	$[\frac{g}{mol}]$	123.111
ρ_S	$[\frac{kg}{m^3}]$	1162
$c_{p,\mathbf{S}}$	$[\frac{J}{kgK}]$	1243
$c_{p,\mathbf{V}}$	$[\frac{J}{kgK}]$	2125
λ	$[\frac{W}{mK}]$	1
ΔH_c	$[\frac{J}{kg}]$	2.22E7
ΔH_p	$[\frac{J}{kg}]$	-2.02E5
$k_{ST}\, at\, D_p = 37\mu m$	$[bar\frac{m}{s}]$	215

Table 5.11: Pyrolysis kinetic parameters for Niacin dust

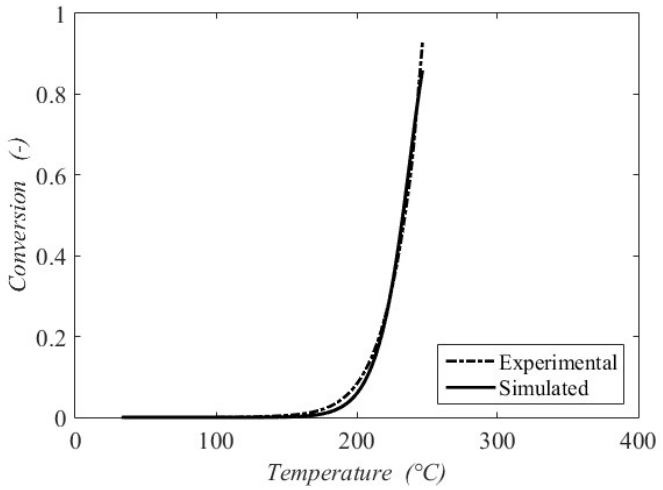

Figure 5.11: Conversion vs. Temperature profile for Niacin

5.1.6 Polyethylene

Table 5.12 shows the kinetic parameters for the lumped pyrolysis of the cork derived by the fitting of the experimental conversion vs temperature curve (Fig. 5.12). Figure 5.12 also shows the comparison between experimental and simulated (using the estimated kinetic parameters listed in Table 5.12) conversion vs temperature curves. Table 5.13 shows the properties used to

simulate the k_{ST} for Niacin dust. Inserting all these parameters in the mathematical model a k_{ST} value close to the experimental one was achieved: k_{ST}= 147 $bar\frac{m}{s}$ vs $k_{ST,exp}$= 133 $bar\frac{m}{s}$. There is only a slight overestimation; anyway, it appears that, the value given by the model is included in the common error bands (15 %). A possible explanation for this deviations between predicted and experimental value of k_{ST} can be found in the extremely variation of the properties of polyethylene, PE (e.g. high or low density).

Parameter	**Unit**	Value
E_a	$[\frac{J}{mol}]$	1.844E5
A	$[\frac{1}{s}]$	6.578E14
n	$[-]$	0.665
χ	$[-]$	0.0887
β	$[-]$	0.0142

Table 5.12: Pyrolysis kinetic parameters for Polyethylene dust

Parameter	**Unit**	Value
MW	$[\frac{g}{mol}]$	28.05
ρ_S	$[\frac{kg}{m^3}]$	920
$c_{p,\mathbf{S}}$	$[\frac{J}{kgK}]$	2300
$c_{p,\mathbf{V}}$	$[\frac{J}{kgK}]$	2500
λ	$[\frac{W}{mK}]$	0.01
ΔH_c	$[\frac{J}{kg}]$	5.03E7
ΔH_p	$[\frac{J}{kg}]$	-9.60E5
$k_{ST}\, at\, D_p = 28\mu m$	$[bar\frac{m}{s}]$	133

Table 5.13: Pyrolysis kinetic parameters for Polyethylene dust

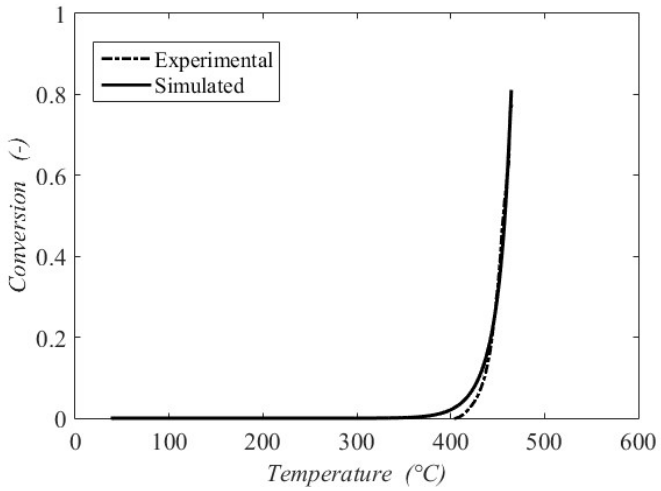

Figure 5.12: Conversion vs. Temperature profile for Polyethylene

5.1.7 Polystyrene

Table 5.14 shows the kinetic parameters for the lumped pyrolysis of the cork derived by the fitting of the experimental conversion vs temperature curve (Fig. 5.13). Figure 5.13 also shows the comparison between experimental and simulated (using the estimated kinetic parameters listed in Table 5.14) conversion vs temperature curves. Table 5.15 shows the properties used to simulate the k_{ST} for Niacin dust. Inserting all these parameters in the mathematical model a k_{ST} value almost equal to the experimental one was achieved: k_{ST}= 216 $bar\frac{m}{s}$ vs $k_{ST,exp}$= 218 $bar\frac{m}{s}$.

Parameter	**Unit**	Value
E_a	$[\frac{J}{mol}]$	1.792E5
A	$[\frac{1}{s}]$	4.228E14
n	$[-]$	0.821
χ	$[-]$	0.124
β	$[-]$	0.0705

Table 5.14: Pyrolysis kinetic parameters for Polystyrene dust

Parameter	**Unit**	Value
MW	$[\frac{g}{mol}]$	104.1491
ρ_S	$[\frac{kg}{m^3}]$	1040
$c_{p,\mathbf{S}}$	$[\frac{J}{kgK}]$	1800
$c_{p,\mathbf{V}}$	$[\frac{J}{kgK}]$	2500
λ	$[\frac{W}{mK}]$	0.02
ΔH_c	$[\frac{J}{kg}]$	4.22E7
ΔH_p	$[\frac{J}{kg}]$	-6.39E5
$k_{ST}\, at\, D_p = 20\mu m$	$[bar\frac{m}{s}]$	218

Table 5.15: Pyrolysis kinetic parameters for Polystyrene dust

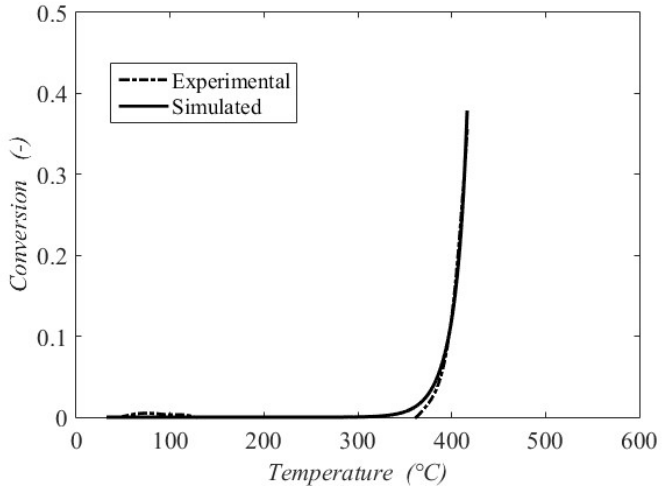

Figure 5.13: Conversion vs. Temperature profile for Polystirene

5.1.8 Sugar

Table 5.16 shows the kinetic parameters for the lumped pyrolysis of the cork derived by the fitting of the experimental conversion vs temperature curve (Fig. 5.14). Figure 5.14 also shows the comparison between experimental and simulated (using the estimated kinetic parameters listed in Table 5.16) conversion vs temperature curves. Table 5.17 shows the properties used to simulate the k_{ST} for Niacin dust. Inserting all these parameters in the

mathematical model a k_{ST} value close to the experimental one was achieved: k_{ST}= 155 $bar\frac{m}{s}$ vs $k_{ST,exp}$= 138 $bar\frac{m}{s}$. There is only a slight overestimation; anyway, it appears that, the value given by the model is included in the common error bands (15 %).

Parameter	**Unit**	Value
E_a	$[\frac{J}{mol}]$	3.574E5
A	$[\frac{1}{s}]$	7.357E14
n	$[-]$	8.16
χ	$[-]$	-0.1112
β	$[-]$	0.207

Table 5.16: Pyrolysis kinetic parameters for Sugar dust

Parameter	**Unit**	Value
MW	$[\frac{g}{mol}]$	342.297
ρ_S	$[\frac{kg}{m^3}]$	1590
$c_{p,\mathbf{S}}$	$[\frac{J}{kgK}]$	1263
$c_{p,\mathbf{V}}$	$[\frac{J}{kgK}]$	2500
λ	$[\frac{W}{mK}]$	0.167
ΔH_c	$[\frac{J}{kg}]$	8.18E6
ΔH_p	$[\frac{J}{kg}]$	-4.00E5
$k_{ST}\, at\, D_p = 30\mu m$	$[bar\frac{m}{s}]$	138

Table 5.17: Pyrolysis kinetic parameters for Sugar dust

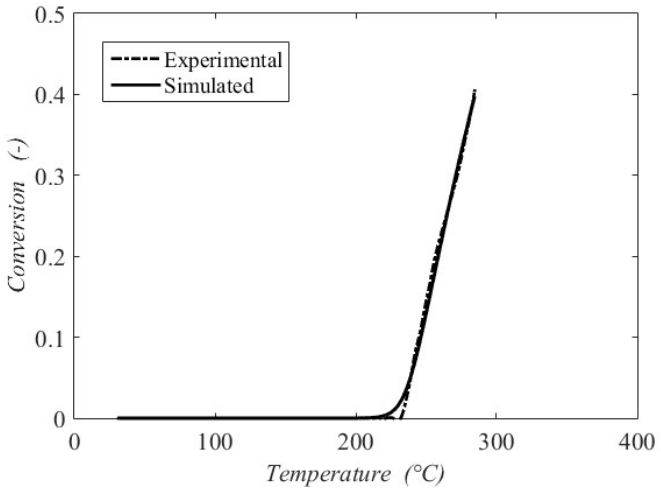

Figure 5.14: Conversion vs. Temperature profile for Sugar

5.1.9 Wheat flour

Table 5.18 shows the kinetic parameters for the lumped pyrolysis of the cork derived by the fitting of the experimental conversion vs temperature curve (Fig. 5.15). Figure 5.15 also shows the comparison between experimental and simulated (using the estimated kinetic parameters listed in Table 5.18) conversion vs temperature curves. Table 5.19 shows the properties used to simulate the k_{ST} for Niacin dust. Inserting all these parameters in the mathematical model a k_{ST} value almost equal to the experimental one was achieved: k_{ST}= 63 $bar\frac{m}{s}$ vs $k_{ST,exp}$= 62 $bar\frac{m}{s}$.

Parameter	**Unit**	Value
E_a	$[\frac{J}{mol}]$	1.861E5
A	$[\frac{1}{s}]$	4.012E14
n	$[-]$	1.867
χ	$[-]$	0.236
β	$[-]$	0.1101

Table 5.18: Pyrolysis kinetic parameters for Wheat flour dust

Parameter	**Unit**	Value
MW	$[\frac{g}{mol}]$	120.1
ρ_S	$[\frac{kg}{m^3}]$	527
$c_{p,\mathbf{S}}$	$[\frac{J}{kgK}]$	2500
$c_{p,\mathbf{V}}$	$[\frac{J}{kgK}]$	2500
λ	$[\frac{W}{mK}]$	0.075
ΔH_c	$[\frac{J}{kg}]$	1.83E7
ΔH_p	$[\frac{J}{kg}]$	-8.00E5
$k_{ST}\, at\, D_p = 57\mu m$	$[bar\frac{m}{s}]$	62

Table 5.19: Pyrolysis kinetic parameters for Wheat flour dust

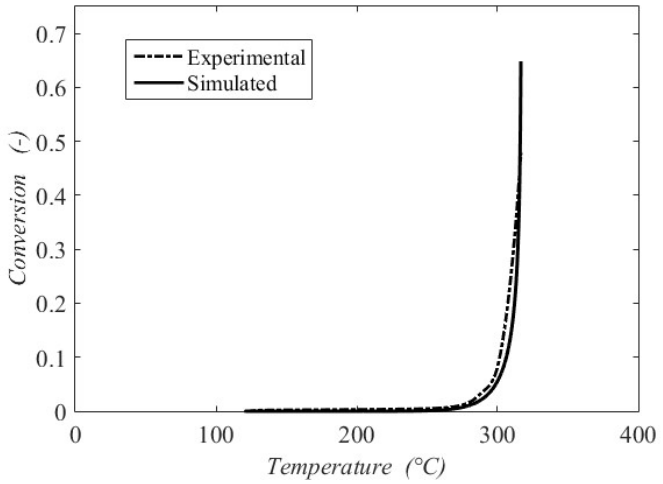

Figure 5.15: Conversion vs. Temperature profile for Wheat flour

5.1.10 Parity plots

In Fig. 5.16, all the experimental and simulated values of k_{ST} are reported. From this parity plot it is possible to see that all the model predicted deflagration indexes are always in the accepted range (note that the accepted error bar are assigned according to the range of k_{ST} value: e.g., when the k_{ST} is over 200 $bar\frac{m}{s}$, the corresponding error bar will be 20%; when it comprised between 100 and 200 $bar\frac{m}{s}$, it will be 15%; and, finally, when it is

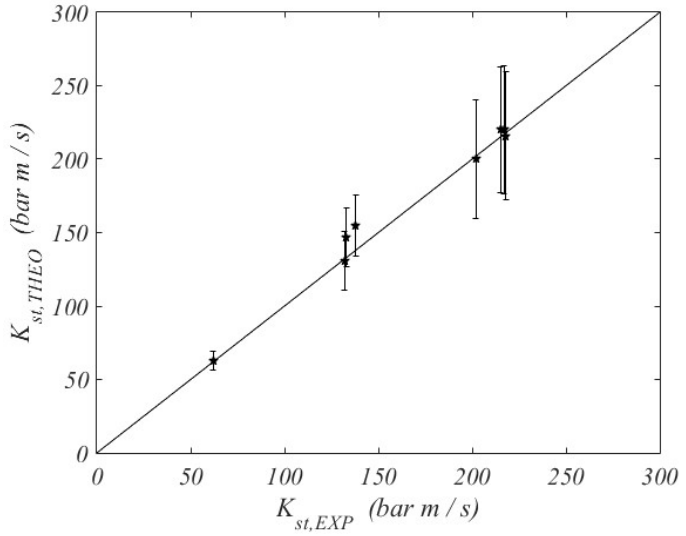

Figure 5.16: Comparison among Theoretical and Experimental values of k_{ST}

lower than 100 $bar\frac{m}{s}$, it will be 10%), therefore confirming the reliability of the developed model.

5.2 Plug Flow Reactor simulation

We report the system of PDEs characterizing the model with constant jacket inlet temperature.

$$\begin{cases} \dfrac{\partial \chi}{\partial \tau} = \delta \dfrac{\partial^2 \chi}{\partial z^2} - \dfrac{\partial \chi}{\partial z} + Da \cdot exp\left(\dfrac{\theta}{1+\dfrac{\theta}{\gamma}}\right) \cdot (1-\chi) \\ \dfrac{\partial \theta}{\partial \tau} = \lambda \dfrac{\partial^2 \theta}{\partial z^2} - \dfrac{\partial \theta}{\partial z} + B \cdot Da \cdot exp\left(\dfrac{\theta}{1+\dfrac{\theta}{\gamma}}\right) \cdot (1-\chi) - St(\theta - \theta_w) \\ \dfrac{\partial \theta_w}{\partial \tau} = -\dfrac{\partial \theta_w}{\partial z} - St_c(\theta - \theta_w) - St_e(\theta_w - \theta_{env}) \end{cases} \tag{5.10}$$

With the following ICs and BCs:

$$\begin{cases} I.C.s & \chi(\tau=0,z)=0 \\ & \theta(\tau=0,z)=0 \\ & \theta_w(\tau=0,z)=0 \\ B.C.s & \chi(\tau,z=0)=0 \\ & \left.\dfrac{\partial\chi}{\partial z}\right|_{z=1}=0 \\ & \theta(\tau,z=0)=0 \\ & \left.\dfrac{\partial\theta}{\partial z}\right|_{z=1}=0 \\ & \theta_w(\tau,z=0)=0 \end{cases} \tag{5.11}$$

If a PI control logic we have instead:

$$\begin{cases} I.C.s & \chi(\tau=0,z)=0 \\ & \theta(\tau=0,z)=0 \\ & \theta_w(\tau=0,z)=0 \\ B.C.s & \chi(\tau,z=0)=0 \\ & \left.\dfrac{\partial\chi}{\partial z}\right|_{z=1}=0 \\ & \theta(\tau,z=0)=0 \\ & \left.\dfrac{\partial\theta}{\partial z}\right|_{z=1}=0 \\ & \left.\dfrac{\partial\theta_w}{\partial\tau}\right|_{z=0}=K_p\left[\left.\dfrac{\partial\theta}{\partial\tau}\right|_{z=z_c}-\dfrac{1}{\tau_i}(\theta_{sp}-\theta(t,z=z_c))\right] \end{cases} \tag{5.12}$$

Among all the models presented, this is the most complicated version. Hence, the implementation of the MOL for the other systems is straightforward. We will consider again a grid of $m+1$ points.

In this case we a system of 2 second-order PDEs and a first order PDE. The mass matrix approach is always a good option for the implementation of MOL. So we want again to express the problem in this form:

$$\boldsymbol{M}\cdot\begin{bmatrix}\boldsymbol{\chi}\\ \boldsymbol{\theta}\\ \boldsymbol{\theta_w}\end{bmatrix}_t=\boldsymbol{A}\cdot\begin{bmatrix}\boldsymbol{\chi}\\ \boldsymbol{\theta}\\ \boldsymbol{\theta_w}\end{bmatrix}+f(\boldsymbol{\chi},\boldsymbol{\theta},\boldsymbol{\theta_w}) \tag{5.13}$$

Where:

$\boldsymbol{\chi}, \boldsymbol{\theta}, \boldsymbol{\theta_w}$ Indicate the vectors defined on the grid points $(\chi_0, \chi_1 ... \chi_m)$ and so on

$\boldsymbol{A}$ Is a block matrix that contains all the discretization matrices

f Collects all the additional terms inside the equations

The mass matrix $\boldsymbol{M}$ is a $(3m+6 \times 3m+6)$ diagonal matrix, and it follows the following pattern:

$$\begin{cases} M_{i,j} = 0 & i \neq j \\ M_{i,i} = 0 & i = 0, m+1, m+2, 2(m+1)+1 \\ M_{i,i} = 1 & elsewhere \end{cases} \tag{5.14}$$

The 0 correspond to the BCs of the 3 PDEs. The matrix $\mathbf{A}$ is a block matrix. If we call again D_1 and D_2 the discretization matrices for the first and second derivatives, and we consider a uniform grid of step Δx, we have then:

$$\boldsymbol{A} = \frac{1}{\Delta x} \begin{bmatrix} \boldsymbol{A}_{1,1} & & \\ & \boldsymbol{A}_{2,2} & \\ & & \boldsymbol{A}_{3,3} \end{bmatrix} \tag{5.15}$$

Where:

$$\mathbf{A}_{1,1} = [\delta D_2 - \Delta x D_1] \tag{5.16}$$

$$\mathbf{A}_{2,2} = [\lambda D_2 - \Delta x D_1] \tag{5.17}$$

$$\mathbf{A}_{3,3} = [-\Delta x D_1] \tag{5.18}$$

For the time integration, we still chose the $MATLAB$ solver $ode15s$, due to its ability to solve DAEs and stiff problems.

5.2.1 Numerical experiments

In this part we tested the efficiency of the proposed method in computing the solution. We chose as test model the PFR with constant inlet temperature jacket. We analyzed how different grids, grid dependence, and different stencils impact the computational time and the solution.

Uniform grids

First, we tested the grid dependence of the solution in uniform grids. We chose a 2-point upwind for the first derivative and a 3-point centered for the second derivative. Table 5.20 lists the computational times required with finer grids, comparing standard conditions with runaway ones (for the other variables we have T_{IN}=625 K, v_0=0,5 $\frac{m}{s}$, T_w= 625 K). As convergence criterion, we have Relative Tolerance equal to 1E-6 and Absolute Tolerance equal to 1E-9.

P_{IN} $[kPa]$	**Grid points**	**Time (s)**
1.6	50	0.965544
	100	1.674512
	200	4.182545
	300	17.215559
	400	18.856277
1.85	50	1.109272
	100	4.172776
	200	29.761084
	300	53.671315
	400	91.819817

Table 5.20: Computational times with Relative Tolerance equal to 1E-6 and Absolute Tolerance equal to 1E-9, testing grid dependence

From the results we notice how the implementation of more critical conditions (higher inlet pressures), consistently increases the time required to reach convergence. We know that this is due to the high exothermicity exhibited around the hotspot. Hence, it would be useful for the computation of the solution introducing non-uniform grids, with a refinement in the first part of reactor.

Figure 5.17 shows the temperature profiles along the length of reactor and jacket at the final time (we made run the algorithm for 5 residence times, in order to reach the steady state). We notice grid dependence for grids below 200 points. The solutions on finer grids are overlapped. Hence, we recommend to choose at least 200 grid points for the computation of the solution.

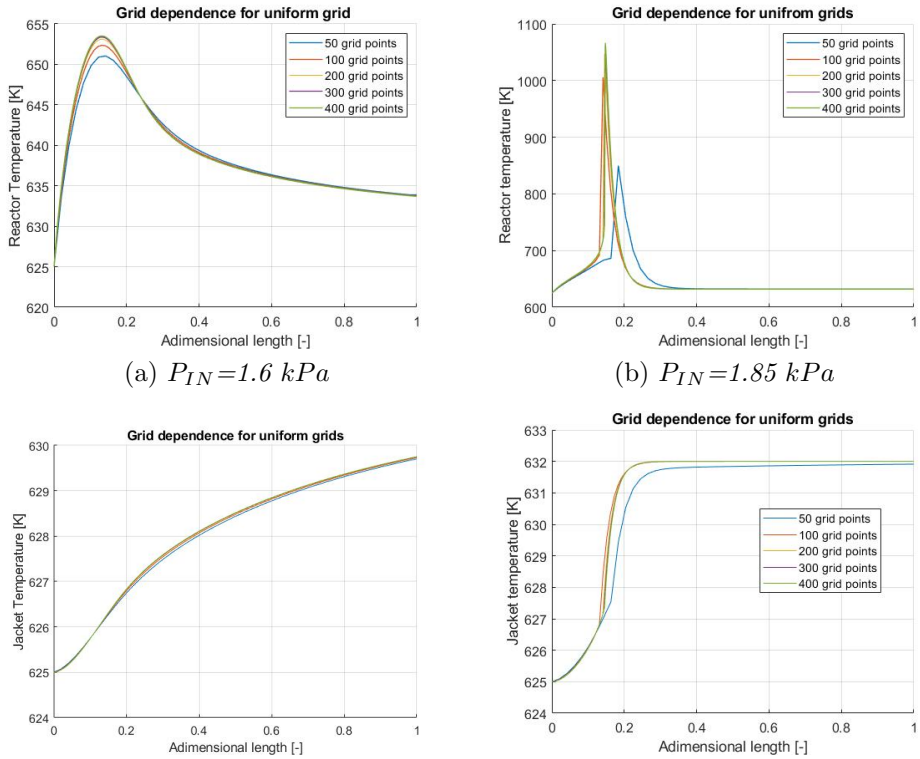

(a) P_{IN}=*1.6 kPa* (b) P_{IN}=*1.85 kPa*

(c) P_{IN}=*1.6 kPa* (d) P_{IN}=*1.85 kPa*

Figure 5.17: Study of grid dependence for reactor and jacket temperature at final time with Relative Tolerance=1E-6 and Absolute Tolerance=1E-9. T_{IN}=625 K, v_0=0,5 $\frac{m}{s}$, $v_{0,cool}$=0,3 $\frac{m}{s}$)

We also tested different schemes for first and second derivatives. Table 5.21 list the computational times for different schemes applied on a 250 points grid. Like in the previous Section, we not that using greater stencils do not necessarily affects the computational times, that are pretty similar.

P_{IN} $[kPa]$	D_1 **scheme**	D_2 **scheme**	**Time (s)**
1.6	2-point-upwind	3-point-centered	5.669915
	3-point-upwind	5-point-centered	11.207451
	4-point-biased-upwind	5-point-centered	4.844773
1.85	2-point-upwind	3-point-centered	41.784848
	3-point-upwind	5-point-centered	50.936067
	4-point-biased-upwind	5-point-centered	51.12548

Table 5.21: Computational times with Relative Tolerance equal to 1E-6 and Absolute Tolerance equal to 1E-9, 250 grid points

For the convergence of different stencils, Fig. 5.18 compare the reactor and jacket temperature profile after 5 residence times inside the reactor. We can notice that solutions are overlapped, confirming the ability of all the proposed schemes to perform the numerical solution of the PDEs system, even in critical conditions.

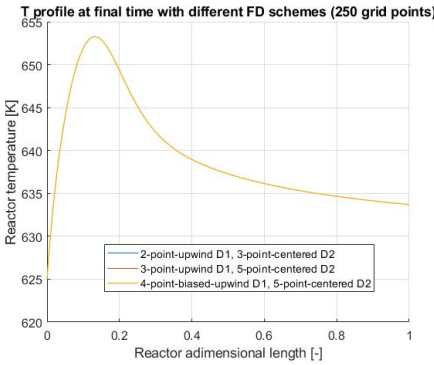

(a) P_{IN}=1.6 kPa

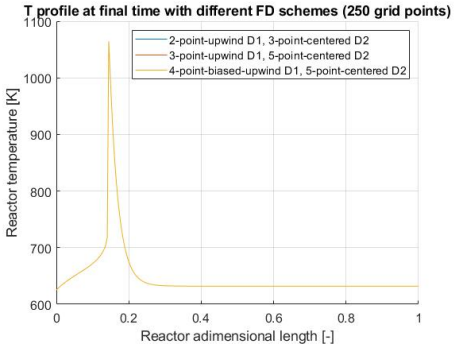

(b) P_{IN}=1.85 kPa

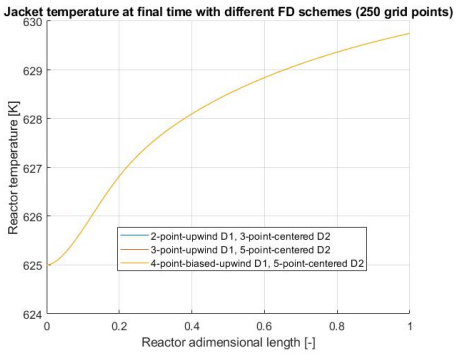

(c) P_{IN}=1.6 kPa

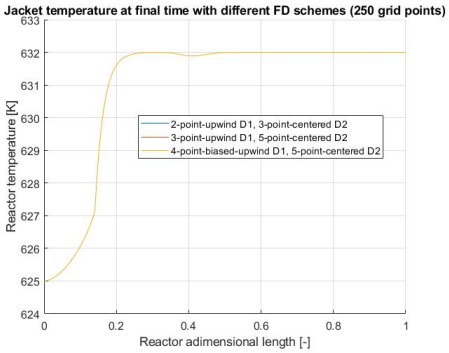

(d) P_{IN}=1.85 kPa

Figure 5.18: Reactor and jacket temperature at final time with different schemes and Relative Tolerance=1E-6 and Absolute Tolerance=1E-9.T_{IN}=625 K, v_0=0,5 $\frac{m}{s}$, $v_{0,cool}$=0,3 $\frac{m}{s}$)

Non-uniform grids

It is then worth introducing non-uniform grids for the solution of the problem, since the presence of the hotspot causes the solution to be extremely sharp at a specific point of the domain. We tried different grid structures and compared them. We apply a 2-point-upwind scheme for the first derivative, and a 3-point-centered scheme for the second derivative. We tested a Chebyshev Polynomial, leading to the following structure:

$$z_i = \frac{1}{2} + \frac{1}{2}\cos\left(\frac{(2i+1)\cdot\pi}{2(m+2)}\right) \tag{5.19}$$

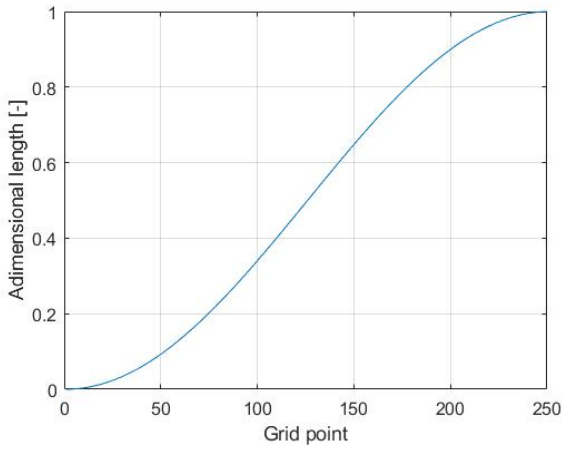

Figure 5.19: Distribution of grid points with a Chebyshev polynomial

The structure of the grid is represented in Fig. 5.19 shows the location of the grid points. It is notable that we have a refinement at the first part of the reactor, where the exothermicity is supposed to happen We also tested a manually refined grid, by composing the grid of 2 separated uniform grids, with the first half of the domain containing more points (150 vs 100). Table 5.22 shows the computational times required by the different schemes:

P_{IN} $[kPa]$	**Grid type**	**Time (s)**
1.6	Uniform	5.669915
	Chebyshev	4.598151
	Manually refined	5.215662
1.85	Uniform	30.412585
	Chebyshev	20.198348
	Manually refined	25.5441

Table 5.22: Computational times for different grids, with Relative Tolerance equal to 1E-6 and Absolute Tolerance equal to 1E-9, 250 grid points

We can notice that, the Chebyshev polynomial brings to significant improvements in the computational time, especially under critic conditions. Figure 5.20 compares the result after 5 residence times. We see that the solutions are overlapped, confirming the convergence of all proposed schemes.

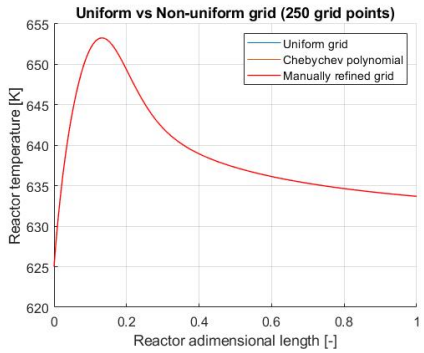

(a) P_{IN}=1.6 kPa

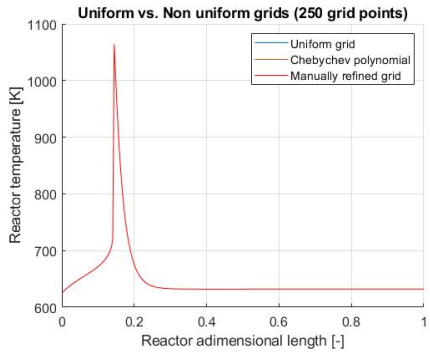

(b) P_{IN}=1.85 kPa

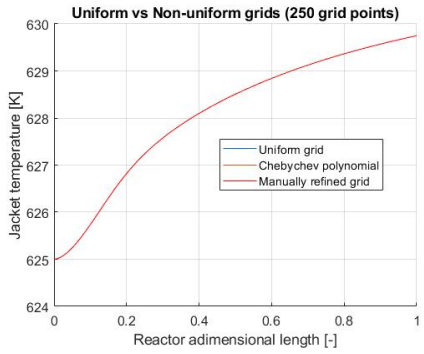

(c) P_{IN}=1.6 kPa

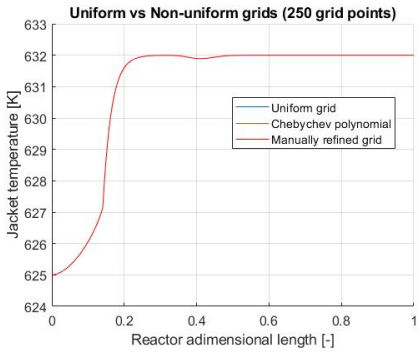

(d) P_{IN}=1.85 kPa

Figure 5.20: Reactor and jacket temperature at final time with different grids, Relative Tolerance=1E-6 and Absolute Tolerance=1E-9.T_{IN}=625 K, v_0=0,5 $\frac{m}{s}$, $v_{0,cool}$=0,3 $\frac{m}{s}$)

Now that we analyzed different set-ups for the resolution of the proposed system, we can swap to the study of the proposed models and their sensitivity analysis.

5.2.2 Steady state model

At first, in order to have reliable comparisons between results, we simulated the PFR without diffusion under steady-state conditions, with a constant jacket temperature (these hypotheses are the same as Morbidelli and Varma [37], their results are presented in Fig. 5.21). In this case the final system is

a couple of ODEs, and they appear in this form:

$$\begin{cases} \dfrac{\partial \chi}{\partial z} - Da \cdot exp\left(\dfrac{\theta}{1+\dfrac{\theta}{\gamma}}\right) \cdot (1-\chi) \\ \dfrac{\partial \theta}{\partial z} = B \cdot Da \cdot exp\left(\dfrac{\theta}{1+\dfrac{\theta}{\gamma}}\right) \cdot (1-\chi) - St(\theta - \theta_w) \end{cases} \tag{5.20}$$

With the following BCs:

$$\begin{cases} B.C.s & \chi(z=0) = 0 \\ & \theta(z=0) = 0 \end{cases} \tag{5.21}$$

We report the solution of the equations under standard conditions and runaway conditions.

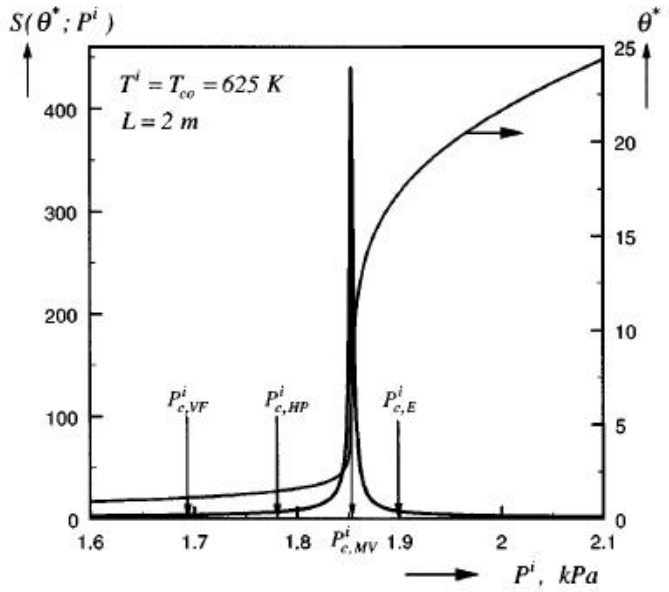

Figure 5.21: Temperature and Sensitivity analysis with respect to the inlet pressure (Varma and Morbidelli, 1999)

Solution with different ICs

Under standard conditions (for simplicity we will call the inlet pressure of Napthalene P_{IN}) (P_{IN}=1.6 kPa, T_{IN}=625 K, v_0=0,5 $\frac{m}{s}$, T_w= 625 K), we see the evolution of conversion and temperature along the reactor in Fig. 5.22. The hotspot of the reactor is located at z=0.18, with a peak of temperature equal to 652 K.

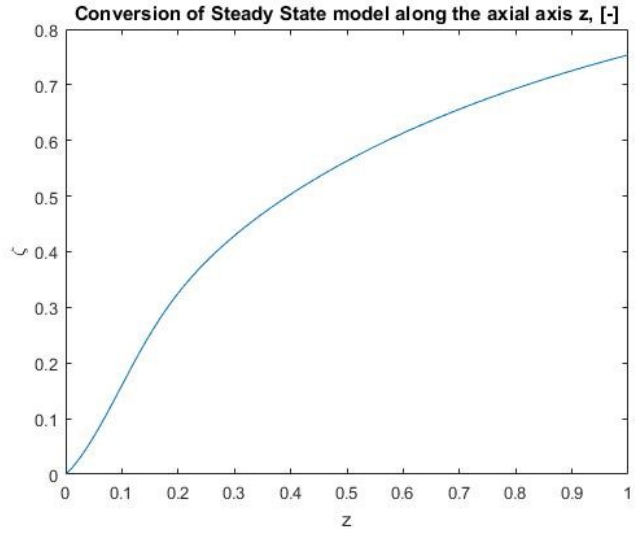

(a) *Conversion*

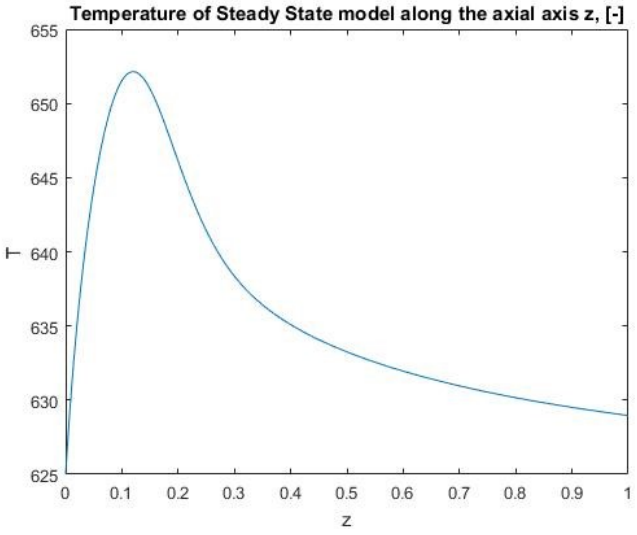

(b) *Temperature*

Figure 5.22: Evolution of conversion and temperature along the reactor with P_{IN}=1.6 kPa, T_{IN}=625 K, v_0=0,5 $\frac{m}{s}$, T_w= 625 K

In order to show the concept of parametric sensitivity, we perform now the same simulation increasing the inlet Naphthalene pressure (that is, increased reactant concentration). We set P_{IN}=1.85 kPa, T_{in}=625 K, v_0=0,5 $\frac{m}{s}$, T_w=

625 K. Basically, we increased the inlet pressure of about 15%. Fig. 5.23 shows the results.

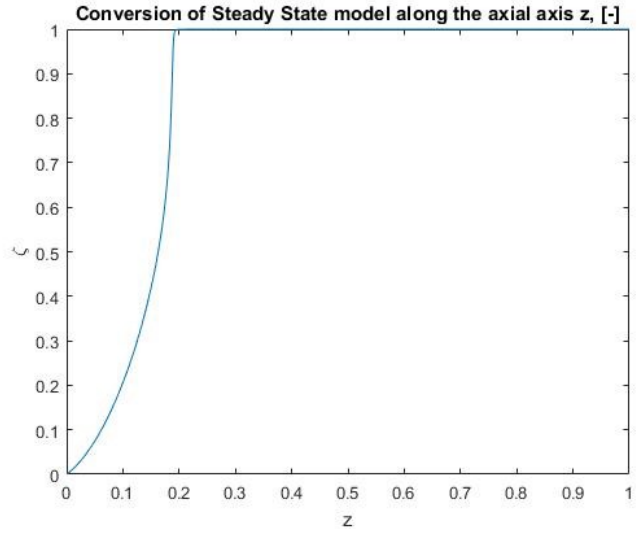

(a) *Conversion*

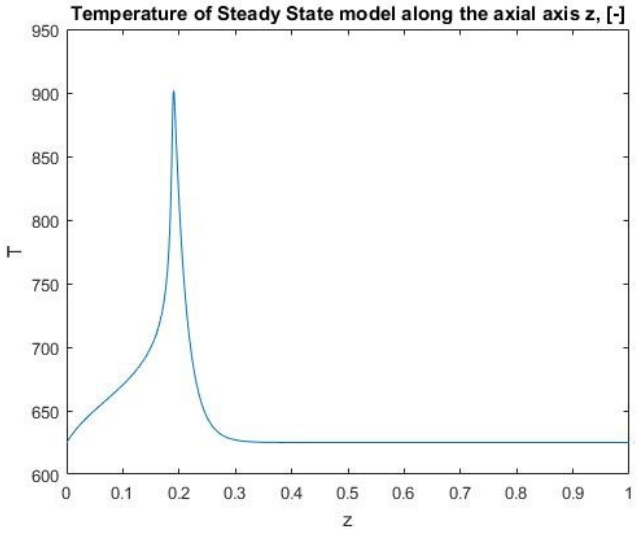

(b) *Temperature*

Figure 5.23: Evolution of conversion and temperature along the reactor with P_{IN}=1.85 kPa, T_{IN}=625 K, v_0=0,5 $\frac{m}{s}$

In this case, we see that the hotspot is slight shifted to the right (z=0.2),

but the temperature of the reactor increased until 905 K, that is around 50% more than the previous result. This indicates that the system is sensitive if we slightly modify the inlet pressure around the value of 1.85 kPa. This is due to the reaction term, that is highly enhanced by the increased reactant concentration.

Runaway Boundaries

In this sense, we applied the parametric sensitivity (discussed in Section 2.2) to the steady state model, in order to establish under which parameters the PFR exhibits sensitive behavior.

We performed a sensitivity analysis with respect to inlet pressure, with different fluid velocities.

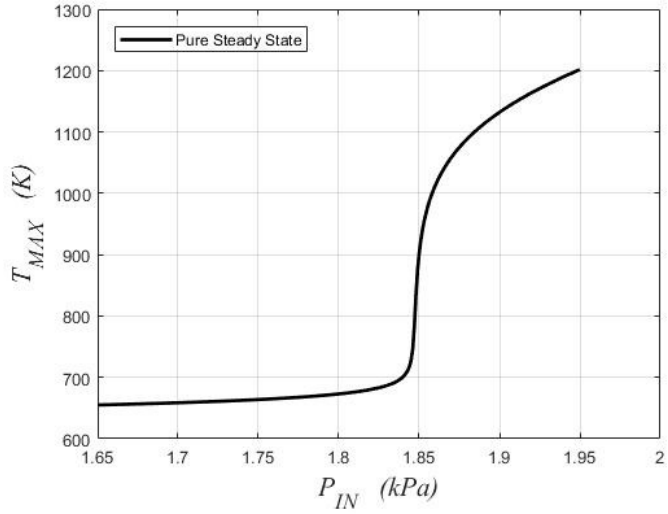

(a) *Maximum temperature in the reactor as a function of the inlet pressure*

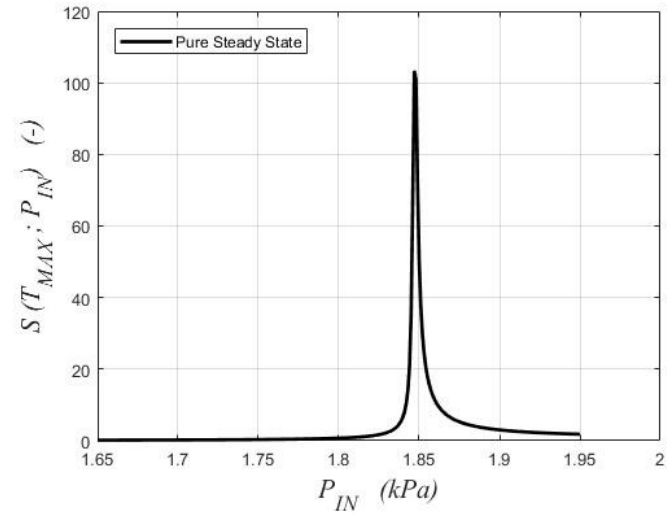

(b) *Sensitivity function S as a function of the inlet pressure*

Figure 5.24: Temperature and Sensitivity analysis with respect to the inlet pressure, for the steady state model

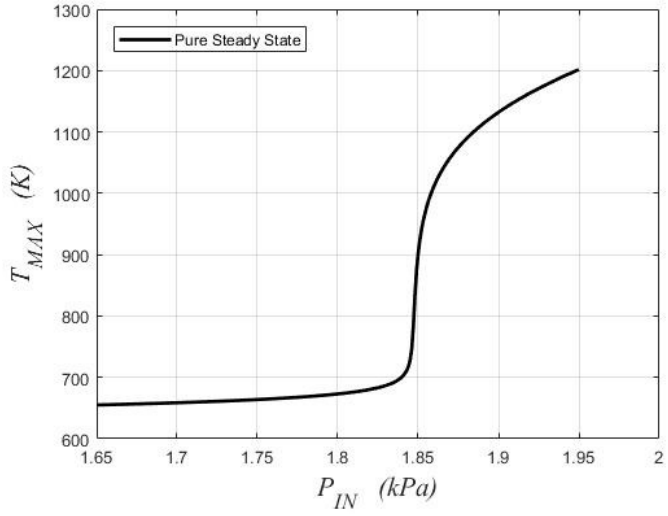

(a) *Maximum temperature in the reactor as a function of the inlet pressure*

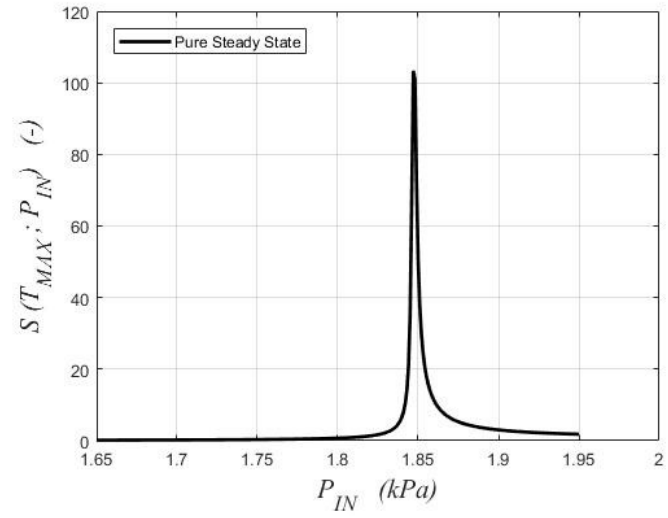

(b) *Sensitivity function S as a function of the inlet pressure*

Figure 5.25: Maximum temperature and Sensitivity respect to different values of P_{IN}, with T_{IN}=625 K, v_0=1 $\frac{m}{s}$, steady state model.

Figure 5.24 shows the results with an inlet velocity equal to 0.5 $\frac{m}{s}$, while Fig. 5.25 shows the results for v_0=1 $\frac{m}{s}$. The critical value of inlet pressure is 1.85 kPa and the critical value for the inlet temperature is 661 K, found

changing the inlet velocity in the range between 0.1-2.0 $\frac{m}{s}$. It can be noticed that these values coincide with those ones computed by Morbidelli and Varma [37], illustrated in Fig. 5.21.

5.2.3 Unsteady state model, constant temperature jacket

We study then the unsteady state model, assuming a constant temperature jacket. The set of equations is then:

$$\begin{cases} \dfrac{\partial \chi}{\partial \tau} = \delta \dfrac{\partial^2 \chi}{\partial z^2} - \dfrac{\partial \chi}{\partial z} + Da \cdot exp\left(\dfrac{\theta}{1+\dfrac{\theta}{\gamma}}\right) \cdot (1-\chi) \\ \dfrac{\partial \theta}{\partial \tau} = \lambda \dfrac{\partial^2 \theta}{\partial z^2} - \dfrac{\partial \theta}{\partial z} + B \cdot Da \cdot exp\left(\dfrac{\theta}{1+\dfrac{\theta}{\gamma}}\right) \cdot (1-\chi) - St(\theta - \theta_w) \end{cases} \tag{5.22}$$

With the following ICs and BCs:

$$\begin{cases} I.C.s & \chi(\tau = 0, z) = 0 \\ & \theta(\tau = 0, z) = 0 \\ B.C.s & \chi(\tau, z = 0) = 0 \\ & \left.\dfrac{\partial \chi}{\partial z}\right|_{z=1} = 0 \\ & \theta(\tau, z = 0) = 0 \\ & \left.\dfrac{\partial \theta}{\partial z}\right|_{z=1} = 0 \end{cases} \tag{5.23}$$

For the computation of results, we used a non-uniform grid (following the Chebyshev polynomial), and 2-point-upwind scheme for the first derivative and 3-point-centered for the second derivative.

Solution with different ICs

Under standard conditions, hence P_{IN}=1.6 kPa, T_{IN}=625 K, v_0=0,5 $\frac{m}{s}$, T_w= 625 K, we see the evolution of conversion and temperature along the

reactor in Fig. 5.26. The hotspot of the reactor is slightly shifted to the left, at z=0.15, with a peak of temperature equal to 652 K.

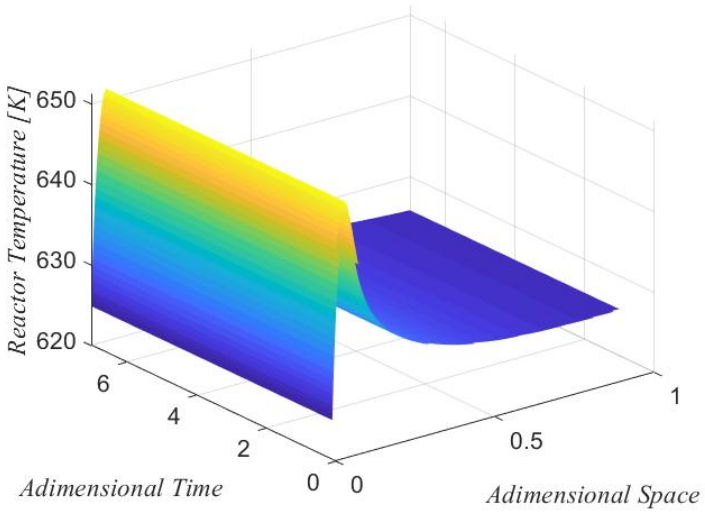

Figure 5.26: Evolution of conversion and temperature along the reactor with P_{IN}=1.6 kPa, T_{IN}=625 K, v_0=0,5 $\frac{m}{s}$, T_w= 625 K

We tested than under critical conditions (P_{IN}=1.85 kPa). The temperature profile is shown in Fig. 5.27.

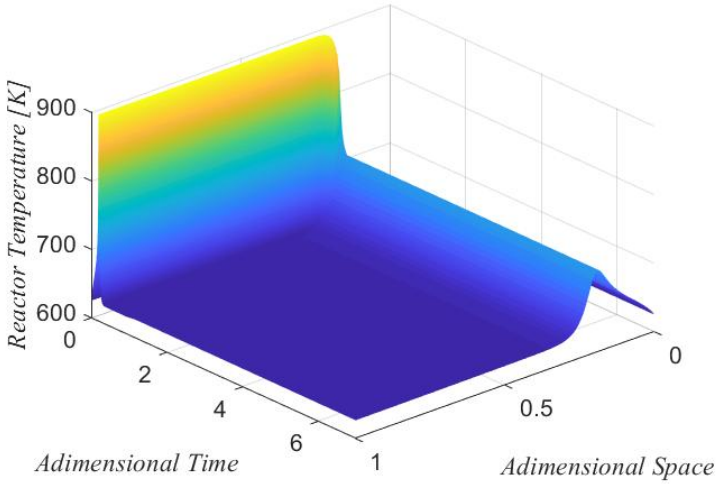

Figure 5.27: Evolution of conversion and temperature along the reactor with P_{IN}=1.85 kPa, T_{IN}=625 K, v_0=0,5 $\frac{m}{s}$, T_w= 625 K

We notice that the maximum temperature is reached during the reactor transient, and it is equal to 902.15 K. Hence, it is almost equal to the steady state case, remarking a moderate impact of the unsteady state and diffusion on the system.

Runaway Boundaries

Even in this case, we perform the sensitivity analysis, respect to both inlet pressure and temperature. We compare the resulting diagrams with the steady state model ones. Figure 5.28 shows the maximum temperature and the sensitivity with respect to the inlet pressure of Napthalene.

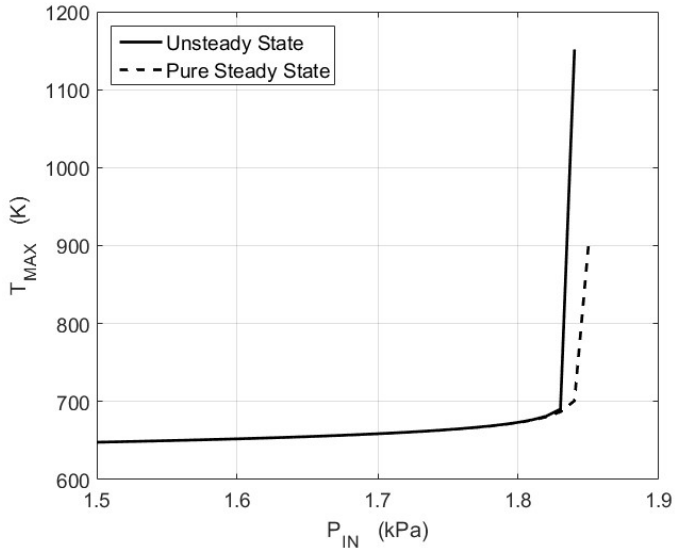

(a) *Maximum temperature in the reactor as a function of the inlet pressure*

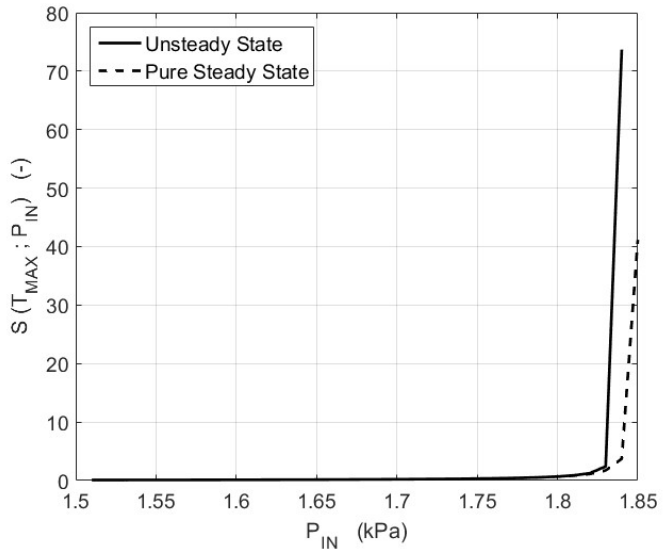

(b) *Sensitivity function S as a function of the inlet pressure*

Figure 5.28: Maximum temperature and Sensitivity respect to different values of P_{IN}, with T_{IN}=625 K, v_0=1 $\frac{m}{s}$, unsteady state model with constant jacket temperature.

Figure 5.29 shows the same analysis, with respect of the inlet temperature.

The critical value of inlet pressure is 1.84 kPa, with a negligible difference with respect to the steady state case. The critical value of inlet temperature is 657 K, with a slight difference with respect to the steady state case.

There are small differences between these values and the ones computed with the steady state model. Of course, such differences are not significant from an operative point of view, therefore can be disregarded concluding that the runaway boundary predicted by both models is the same.

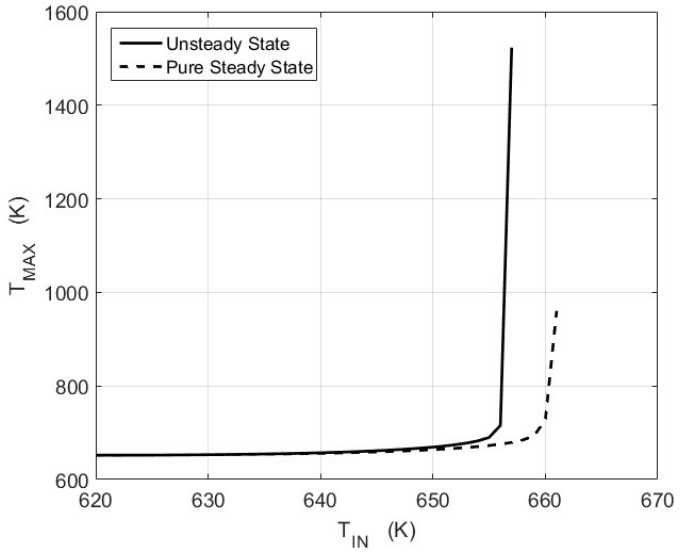

(a) *Maximum temperature in the reactor as a function of the inlet temperature*

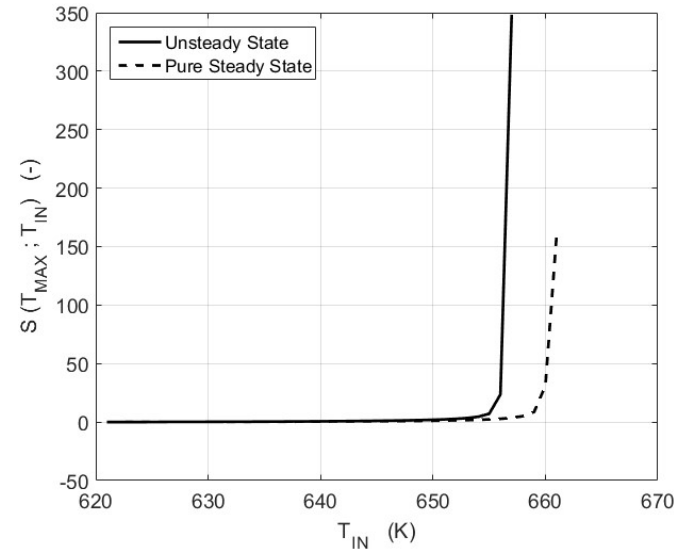

(b) *Sensitivity function S as a function of the inlet temperature*

Figure 5.29: Maximum temperature and Sensitivity respect to different values of T_{IN}, with P_{IN}=1.6 kPa, v_0=1 $\frac{m}{s}$, unsteady state model with constant jacket temperature.

5.2.4 Unsteady state model, constant inlet temperature jacket

Now we consider a more realistic case, where the jacket actually dynamically interacts with the reactor. Hence, the jacket temperature profile is not constant anymore. In this case we won't consider the presence of a temperature controller. Hence, the jacket has a constant inlet temperature. The set of equations is the following:

$$\begin{cases} \dfrac{\partial \chi}{\partial \tau} = \delta \dfrac{\partial^2 \chi}{\partial z^2} - \dfrac{\partial \chi}{\partial z} + Da \cdot exp\left(\dfrac{\theta}{1+\dfrac{\theta}{\gamma}}\right) \cdot (1-\chi) \\ \dfrac{\partial \theta}{\partial \tau} = \lambda \dfrac{\partial^2 \theta}{\partial z^2} - \dfrac{\partial \theta}{\partial z} + B \cdot Da \cdot exp\left(\dfrac{\theta}{1+\dfrac{\theta}{\gamma}}\right) \cdot (1-\chi) - St(\theta - \theta_w) \\ \dfrac{\partial \theta_w}{\partial \tau} = -\dfrac{\partial \theta_w}{\partial z} - St(\theta - \theta_w) - St_e(\theta_w - \theta_{env}) \end{cases} \tag{5.24}$$

With the following ICs and BCs:

$$\begin{cases} I.C.s & \chi(\tau = 0, z) = 0 \\ & \theta(\tau = 0, z) = 0 \\ & \theta_w(\tau = 0, z) = 0 \\ B.C.s & \chi(\tau, z = 0) = 0 \\ & \left.\dfrac{\partial \chi}{\partial z}\right|_{z=1} = 0 \\ & \theta(\tau, z = 0) = 0 \\ & \left.\dfrac{\partial \theta}{\partial z}\right|_{z=1} = 0 \\ & \theta_w(\tau, z = 0) = 0 \end{cases} \tag{5.25}$$

Even in this case, for the computation of results, we used a non-uniform grid (following the Chebyshev polynomial), and 2-point-upwind scheme for the first derivative and 3-point-centered for the second derivative.

Solution with different ICs

Under standard conditions, hence P_{IN}=1.6 kPa, T_{IN}=625 K, v_0=1 $\frac{m}{s}$, $v_{0,cool}$=0,3 $\frac{m}{s}$ $T_{w,IN}$= 625 K, we have the profiles for reactor and jacket temperature in Fig. 5.30:

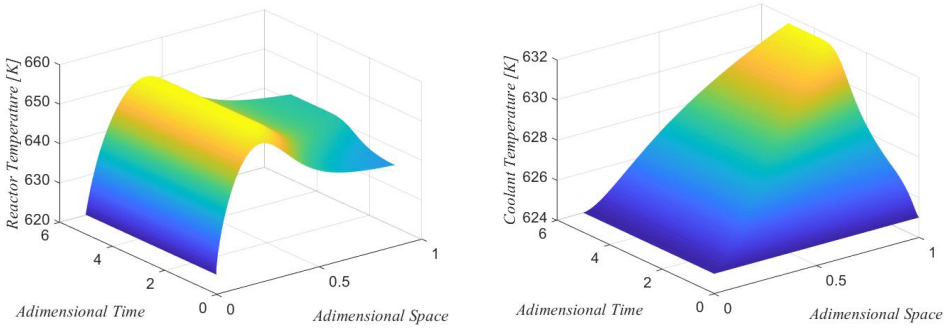

(a) *Reactor temperature* (b) *Jacket temperature*

Figure 5.30: Temperature profiles for the unsteady state model with constant inlet temperature for the jacket (P_{IN}=1.6 kPa, T_{IN}=625 K, v_0=1 $\frac{m}{s}$, $v_{0,cool}$=0,3 $\frac{m}{s}$ $T_{w,IN}$= 625 K)

A lot of comments can be made:

- We notice that, with this reactor properties, the assumption of constant temperature for the jacket is not negligible: we denote a temperature increase of about 8 degrees for the molten salts mixture
- The maximum temperature in the reactor is influenced: 655.92 K vs 651.25 K for the steady state case
- The transient of the reactor takes longer: it requires at least 2 complete runs inside the reactor in order to reach the steady state
- The reactor hotspot is shifted towards right (0.3 vs 0.18 for the steady state)

We then perform the same test ai increased inlet pressure P_{IN}= 1.85 kPa.

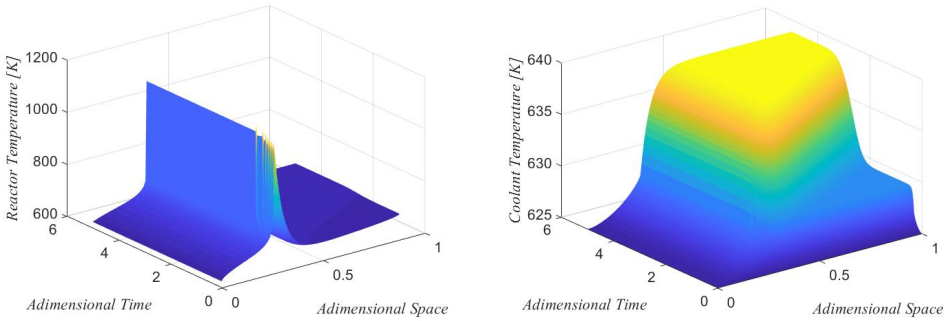

(a) *Reactor temperature* (b) *Jacket temperature*

Figure 5.31: Temperature profiles for the unsteady state model with constant inlet temperature for the jacket (P_{IN}=1.85 kPa, T_{IN}=625 K, v_0=1 $\frac{m}{s}$, $v_{0,cool}$=0,3 $\frac{m}{s}$ $T_{w,IN}$= 625 K)

In this case, the hotspot is in the same position then the previous case, but we see a greater deviation for the reactor maximum temperature: 1141 K vs 905 K for the steady state case.

We also tested different jacket set-ups: we considered higher cooling fluid velocities (1 $\frac{m}{s}$). Figure 5.32 shows the results.

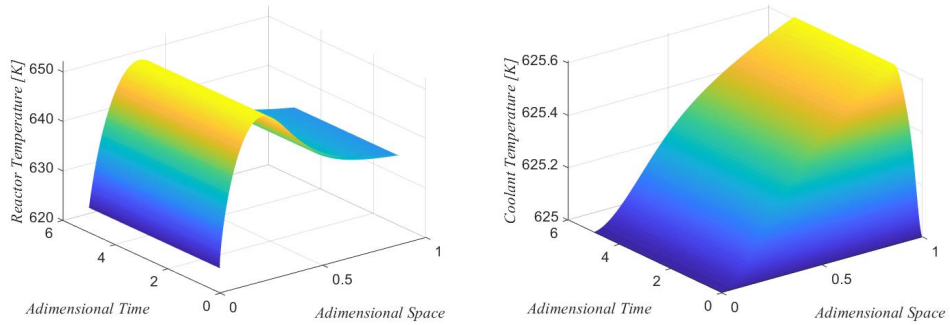

(a) *Reactor temperature* (b) *Jacket temperature*

Figure 5.32: Temperature profiles for the unsteady state model with constant inlet temperature for the jacket (P_{IN}=1.85 kPa, T_{IN}=625 K, v_0=1 $\frac{m}{s}$, $v_{0,cool}$=1 $\frac{m}{s}$ $T_{w,IN}$= 625 K)

In this case, we see that, since the residence time of the cooling fluid is lower, it only increases its temperature of 0.5 K (unimportant for real case

scenarios), and the solution closer to the steady state one (both maximum temperature and hotspot location).

Runaway Boundaries

We performed the sensitivity analysis always with respect to inlet pressure and temperature. We report the results for different fluid velocities. For simplicity, we report only the values of the sensitivity function S. Figure 5.33 show the sensitivity analysis with respect to the inlet pressure. Note that, in this case, the "Steady State" inside the plots (red line) indicates the steady state reached by the unsteady state model after a sufficient time, and it is not then a comparison with the result of the complete steady state model, which results have been already illustrated in Section 5.2.2.

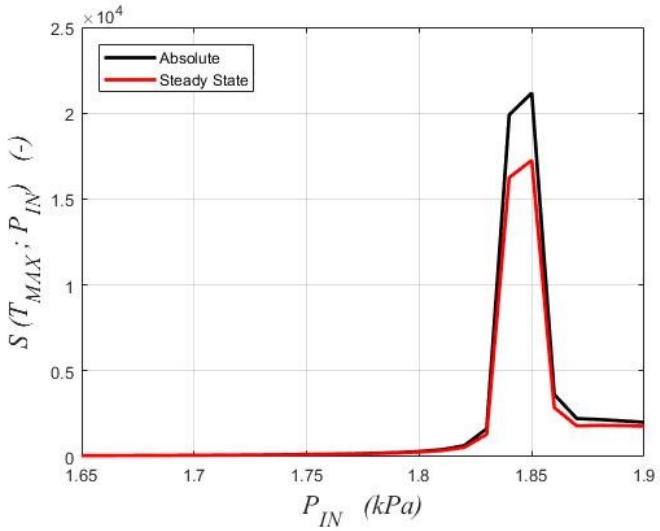

(a) *Sensitivity function S as a function of the inlet pressure (v_0=0.2$\frac{m}{s}$)*

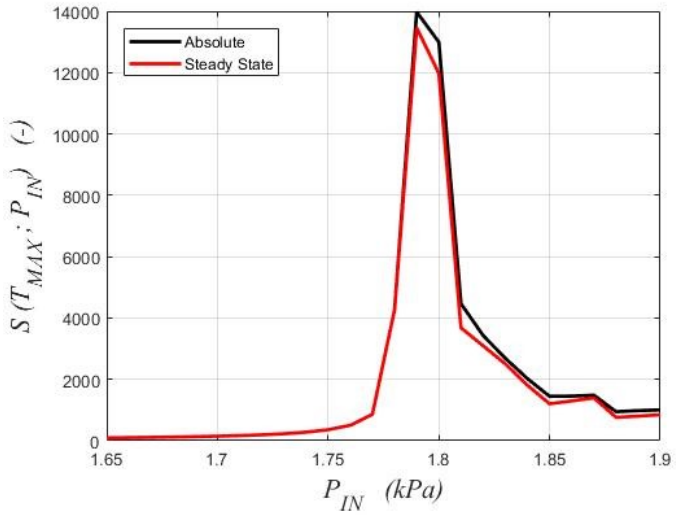

(b) *Sensitivity function S as a function of the inlet pressure (v_0=1$\frac{m}{s}$)*

Figure 5.33: Sensitivity respect to different values of P_{IN}, with T_{IN}= 625 K, v_0=0.2/1 $\frac{m}{s}$, $v_{0,cool}$=0,3 $\frac{m}{s}$ $T_{w,IN}$= 625 K

The system becomes sensitive to lower pressures increasing the inlet velocities of the reactant flow: the critical pressure is shifted from 1.85 kPa (v_0

$= 0.2\ \frac{m}{s}$) to 1.8 kPa ($v_0 = 1\frac{m}{s}$).

Figure 5.34 shows the sensitivity analysis with respect to the inlet temperature.

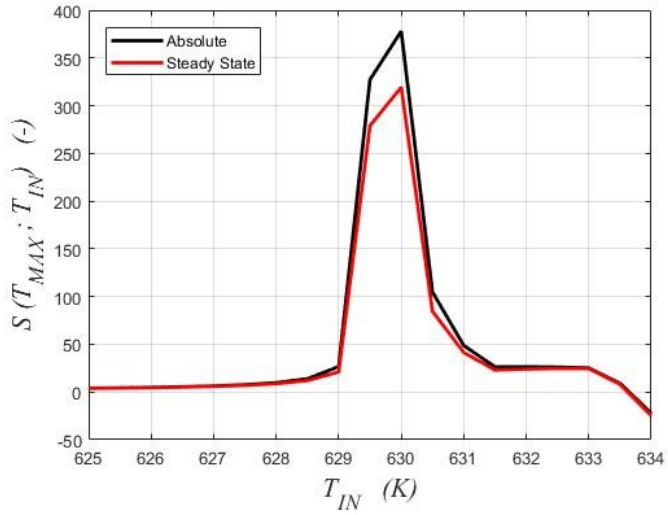

(a) *Sensitivity function S as a function of the inlet temperature (v_0=0.2$\frac{m}{s}$)*

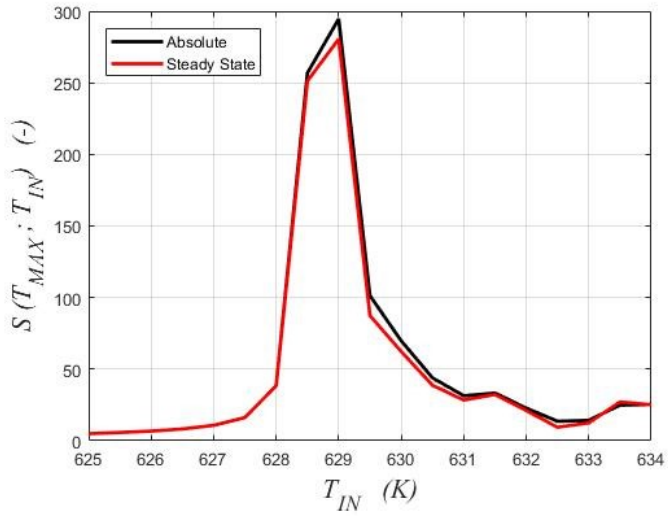

(b) *Sensitivity function S as a function of the inlet pressure (v_0=1$\frac{m}{s}$)*

Figure 5.34: Sensitivity respect to different values of T_{IN}, with P_{IN}= 1.6 kPa, v_0=0.2/1 $\frac{m}{s}$, $v_{0,cool}$=0,3 $\frac{m}{s}$ $T_{w,IN}$= 625 K

The system becomes sensitive to lower temperatures increasing the inlet velocities of the reactant flow: the critical temperature is shifted from 630

K ($v_0 = 0.2\ \frac{m}{s}$) to 629 K ($v_0 = 1\frac{m}{s}$). So, the introduction of a more realistic cooling system, outlines that the maximum temperature achieved are different, and the Runaway Boundaries lead to less conservative results, especially for the inlet temperature.

5.2.5 Unsteady state model, temperature controller

The addition of the temperature controller, modifies the BCs, already presented in Section 5.2. We implemented it inside the MOL with a simple trick: the mass matrix value corresponding to the jacket energy balance is set to 1. In this way, the temporal derivative that is the control equation is taken into account. We will consider a PI controller with a thermocouple installed at the adimensional point z_T. We will always consider a a non-uniform grid (following the Chebyshev polynomial), 2-point-upwind scheme for the first derivative and 3-point-centered for the second derivative.

Runaway Boundaries

We analyzed the Runaway Boundaries for different thermocouple positions and fluid velocities. Figure 5.35 show the diagrams with respect to P_{IN}, with T_{IN}= 625 K, v_0=0.2/1 $\frac{m}{s}$, $v_{0,cool}$=0,3 $\frac{m}{s}$ $T_{w,IN}$= 625 K and thermocouple placed at z_T=0.2.

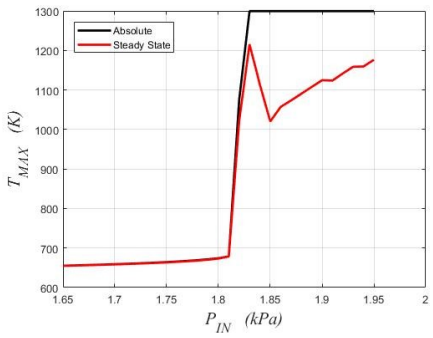

(a) *Maximum temperature as a function of the inlet pressure* (v_0=*0.2*$\frac{m}{s}$)

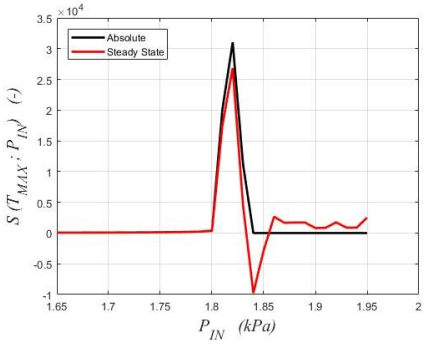

(b) *Sensitivity function S as a function of the inlet pressure* (v_0=*0.2*$\frac{m}{s}$)

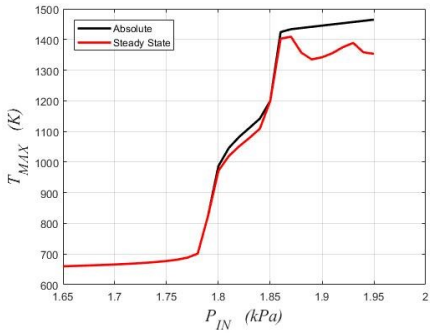

(c) *Maximum temperature as a function of the inlet pressure* (v_0=*1*$\frac{m}{s}$)

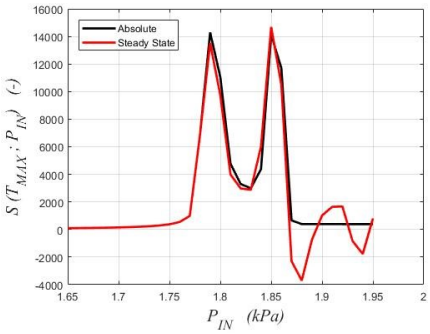

(d) *Sensitivity function S as a function of the inlet pressure* (v_0=*1*$\frac{m}{s}$)

Figure 5.35: Sensitivity respect to different values of P_{IN}, with T_{IN}= 625 K, v_0=0.2/1 $\frac{m}{s}$, $v_{0,cool}$=0,3 $\frac{m}{s}$ $T_{w,IN}$= 625 K and thermocouple placed at z_T=0.2

We notice the system becoming sensitive to lower pressures increasing the inlet velocities of the reactant flow: the critical pressure is shifted from 1.82 kPa to 1.79 kPa. Figure 5.36 shows the diagrams with respect to the inlet temperature.

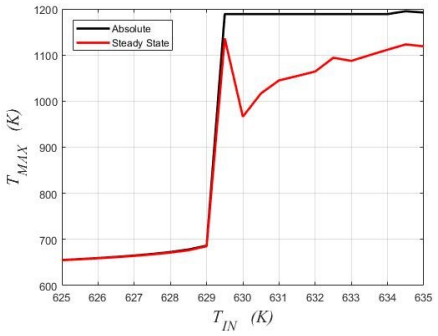

(a) *Maximum temperature as a function of the inlet temperature* (v_0=*0.2*$\frac{m}{s}$)

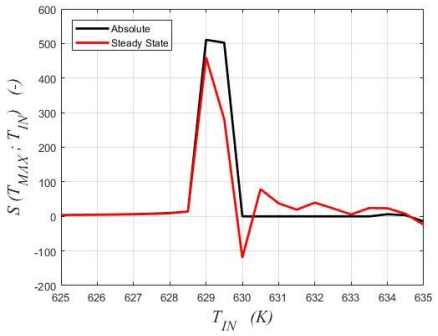

(b) *Sensitivity function S as a function of the inlet temperature* (v_0=*0.2*$\frac{m}{s}$)

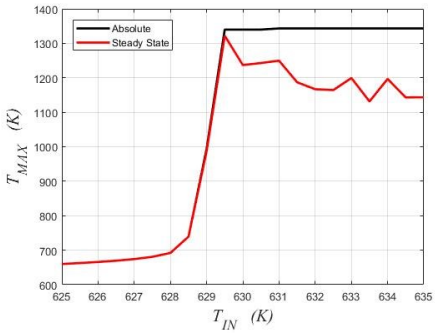

(c) *Maximum temperature as a function of the inlet temperature* (v_0=*1*$\frac{m}{s}$)

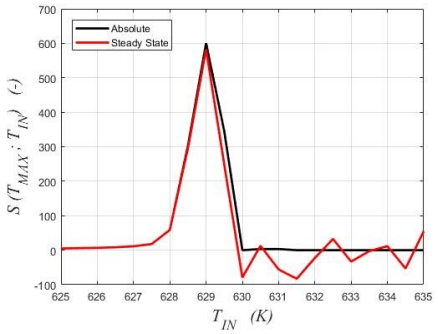

(d) *Sensitivity function S as a function of the inlet temperature* (v_0=*1*$\frac{m}{s}$)

Figure 5.36: Sensitivity respect to different values of T_{IN}, with P_{IN}= 1.6 kPa, v_0=0.2/1 $\frac{m}{s}$, $v_{0,cool}$=0,3 $\frac{m}{s}$ $T_{w,IN}$= 625 K and thermocouple placed at z_T=0.2

The system becomes sensitive to lower temperatures increasing the inlet velocities of the reactant flow: the critical temperature is shifted from 629.5 K to 629 K.

This thermocouple position should be good for the system, since it is able to read information in a place where the exothermicity takes place.

We derived then the diagrams under the same conditions but with the thermocouple placed in at z_T=0.6.

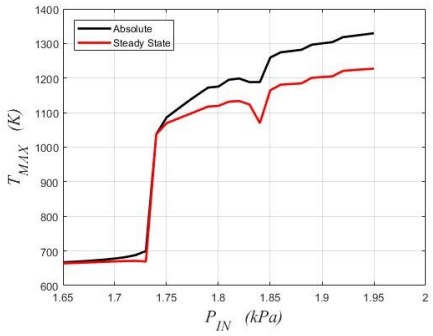

(a) *Maximum temperature as a function of the inlet pressure (T_{IN}=625K)*

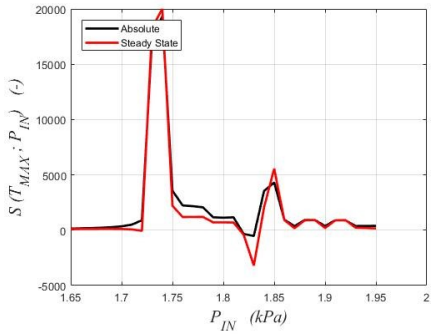

(b) *Sensitivity function S as a function of the inlet pressure (T_{IN}=625K)*

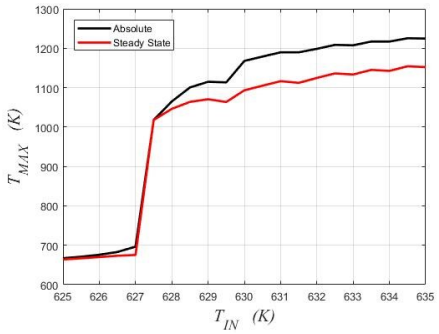

(c) *Maximum temperature as a function of the inlet temperature (P_{IN}=1.6kPa)*

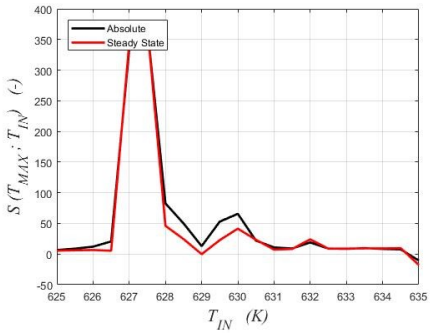

(d) *Sensitivity function S as a function of the inlet temperature (P_{IN}=1.6kPa*

Figure 5.37: Sensitivity respect to different values of P_{IN} and T_{IN}, with v_0=0.2 $\frac{m}{s}$, $v_{0,cool}$=0,3 $\frac{m}{s}$ $T_{w,IN}$= 625 K and thermocouple placed at z_T=0.6

Here we have these critical values: 1.74 kPa for the pressure and 627.5 K for the temperature.

5.2.6 Summary of results

We report here the results obtained for the whole study.

For what concerns the parametric sensitivity, the developed analysis has showed good agreement with the result presented in the literature [37]. Two critical parameters were found, with v_0=1 $\frac{m}{s}$:

- $P_{IN,cr}$=1.85 kPa

- $T_{IN,cr}$=630 K

Those values have been produced under the same conditions of the literature study, where the jacket was considered with a constant temperature. Adding the heat exchanger with a real fluid in a jacket, we noticed an interesting result: the runaway boundaries shift towards lower temperatures if the coolant velocity decreases. If the fluid had enough low residence time in the jacket (that is, high velocity), it would have an almost flat temperature profile, coinciding with the constant temperature case. Under such conditions, the result coincides with the literature one. Decreasing the coolant velocity, its thermal profile changes, due to the heat produced by the reaction. This causes a worse cooling system overall, and the system starts to be sensitive at lower temperatures (from 630 K for v_{cool}=1 $\frac{m}{s}$ to 627.5 K with v_{cool}=0.1 $\frac{m}{s}$). Considering the PI controller, we report the critical values. In the case of one thermocouple, the two critical parameters depend on the position of the thermocouples (z_T is intended as a dimensionless length, and it can assume values from 0 to 1).

If z_T is 0.2 the critical values are:

- $P_{IN,cr}$=1.82 kPa
- $T_{IN,cr}$=629.5 K

If z_T is 0.6 the critical values are:

- $P_{IN,cr}$=1.74 kPa
- $T_{IN,cr}$=627.5 K

From those results, we can notice how a bad control strategy (such as positioning the thermocouple at $z_T = 0.6$, where the reaction has already expressed its exothermicity), leads to a shifting to lower values for the critical values of the boundary diagrams, this means an intrinsically lesser safe system. The hot spot may undergo large variations in the response to relatively small changes in one or more of the operating conditions, thus the PFR reactors without or with PI controller provide desired or undesired behavior to identify runaway conditions.

Conclusions

In this work, we applied the Method of Lines to solve problems in the field of chemical engineering. Our results remark the utility of the MOL, which appears to be still a versatile and powerful tool to simulate chemically reactive systems. The proposed codes have been implemented and solved inside $MATLAB^{\mathrm{TM}}$environment. The application of such method has been widely investigated, considering several types of grids and Finite Differences schemes. The MOL resulted as a stable resolutive method, applicable to a wide set of PDEs.

In the first part of the work, a model to estimate an important parameter for explosive dust has been developed. The model was based upon material and energy balances, written based upon both theoretical data and semi-empirical tools. Most of the required parameters, including lumped kinetic data for the dust pyrolysis can be deduced by performing a TGA analysis on a dust sample, that is a pretty cheap test. This model was validated by comparison with experimental values measured in a 20 L sphere test for eight common types of organic dust. The substances considered were: Aspirin, Cork, Corn starch, Niacin, Polyethylene, Polystyrene, Sugar and Wheat flour. The results can be considered very promising; in fact, the developed model allows for predicting the k_{ST} value for different dusts with different particle sizes: this imply a substantial reduction of time and costs related to the analysis, making the evaluation of the risks linked to combustible dusts much more affordable. However, there is still room for improvements, since some criticalities also remain. For example, pressure vs time curves given from simulations and theoretically representative of a 20 L test are not always in perfect agreement with the data collected during a real experimental test. It will be target of future works to provide models with good predictions of all the quantities involved in the process. Also, it is important to remember that, despite the evaluation of the deflagration index is subject of strict in-

ternational regulations (ASTM and EN standards), the parameter itself can be considered sometimes misleading in the assessment of the hazardous property of an explosive dust. Hence, it could be interesting using the approaches presented in this work to estimate other parameters, such as the Minimum Ignition Energy and the Minimum Ignition Temperature.

In the second part of the work, a PFR reactor for the naphthalene oxidation has been successfully simulated in this work. The reactor is equipped with a thermal jacket, where a Heat Transfer Salt is used as thermoregulating fluid. The reactor can also be thermally controlled by a PI controller, a pretty common strategy in process industry. In order to study the safety of this process, parametric sensitivity calculations have been carried out, studying the sensitivity of the reactor temperature with respect to the inlet pressure and inlet temperature at different residence times and different coolant heating capacities. The results of the simulations show interesting observations for what concerns both the optimization of the process and its safety issues.

For what concerns the maximum temperature achieved under unsteady state conditions, we noticed that it coincides with the value of the stationary one, so the dynamic integration gives the same outcome. The unsteady state model also approaches the start-up of the reaction, which is a very important part of the whole process. By adding more information to the model, we notice how the discrepancy between unsteady states and steady states slightly increases. Involving the reactor jacket, we notice a slight difference between steady and unsteady state. This is due to the jacket reactor profile, which evolves with characteristic times higher than the reactor ones. With the addition of thermocouples and the implementation of a thermal control, we do not notice sensible differences among the maximum temperatures in the cases involved, under standard operating conditions.

For the parametric sensitivity analysis, we found good agreement with the results provided in the current literature, by using the same assumptions of these works (constant temperature jacket).

Adding the heat exchanger with a real fluid in a jacket, we noticed an interesting result: the runaway boundaries shift towards lower temperatures if the coolant velocity decreases. If the fluid had enough low residence time in the jacket (that is, high velocity), it would have an almost flat temperature profile, coinciding with the constant temperature case. Under such conditions, the result coincides with the literature one. Decreasing the coolant velocity, its thermal profile changes, due to the heat produced by the reaction. This causes a worse cooling system overall, and the system starts to be

sensitive at lower temperatures (from 630 K for v_{cool} =1 $\frac{m}{s}$ to 627.5 K with v_{cool}=0.1$\frac{m}{s}$).

Considering the PI controller, we noticed criticalities related to the positioning of the thermocouple. A badly placed thermocouple can induce runaway in the system, despite being implemented with the aim of stabilizing the process.

Finally, this work sets a base for many future works, with the final target of having a better understanding of such phenomena, developing more efficient strategies aimed to predict the behavior of a real process, avoiding runaway accidents. Further investigation should be carried out on unsteady state models with multiple dimensions, in order to study the effect of radial diffusion, that afflicts both material and heat transfer. The study of the eventual shifting of the relative runaway boundary is definitely an interesting aspect.

Bibliography

Dust Explosions state of art

[1] Abbasi, T., Abbasi, S.A.,*Dust explosions-Cases, causes, consequences, and control.* J. Hazard. Mater. 140, 7e44, 2007

[2] Allen, T.,*Particle Size Measurement, 3rd ed.* London: Chapman and Hall, 1981

[3] Amyotte, P., *An Introduction to Dust Explosions e Understanding the Myths and Realities of Dust Explosions for a Safer Workplace.* Butterworth-Heinemann,Oxford, 2003

[4] Bartknecht, W., *Brenngas-und Staubexplosionen. Forschungsbericht F45.* Federal Republic of Germany: Bundesinstitut fur Arbeitsschutz, Koblenz, 1971

[5] Bartknecht, W., 1978, *Explosionen, Ablauf und Schutzmassnahmen.* Springer-Verlag, Berlin, Heidelberg, New York, 1978

[6] Bartknecht, W., *Dust Explosions: Course, Prevention, Protection.* Springer-Verlag, Berlin, 1989

[7] Birks, N., Alabi, F.,*Reactions leading to the auto-ignition of direct reduced iron.* In: Proc. 5th Int. ISI Congress, Washington, D C, p. 83, 1986

[8] Dorsett, H. G., M. Jacobson, J. Nagy, et al.*Laboratory Equipment and Test Procedures for Evaluating Explosibility of Dusts.* Report Inv. 5424. Washington, DC: U.S. Bureau of Mines, 1960

[9] Field, P.,*Explosibility Assessment of Industrial Powders and Dusts.* London: Department of the Environment, Building Research Establishment, Her Majesty?s Stationery Office, 1983

[10] Eckhoff, R.K.,*Dust Explosions in the Process Industries.* Gulf Professional Publishing,2003

[11] Eckhoff R., Li G., Yang H-X., Yuan C-M., A catastrophic aluminium-alloy dust explosion in China, Journal of Loss Prevention in the Process Industries, 2015

[12] Fumagalli, A., Derudi, M., Rota, R., Copelli, S. *Estimation of the deflagration index KSt for dust explosions: A review. Journal of Loss Prevention in the Process Industries.* 44, 311-322, 2016

[13] Hertzberg, M., K. L. Cashdollar, and J. J. Opferman, *The Flammability of Coal Dust-Air Mixtures. Lean Limits, Flame Temperatures, Ignition Energies and Particle Size Effects* Report Inv. 8360. Washington,DC: U.S. Bureau of Mines, 1979

[14] Hertzberg, M., R. S. Conti, and K. L. Cashdollar, *Electrical Ignition Energies and Thermal Autoignition Temperatures for Evaluating Explosion Hazards of Dusts.* Report Inv. 8988 Washington, DC: U.S. Bureau of Mines, 1985

[15] International Standards Organization, *Explosion Protection Systems. Part 1. Determination of Explosion Indices of Combustible Dusts in Air.* ISO 6184/1, 1985a

[16] Kauffman, C. W., and R. F. Hubbard.,*Investigation of Fourteen Grain Elevator Explosions Occurring between January 1979 and April 1981.* Washington, DC: Occupational Safety and Health Administration, 1984

[17] Lightstone,M. F., and G. D. Raithby,*A Stochastic Model of Particle Dispersion in a Turbulent Gaseous Environment.* Combustion and Flame 113,pp. 424-441, 1998

[18] Lunn, G. A. *Aluminium Powder Explosion at ALPOCO, Anglesey, UK.* Report No. SMR 346/235/0171. Health and Safety Executive, Explosion and Flame Laboratory, 1984

[19] Morozzo, Count.,*Account of a Violent Explosion which Happened in a Flour-Warehouse, at Turin, December the 14th, 1785, to which are Added some Observations on Spontaneous Inflammations.* Repertory of Arts and Manufactures 2, pp. 416-432, 1795

[20] Skjold T., Arntzen B. J., Hansen O. R., Taraldset O. J., Storvik I. E., Eckhoff R. K., *Simulating Dust Explosions with the First Version of DESC.* Process Safety and Environmental Protection, Volume 83, Issue 2, pp. 151-160, 2005

Plug Flow Reactors Runaway Boundaries state of art

[21] Adler, J.; Enig, J. W., *The critical conditions in thermal explosion theory with reactant consumption*, Combustion and Flame, 8, 97, 1964

[22] Balakotaiah, V.; Luss, D.,*Structure of the Steady-State Solutions of Lumped-Parameter Chemically Reacting Systems*, Chemical Engineering Science, 37, 1611, 1982

[23] Barkelew, C. H., *Stability of Chemical Reactors. Chemical Engineering Progress Symposium Series*, 25, 37, 1959

[24] Bilous, O.; Amundson, N. R.,*Chemical Reactor Stability and Sensitivity II. Effect of Parameters on Sensitivity of Empty Tubular Reactors*, AIChE Journal, 2, 117, 1956

[25] Chemburkar, R. M.; Morbidelli, M.; Varma, A.,*Parametric sensitivity of a CSTR*, Chemical Engineering Science, 41, 1647, 1986

[26] Degnan, T. R.; Wei, J.,*The co-current reactor heat exchanger: part I. Theory*, AIChE Journal, 25, 338. 1979

[27] Dente, M.; Collina, A., *II comportamento dei reattori chimici a flusso longitudinale nei riguardi della sensitività* . La Chimica e L'Industria,46, 752, 1964

[28] Dente, M.; Buzzi Ferraris, G.; Collina, A.; Cappelli, A.,*Sensitivity behavior of tubular chemical reactors, II. Sensitivity criteria in the case of parallel reactions*, Quaderni di Ingegneria Chimica Italiana, 48, 47, 1966

[29] Henning, G. P.; Perez, G. A., *Parametric sensitivity in fixed-bed catalytic reactors.* Chemical Engineering Science, 41, 83, 1986

[30] Luss, D.; Medellin, P., *Steady state multiplicity and stability in a counter currently cooled tubular reactor.* Proceedings of the Fifth European/Second International Symposium on Chemical Reaction Engineering, B4, 47.1972

[31] Morbidelli, M.; Varma, A. *Parametric Sensitivity and Runaway in Tubular Reactors.* AIChE Journal, 28, 705, 1982

[32] Morbidelli, M.; Varma, A., *A generalized criterion for parametric sensitivity: application to thermal explosion theory.* Notes - Unpublished Document,1985

[33] Soria Lopez, A.; De Lasa, H. I.; Porras, J. A. *Parametric sensitivity of a fixed bed catalytic reactor.* Chemical Engineering Science, 36, 285.1981

[34] Strozzi, F.; Zaldivar, J. M.; Kronberg, A. E.; Westerterp, K. R., *On-line runaway detection in batch reactors using chaos theory techniques.* AIChE Journal, 45, 2429, 1999

[35] Thomas, P. H., *Effect of reactant consumption on the induction period and critical conditions for a thermal explosion.* Proceedings of the Royal Society A, 262, 192, 1961

[36] van Welsenaere, R. J.; Froment, G. F., *Parametric sensitivity and runaway in fixed bed catalytic reactors.* Chemical Engineering Science, 25, 1503, 1970

[37] Varma, A.; Morbidelli, M.; Wu, H., *Parametric Sensitivity in Chemical Systems.* Cambridge University Press: 1999

[38] Wu, H.; Morbidelli, M.; Varma, A. *An approximate criterion for reactor thermal runaway.* Chemical Engineering Science, 53, 3341, 1998

[39] Zaldivar, J. M.; Cano, J.; Alos, M. A.; Sempere, J.; Nomen, R.; Lister, D.; Maschio, G.; Obertopp, T.; Gilles, E. D.; Bosch, J.; Strozzi, F., *A general criterion to define runaway limits in chemical reactors.* Journal of Loss Prevention in the Process Industries, 16, 187,2003

Method of Lines

[40] Cynar, S., J., *Using Gaussian elimination for computation of difference equation coefficients.*, SIGNUM Newsl. (USA), v. 22, pp. 12-19, 1987

[41] Fornberg, B.,*Generation of finite difference formulas on arbitrarily spaced grids.* Math. Comput. 51(184):699-706 , 1988

[42] Fornberg, B.,*Calculation of weights in finite difference formulas.* SIAM Rev40 (3):685-691, 1998

[43] Hirsch C., *Numerical Computation of Internal and External Flows.* Second edition, Vol.1, Butterworth-Heinemann, 2007

[44] Kazem S., Dehghan M., *Application of finite difference method of lines on the heat equation.* Numer. Methods Partial Differential Eq.; Vol. 34, pp. 626-660, 2018

[45] Keller, H., B., Pereyra, V., *Symbolic generation of finite difference formulas.* Math. Comp., v. 32, pp. 995-971, 1978

[46] Lakin, W., D., *Differentiation matrices for arbitrarily spaced grid points.* Internat. J.Numer. Methods Engrg., v. 23, pp. 209-218, 1986

[47] Lax, P. D.; Richtmyer, R. D. *Survey of the Stability of Linear Finite Difference Equations* Comm. Pure Appl. Math. 9: 267?293, 1956

[48] Mohamed, F., Pantea, C., Tudorascu,*Chemical reaction-diffusion networks: convergence of the method of lines* A. J Math Chem, Vol. 56, pp. 30-68, 2018

[49] Naguib M.,*On the validity and stability of the method of lines for the solution of partial differential equations.* Applied Mathematics and Computation, Vol. 22, 2?3, pp. 89-98, 1987

[50] Reddy, S.C., Trefethen, *Stability of the method of lines.* L.N. Numer. Math. 62: 235, 1992

[51] Salehi, Y., Darvishi, M., T., Schiesser, W., E., *Numerical solution of space fractional diffusion equation by the method of lines and splines.* Applied Mathematics and Computation,Vol. 336, Pp. 465-480, 2018

[52] Schiesser W.E., *The numerical method of lines: Integration of Partial Differential Equations*, Academic Press, San Diego, 1991

[53] Schiesser, W. E., Griffiths, G. W. ,*A Compendium of Partial Differential Equation Models: Method of Lines Analysis with Matlab* , Cambridge University Press, 2009

[54] Vande Wouwer, A., Saucez P., Schiesser, W. E.,*Simulation of distributed parameter systems using a Matlab-based method of lines toolbox: Chemical engineering applications*, Industrial and Engineering Chemistry Research, 43, 3469-3477, 2004

[55] Vande Wouwer, A.; Saucez, P.; Vilas, C.,*Simulation of ODE/PDE Models with MATLAB,OCTAVE and SCILAB. Scientific and Engineering Applications.* Springer International Publishing Switzerland, 2014

[56] Verwer, J., G., Sanz-Serna, J., M., *Convergence of method of lines approximations to partial differential equations.* J.M. Computing, 33: 297, 1984

Dust explosions in a 20 L sphere model

[57] Copelli, S., Barozzi, M., Scotton, M., S., Fumagalli, A., Derudi, M., Rota, R:, *Development of a predictive model for the estimation of the deflagration index of organic dusts*, submitted article

[58] Andrews, J.G., Atthey D.R.,*On the motion of an intensely heated evaporating boundary.* IMA Journal of Applied Mathematical, Volume 15, Issue 1, 59-72, 1975

[59] Çengel, Y., A., *Introduction to Thermodynamics and Heat Transfer, 2nd Edition.* Mc Graw Hill, 2008

[60] Dahoe, A.E., Cant, R.S., Scarlett, B., *On the decay of turbulence in the 20-liter explosion sphere.* Flow Turbul Combust, 67: pp. 159-184, 2001

[61] Di Benedetto, A., Russo, P., Amyotte, P., Marchand, N.,*Modelling the effect of particle size on dust explosions.* Chemical Engineering Science 65 (2), pp. 772-779, 2010

[62] Di Blasi, C., *Linear pyrolysis of cellulosic and plastic waste.* Journal of Analytical and Applied Pyrolysis., PYROLYSIS '96, 40-41, pp. 463-79, 1997

[63] Fumagalli, A., Derudi, M., Rota, R., Snoeys, J., Copelli, S.,*Prediction of the deflagration index for organic dusts as a function of the mean particle diameter.* Journal of Loss Prevention in the Process Industries 50, pp. 67-74, 2017

[64] Staggs, J.E.J., *A simple model of polymer pyrolysis including transport of volatiles.* Fire Safety Journal 34 (1), pp. 69-80, 2000

[65] Zhen, G., Leuckel, W., *Determination of Dust-Dispersion-Induced Turbolence and its influence on dust explosions.* Combustion Science and technology 113 (1), pp. 629-639, 1996

PFR model

[66] Stephanopoulos G., *Chemical Process Control. An Introduction to Theory and Practice.* Prentice-Hall, Englewood Cliff, 1984

[67] Visioli A., *Research Trends for PID Controllers.* Acta Polytechnica Vol. 52 No. 5/2012, 2012

[68] Bohlmann E.G., *Heat transfer salt for high temperature steam generation.* Reactor Chemistry Division, OWL-TM-3777, 1972

[69] Gaune-Escard M., Haarberg G. M.,*Molten Salts Chemistry and Technology.* John Wiley and Sons Ltd., UK, 2014

[70] Kirst W.E., Nagle M. W., Castner J. B., *New Heat Transfer Medium for High Temperatures* A, Trans. Am. Inst. Chem. Engrs, 36, 371, 1940